DESIGN, ANALYSIS, AND OPTIMIZATION OF WRIST-WORN ENERGY HARVESTERS

by

Robert Rantz

A dissertation submitted to the faculty of
The University of Utah
in partial fulfillment of the requirements for the degree of

Doctor of Philosophy

Department of Mechanical Engineering

The University of Utah

May 2019

The University of Utah Graduate School

STATEMENT OF DISSERTATION APPROVAL

The dissertation of **Robert Rantz**

has been approved by the following supervisory committee members:

Shadrach Roundy	, Chair	**2/20/2018** Date Approved
Jake Abbott	, Member	**2/20/2018** Date Approved
Jiyoung Chang	, Member	**2/20/2018** Date Approved
Kam Leang	, Member	**2/20/2018** Date Approved
Andrejs Treibergs	, Member	**2/20/2018** Date Approved

and by **Bruce Gale** , Chair/Dean of

the Department/College/School of **Mechanical Engineering**

and by David B. Kieda, Dean of The Graduate School.

ABSTRACT

An interest in wearable sensors for activity tracking and health monitoring, coupled with the desire for energy-independent devices for increased convenience and an improved user experience, have resulted in significant research and commercial interest in wrist-worn energy harvesting. Energy harvesting – an alternative to finite, traditional energy storage technologies, such as batteries – has the potential to provide power to wearable devices for a functionally unlimited amount of time by extracting ambient, freely-available energy from the environment, obviating the need for user intervention in replenishing a finite energy supply. Vibration energy harvesting, which concerns the harvest of kinetic energy, is of particular interest for wearable applications. However, the low-frequency, high-amplitude excitations that typify wrist motion during common daily activities make vibration energy harvesting using traditional linear vibration energy harvesting architectures challenging. Alternatives to linear vibration energy harvesting architectures have been proposed for wrist-worn energy harvesting, with eccentric rotor harvesters – asymmetric, rotational devices – representing a common choice in the literature (possibly due to the watch-like form factor and extant commercial products) that exhibit some interesting properties.

This project concerns the design, analysis, and optimization of architectures for wrist-worn energy harvesting, with particular emphasis placed on eccentric rotor harvesting architectures. The problem of determining which architecture is best suited for wrist-worn energy harvesting is first approached by deriving mathematical models of several common architectures and developing a means by which the disparate architectures may be compared fairly. Eccentric rotor harvesters – especially those that include a torsional spring – fare particularly well, and become the focus of the remainder of the work. Several generations of eccentric rotor prototypes are designed, fabricated, and characterized in order to validate the mathematical models and demonstrate the improvement of power output that comes with the addition of a torsional spring to the eccentric rotor architecture. Finally, a dynamical analysis gives insight into how the design parameters affect power output and provides an explanation for some of the nonlinear behavior observed in these devices. This knowledge is used to develop a new kind of eccentric rotor harvester that may have significant advantages over designs hitherto presented in the energy harvesting literature.

TABLE OF CONTENTS

LIST OF TABLES

Tables

CHAPTER 1

INTRODUCTION

1.1 Motivation

The desire for vast networks of embedded, wirelessly connected sensors in applications ranging from remote health monitoring to infrastructure management, coupled with a decrease in the power demands of sensing and communications technology, have driven an interest in the development of novel mechanisms for delivering power to low-power electronics. Traditional energy storage technologies, such as batteries, degrade with time and require regular replacement that is often either highly undesirable, entirely infeasible, or impossible to perform. Additionally, finite energy storage mechanisms such as batteries and capacitors suffer from low energy densities when long device lifetimes are considered [1], [2]. The emergence of low-power integrated circuits and wireless communication technologies has made possible systems capable of powering themselves using ambient energy sources. Of course, this trend has been ongoing for some time; the solar-powered pocket calculator – the first application of photovoltaics in a consumer product context – was introduced in 1978, with other low-power products of daily use following suit thereafter [3]. Powering electronics using ambient energy reaches even farther back in history, however, with *crystal radio receivers* – radios that powered high-impedance earphones using only the strong, relatively local radio frequency signals themselves – claiming roots in technology developed in the late nineteenth century [4, pp. 5-10]. Devices that are free from the constraints of traditional energy storage elements, or devices that augment the performance of such storage elements, have thus been of interest for at least a century.

Lacking a finite reservoir of energy that is maintained during its lifetime via regular replacement or resupply by means of intervention, an electronic device can only fuel its power consumption by virtue of some alternative external supply of energy. Two particular approaches to eliminating or augmenting a finite energy reservoir for electronic systems have become especially prominent in the research literature: *Wireless Power Transfer* (WPT) and *energy harvesting*.

WPT systems address the situation in which the device to be powered (the receiver) has access to a power transmission technology (the transmitter) that has been purposefully designed to direct power to the device. Electromagnetic WPT systems transfer power on the basis of the propagation of electromagnetic waves, and may be broadly classified as radiative and nonradiative [4]. The phenomena of magnetic resonance and near-field inductive coupling are often exploited, and capacitive coupling is also possible. Many WPT systems have been proposed to power devices ranging from minuscule sensing systems to electric vehicles, and some WPT technologies have been in development for over a century [5], [6]. In situations where the medium for transmission is not particularly conducive to electromagnetic power transmission or where shorter wavelengths are desired (as is often the case with bioimplantable devices), even acoustic waves may be used to wirelessly transmit power [7].

The second approach to address the issues with traditional energy storage technologies differs from the WPT solution in the most general sense by whether a transmitter has been intentionally designed to transmit the power to be consumed or whether power is delivered by collecting freely-available, ambient energy from the environment in which the device operates; the latter case is known as energy harvesting or, alternatively, *energy scavenging*. A loop of copper coil designed to absorb the power delivered by a second, external transmission coil would perhaps best be classified as a receiver in a WPT system, for example, whereas a similar device designed to absorb ambient electromagnetic energy in an environment with elevated levels of electromagnetic radiation (as in the case of a crystal radio receiver) may be more accurately classified as an energy harvester. In situations where energy independence is required and the environment contains a source of useful energy that can be scavenged, energy harvesting may be a viable candidate for the delivery of power to electronic systems.

It is important to note that, its broadest interpretation, energy harvesting would encompass many of the power generation technologies used in the provision of electricity on massive scales, and could be said to have been exploited for millennia; windmills have existed for at least a thousand years, after all, and sails have been propelling ships since antiquity [8, pp. 1-11]. For the purposes of this manuscript, it is therefore prudent to restrict the discussion of energy harvesting to that which concerns the delivery of power to small-scale, low-power electronic systems by scavenging freely-available energy.

The human body, by dint of the metabolic processes that sustain all life, represents a repository of energy with harvesting potential in many forms, such as thermal and kinetic; even solar energy is available when the body is in the presence of both natural and artificial light. Additionally, consumers exhibit a proclivity for donning technology; in a 2018 forecast, the industry analyst firm CCS Insight predicted that the smart wearables market is slated to become worth over US $25 billion by 2019 [9]. Additionally, motivated in part by an effort to ameliorate the rising costs of healthcare, a research interest in wearable biosensors and proactive health monitoring technology has materialized [10] and – in recognition of the drawbacks of battery-powered wearables – has led some researchers to produce health monitoring devices that are free from batteries [11], [12]. The conventional wisdom regarding the inconvenience of battery maintenance in consumer electronics [13], coupled with the availability of energy from the human body, gives rise to a potential market opportunity if a suitable body-worn energy harvesting technology can be developed.

1.2 Energy Harvesting Overview

Various forms of energy may be accumulated from the environment, including energy from solar radiation, thermal gradients, radiative radio frequency electromagnetic waves, wind, and motion [14], [15].

Harvesting solar energy typically involves solar cells, which harvest energy by virtue of the photovoltaic effect – the direct conversion of incident light into electricity [16]. Although solar cells require no moving parts and are highly modular, they require additional signal processing technology, a relatively large surface area, and their functionality is contingent upon the availability of light in the application of interest [14].

Thermal gradients may be used to generate electricity by making use of the Seebeck effect, with a typical semiconductor thermoelectric generator consisting of n- and p-type semiconductor legs connected in series by metal strips and thermally in parallel [17]. Thermoelectric generators are a solid-state technology that is highly reliable and generates little noise and emissions [17], although limitations with materials appear to have limited the conversion efficiency of such generators, and sufficiently large thermal gradients often do not exist in many applications where small device volumes are required [18].

Far-field radio frequency harvesting techniques for powering wireless networks have received considerable attention in the literature, although, due to the inverse-square law dictating that the power density of radio frequency waves decreases proportionally to the inverse of the square of the propagation distance, achieving high power transfer rates is difficult in general; direction and gain of the receive antennas, impedance mismatching issues, and some line-of-sight requirements also negatively impact the efficacy of far-field radio frequency harvesting techniques [19].

Small scale windmills have been proposed and fabricated for use in powering autonomous sensor networks using piezoelectric transducers, which are considered an alternative to the more commonly used electromagnetic transducers that can improve safety and better enable the harvesting of energy at lower wind speeds [20]–[22]. As the purpose of a windmill is to extract kinetic energy from the motion of the surrounding air, such devices can be considered a subset of energy harvesters that derive their energy from ambient motion.

If vibration of sufficient amplitude is present in the application of interest, then it is natural to seek freely available kinetic energy as a means by which one may power electronic devices; this specific class of energy harvesting is known as *vibration* or *kinetic energy harvesting*. Vibration energy harvesting has received much attention in the literature not only because mechanical vibrations are present in a vast number of applications, but also because vibration energy harvesting techniques can provide stable power for longer periods of time when compared to typical energy storage technologies; additionally, vibration energy harvesters can exhibit energy densities greater than both batteries and many other energy harvesting techniques, depending on the application [2]. As many vibration energy harvesters are mechanical resonators, devices have moving parts, are often displacement-limited, and typically exhibit a sharp resonance peak in which a small mismatch in input frequency and the resonator natural frequency can result in a severe reduction in power output.

1.2.1 Energy Harvesting from Human Motion

In a seminal paper on energy harvesting for wearable computing [23], a basic analysis on the caloric intake and expenditure of human beings is performed with the intention of assessing the feasibility of powering computing systems using the energy from the human body. Various sources of energy, including body heat, respiration, blood pressure, air resistance, upper limb motion, and walking are assessed. The study concludes that harvesting the energy from motion – especially from walking – holds the most promise in terms of available power for harvest with the fewest disadvantages to the user. The calculations from the study suggest power on the order of tens of Watts may be available from human motion, although limitations in the recovery of this power, as well as practical considerations concerning an unencumbered user experience, would likely yield a more realistic estimate on the order of a few Watts. The power available from walking – specifically, from the fall of the heel during the heel strike phase of walking – is promising and appears to exceed that which is available from upper body motion. However, devices placed in a shoe capable of harvesting energy from the heel during walking have the disadvantage of inconvenience of location for both user-device interaction as well as acquisition of physiological measurements of interest; it's worth noting that practically all activity tracking devices are placed on or near the upper body during use [24], [25].

A distinction is often made in the energy harvesting literature – especially in wearable energy harvesting – between inertial and direct-force harvesting devices. Inertial harvesting devices rely on the motion of an inertial (or seismic) mass that is excited by virtue of the motion of the housing (or frame) in which the mass is placed. The relative motion that subsequently develops between the housing and the inertial mass is used to produce a force (or torque) on a suitable transducer for the conversion of kinetic energy into electrical energy. Direct-force (or non-inertial) harvesting devices instead use force applied directly between two ends of a transducer to produce power; the aforementioned shoe harvester is thus an example of a direct-force harvesting device. For devices to be worn externally, possibly around a muscle that expands significantly during use, direct-force harvesting devices on the upper body are likely to be very large and obtrusive to the user [26]. The use of solar cells to power wearable devices is also briefly assessed in [26], as well as the use of thermoelectric generators, and the author concludes that energy harvesting from motion is likely the best solution for powering wearable devices, provided that kinetic energy harvesting devices continue to approach theoretical power limits with continued research.

With this elementary discussion of energy harvesting opportunities on the human body in mind, it is reasonable to conclude that inertial, kinetic energy harvesting devices located on the upper body represent a promising pathway for powering wearable electronics. Additionally, due to the prevalence of wristwatches as functional apparel, and the recent proliferation of wrist-worn activity tracking devices, targeting a wrist-worn application is particularly attractive for the development of an upper-body energy harvester to be used in powering smart wearable technology.

1.2.2 Transducer Technologies

An aside on transducer technologies commonly employed in vibration energy harvesters is appropriate before a more detailed discussion on theory begins. Three transducer technologies dominate the energy harvesting literature: electromagnetic, piezoelectric, and electrostatic.

Electromagnetic transducers operate on the basis of Faraday's law of induction; a time-rate-of-change of flux linkage through a conducting coil loop induces a voltage that may be used to drive electric circuits. As the basis for electromotors and large-scale power generation, electromagnetic transducers are ubiquitous. Although there are numerous configurations, practically all electromagnetic transducers are realized using arrays of permanent magnets that generate a static magnetic field that permeates loops of copper conducting wire. Relative motion between the magnets and coils creates a time-varying flux linkage through the coils, which in turn induces a voltage on the coils; if the coils form part of a closed electric circuit, the resultant flow of current dissipates energy, effectively extracting power from the mechanical domain for use in the electrical domain.

Piezoelectric transducers operate on the basis of the piezoelectric effect, in which piezoelectric materials form an electric field in response to an applied mechanical stress. The converse effect is often used in actuators, like those used in the production of ultrasonic acoustic waves. Mechanical strain develops in the piezoelectric material due to the applied stress, and can be induced in a number of ways; patches of piezoelectric material can be applied to mechanical components that exhibit strain during oscillations, for example, or structures comprised of layers of piezoelectric material may constitute the bulk of a mechanical oscillator itself. The charge accumulated on a piezoelectric material under strain is used to drive the flow of current, which may then be used to power electrical circuits.

Finally, electrostatic transducers make use of the property of capacitance in their function. Capacitance is a ratio of the change in charge to a resulting change in electric potential. The capacitance in a system can be varied by changing the gap or overlap between the conductors in a capacitor, or by modifying the properties of the dielectric that separates the conductors. Electrets may also be used in electrostatic transducers, eliminating the need to charge the capacitor that forms the transducer before use. Constant charge and constant voltage approaches to the design of electrostatic transducers are common. Regardless of the approach taken, relative motion of the conductors which form the capacitor causes a change in voltage that is proportional to the relative displacement of the conductors. The changing voltage can then be used to drive an electric circuit, again converting mechanical energy into electrical energy for use in powering electronic devices.

1.2.3 Some Inertial Vibration Energy Harvesting Fundamentals

An inertial vibration energy harvester is comprised, at a minimum, of two primary components: a mechanical structure and a transducer. The former is the portion of the harvester responsible for the absorption of kinetic energy from the environment, and the latter is required to convert kinetic energy into electrical energy. These components are not truly disjoint, however, as the mechanical structure and transducer together form a dynamical system that is designed to be sensitive to incoming excitations to produce relative displacement between the harvester housing and inertial mass that may then drive the production of electricity through the transducer. It is typical for the phenomenon of resonance to be exploited in order to maximize absorbed kinetic energy from the input source. Of particular importance in the development of resonant vibration energy harvester theory is the linear mass-spring-damper as a mathematical harvester model, first proposed in its simplest form in [27], [28], and studied extensively in [29], which serves as both a simplified model for the purpose of theoretical development as well as a reasonable approximation of many real vibration energy harvesters developed in practice (Figure 1-1).

The generic energy harvester model in Figure 1-1 consists of a frame with displacement $y(t)$ and a harvester inertial mass m with absolute (measured from an inertial reference frame) displacement $x(t)$, relative (to the harvester frame) displacement $z(t)$, and displacement limit Z_l, attached to the frame through a suspension composed of

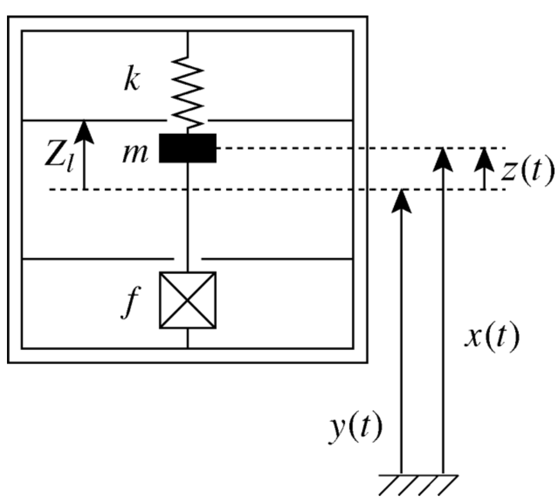

Figure 1-1 – Schematic of a generic, inertial, linear vibration-driven energy harvester. Reproduced, with permission, from [29]. © 2004 IEEE.

a spring element of stiffness k and unspecified damping element with a damping force f. The damping element may or may not contain a model for parasitic losses from, for example, friction. In the seminal work in [29], harmonic excitation of the form $y(t) = Y_0 \cos \omega t$ is considered, with Y_0 representing the displacement amplitude, ω the frequency of excitation, and t time. An attempt to derive the maximum possible power output for a harmonically-driven, linear vibration energy harvester can be found by considering the maximum available acceleration magnitude from the input, $Y_0\omega^2$, assumed to be delivered to the harvester at all times, with a maximum possible damping force that still permits motion, $Y_0\omega^2 m$, acting on the mass, maximum displacement of mass Z_l, and energy extraction in both directions of motion; the result is

$$P_{max} = \frac{2}{\pi} Y_0 Z_l \omega^3 m \tag{1-1}$$

which, on the basis of fundamental considerations, provides an upper bound on the power output of any one-dimensional translational inertial harvester, driven by a continuous excitation, with any transduction mechanism [1]. Of course, (1-1) represents a fundamental limit on power output, and is consequently unrealistically achievable for any real harvester. In order to develop better bounds on performance, some additional harvester structure should be considered.

Noted in [29], as in earlier works [30]–[32], power output generally appears to be proportional to $Y_0^2\omega^3 m$, which makes for a useful normalization term. Normalized power is used throughout [29]. An expression for normalized or dimensionless power output is derived in Chapter 4, yielding a similar normalization term.

In [29], three harvester topologies are delineated and analyzed: the Velocity-

Damped Resonant Generator (VDRG), the Coulomb-Damped Resonant Generator (CDRG), and the Coulomb-Force Parametric Generator (CFPG). All three can be implemented in real devices, using electromagnetics (VDRG) or electrostatics (CDRG and CFPG). As the VDRG model provides a suitable model for the prototypes constructed and analyzed in this project, the behavior of this type of model is of particular interest.

For a VDRG harvester, the transducer damping force f is linearly proportional to the relative velocity $\dot{z}$; that is, the transducer is modeled as a linear viscous damping element. If it is assumed that parasitic losses are negligible, then the maximum power output for a displacement-constrained VDRG harvester at resonance is

$$P_{VDRG} = \frac{1}{2} Y_0^2 \omega^3 m \frac{Z_l}{Y_0} \tag{1-2}$$

where it is assumed that the damping is selected such that the mass is fully displaced up to the displacement limit, Z_l. Note the similarity of (1-2) to (1-1); thus the VDRG model inherits all of the limitations of (1-1), but with a lower fundamental limit on power output. Given the strong dependence of power output on input frequency seen in (1-2), it is immediately clear why the low-frequency excitation typical of human motion imposes serious limitations on power output that may not be seen with high-frequency machine vibration input. Furthermore, vibrations from human motion are not consistent, as they might be for machine motion, and achieving a state of resonance is often difficult in practice. Also, due to the low-frequency and high-amplitude vibrations that typify human motion [33], displacements required for a linear resonant device are very large, which often makes implementations of VDRG harvesters on the human body impractical [1].

A number of harvester architectures have been proposed for harvesting energy from human motion on the upper body that attempt to address some of the unique issues present in such an application. Perhaps most important for this project is the *eccentric rotor* architecture. This architecture is comprised of an asymmetric rotating inertial mass that, as a result of the fact that the rotating center and the center of gravity are not coincident, is excited by both rotational and linear acceleration inputs. Eccentric rotors purposed as inertial masses to harvest kinetic energy from the upper body have a surprisingly long history, as such rotors are found in self-winding watches that were invented perhaps by Abraham-Louis Perrelet, or possibly Hubert Sarton – the history is quite contentious – as early as 1770 [34]. In addition to sensitivity to many kinds of vibratory input, eccentric rotor harvester structures have the additional advantages of a watch-like form factor and no intrinsic displacement limits. What now follows are examples of this architecture in commercial products and in prototype devices in the literature, as well as examples of several other kinds of architectures that have been demonstrated in wrist-worn energy harvesting applications.

1.3 Literature Review

Table 1-1 provides a list of selected publications with associated claims on power generation. Although eccentric rotor-based mechanical architectures for absorbing kinetic energy from human motion are common in the literature (possibly due to the watch-like form factor and extant commercial products), many other mechanical architectures have also been proposed [35]–[50]. Some structures include: 1 Degree of Freedom (DOF) translational inertial masses, 6 DOF inertial masses free to move in an enclosed volume, nonholonomic systems, and mechanical systems that intentionally incorporate

Table 1-1 – Published body-worn energy harvester prototypes

Year	**Author(s) / Reference**	**Mechanical Architecture**	**Dimensions [mm]**	**Transducer**	**Power Output Claim**
1984	Kinetron bv, [50]	1 DOF Eccentric Inertia (Rotation)	⌀ 34×9	Electromagnetic	600 mJ per day
1991	Seiko Watch Corp., [37]	1 DOF Eccentric Inertia (Rotation)	⌀ 36×9	Electromagnetic	250 swings provide 1 day of operation
2009	Renaud *et al.*, [42]	1 DOF Proof Mass (Translation)	35×20×20	Piezoelectric	47 μW under 2 Hz device rotation
2011	Romero *et al.*, [36]	1 DOF Eccentric Inertia (Rotation)	2cm^3 Volume	Electromagnetic	<10 μW for 4 mph walking (worn at elbow)
2014	Rao *et al.*, [51]	6 DOF Proof Mass (Rotation & Translation)	⌀ 37×35	Electromagnetic	100 μW from jogging
2014	Pillatsch *et al.*, [48]	1 DOF Eccentric Inertia (Rotation)	⌀ 30×7	Piezoelectric	0.5 μW to 7 μW during a half marathon (worn on upper arm)
2014	Halim *et al.*, [41]	1 DOF Proof Mass (Translation)	⌀ 13.5×50	Electromagnetic	110 μW when shaken by hand (15 $m{\cdot}s^{-2}$ to 20 $m{\cdot}s^{-2}$)
2015	Ju and Ji, [52]	1 DOF Proof Mass (Translation)	27×26.5×6.5	Piezoelectric	908.7 μW under linear excitation (3 g, 17 Hz)
2015	Nakano *et al.*, [35]	1 DOF Eccentric Inertia (Rotation)	⌀ 40×<10	Electrostatic	3.6 μW during constant rotation of 1 rotation per second
2016	Haroun *et al.*, [53]	4 DOF Proof Mass (Rotation & Translation)	⌀ 9×12	Electromagnetic	87.4 μW during walking (single subject, 75 $m{\cdot}min^{-1}$)
2016	Niroomand and Foroughi [54]	1 DOF Proof Mass (Rotation)	⌀ 50x12.7	Electromagnetic	416.6 μW during walking (best subject, ankle)
2017	Geisler *et al.*, [55]	4 DOF Proof Mass (Rotation & Translation)	⌀ 63×13	Electromagnetic	3 mW under 4 $km{\cdot}h^{-1}$ walking speed
2017	Wang *et al.*,	1 DOF Proof Mass (Translation)	⌀ 150x20	Electromagnetic	10.66 mW under 8 $km{\cdot}h^{-1}$ walking speed (on ankle)
2018	Zhao *et al.*, [56]	1 DOF Proof Mass (Translation)	⌀ 14x50	Electromagnetic	63.9 mW when shaken by hand at 5 Hz, 6 g

nonlinearities. From a reading of the available literature alone, it remains unclear which mechanical architecture is best suited to extract energy at the wrist under excitation from the human wrist during various activities.

A few observations about the publications presented in Table 1-1 will shed some light on the basis for the significance and merit of the research presented in this manuscript:

First, it is not at all clear which mechanical architecture is best for a particular intended application – especially harvesting energy from the wrist from human walking motion. Device volumes are not held constant, transducers differ from device to device, optimization of device parameters is often ignored or not discussed, and there is no standard suite of excitations for experimental testing, rendering comparisons between power output claims useless in terms of determining a mechanical structure best suited for absorbing kinetic energy in a wrist-worn application. A fair comparison between mechanical architectures that sheds light on the optimal architecture is needed; this is the basis for the work presented in Chapter 2.

Secondly, there are numerous, disparate excitations used to test the devices in Table 1-1. Although this reflects a narrow problem of a lack of experimental standardization, it is also reflective of a generic problem in the field of vibration energy harvesting: a lack of rigorous characterization of devices, and a tenuous connection between the benchtop test signal and the device performance for the intended application – harvesting energy from human motion. To more firmly establish the superiority of a particular mechanical architecture proposed in Chapter 2, a benchtop signal reminiscent of arm swing during locomotion is employed consistently between devices as a single parameter is varied, as well as between device generations, for device characterization in Chapter 3. Although not obvious from a cursory reading of Table 1-1, when devices in the literature are tested on human subjects, they are typically tested on one or very few subjects, and sometimes under uncontrolled testing conditions. To establish a baseline of performance, a larger population of human subjects should be used, and the experiments should be carried out under controlled test conditions; this approach is also employed over two device generations in Chapter 3.

Finally, although again not obvious from a reading of Table 1-1, many of the prototyping efforts presented in Table 1-1 are accompanied by a lack of rigorous mathematical modeling and analysis. If a device appears to work well, there may only be speculation as to why this may be the case – if that – and it is not clear if the results are generalizable to other device scales or input excitations. Many papers consist of the fabrication and characterization of a device without any mathematical modeling at all.

Due to the watch-like form factor, the adoption of wrist-worn wearables, and the output of the work presented in Chapter 2, it is clear that there exists great potential for rotational architectures in wrist-worn energy harvesting applications. Such architectures are, however, very complex dynamical systems that exhibit a wealth of interesting dynamical phenomena. For this reason, the relationship between design parameters and power output is not well understood. Even the more elementary relationships between, for example, the seismic mass, or inertia about the center of gravity of the rotor, and the resultant device behavior remain unclear. An analysis of some of the more interesting dynamics of the eccentric rotor system can provide a better understanding of the harvester system and yield pathways to improving performance; this is the basis for the work of Chapter 4.

1.4 Research Objectives

This project focuses on wrist-worn vibration energy harvesting, which is concerned with extracting kinetic energy from the wrist of a user during typical activities, such as locomotion, for the purpose of powering body-worn, low-power electronic devices. The project may be broadly demarcated into three objectives:

Objective 1: Compare architectures for wrist-worn energy harvesting. The goal is to find a harvester architecture that maximizes absorbed kinetic energy at the wrist during locomotion. Several device architectures are proposed, mathematical models representing those architectures are derived, and a methodology for comparing disparate architectures is developed to allow for a fair comparison. Prototype devices are then fabricated in order to corroborate the mathematical models, where necessary. This is followed by a discussion of the results and the idiosyncrasies of the architectures – informed by the mathematical models and numerical simulations – which is provided to give an understanding of the relative merits of each architecture.

Objective 2: Rigorously characterize the sprung and unsprung eccentric rotor architectures. The goal is to demonstrate the results predicted by the mathematical models, as well as continually improve the implementation of a sprung rotational architecture through an iterative design process. A consistent benchtop excitation, reminiscent of human arm swing during locomotion, is used throughout device generations to establish trends of improvement in the design. A population of human subjects is employed to demonstrate that the addition of a torsional spring can greatly improve power output under walking excitations, as well as corroborate model predictions under these excitation scenarios.

Objective 3: Explore the dynamics of the eccentric rotor architecture with the purpose of better understanding the relationship between the design parameters and power output, and potentially uncovering regimes of operation that are available for exploitation. A rotational architecture is promising for wrist-worn energy harvesting. However, the relationship between the harvester behavior (and its power output) and key design parameters is not totally clear from a comparative analysis alone. A highly simplified linear model is used to better understand the primary resonance phenomenon exhibited by the device. A nonlinear perturbation analysis explains the existence of additional resonances and the disagreement between the simple linearized model and the nonlinear model. The work results in a proposal for a resonant eccentric rotor harvester – possibly the first of its kind – that exhibits high power output over a large range of input frequencies with a relatively small requirement for electrical damping.

The completion of the aforementioned objectives yields several contributions: a comparative analysis supporting the choice of rotational architecture for wrist-worn energy harvesting applications, the characterization and empirical demonstration of a novel rotational architecture with a torsional spring, and a dynamical analysis that provides greater depth of understanding of the behavior of eccentric rotor devices that leads to the proposal of a resonant rotational energy harvester device.

1.5 Dissertation Overview

This manuscript consists of five chapters, the first of which is this introduction, followed by the three chapters that comprise the majority of the results of the project: the comparative analysis, prototype device implementation and characterization, and dynamical analysis. The fifth chapter concludes this dissertation and includes a summary of original contributions and suggestions for future work, and is followed by an extensive appendix.

Chapter 0 introduces energy harvesting generally, and energy harvesting from human motion specifically. This chapter provides some useful background on energy harvesting theory and motivates the subsequent chapters.

Chapter 2 presents a comparative analysis of various architectures with the goal of establishing a particular architecture that is best suited for harvesting kinetic energy at the wrist during human walking. This chapter presents a limited set of data collected from real prototypes under benchtop excitations and real walking excitations, demonstrating the beneficial effect that a torsional spring has on the power output for eccentric rotor harvesters and corroborating the mathematical models derived therein. This chapter is a reprint of a journal manuscript published in *Smart Materials and Structures.*

Chapter 3 is a history of the prototyping and characterization efforts that help to reify many of the conclusions drawn from the mathematical models developed for this project. The experiments carried out on several generations of prototypes firmly establish that the addition of a torsional spring to eccentric rotor prototypes can greatly improve power output under waking excitations. Details of the design each generation of prototype are provided.

Chapter 4 presents a dynamical analysis of the eccentric rotor architecture under a benchtop excitation reminiscent of human arm swing during walking. The model is nondimensionalized to aid in the analysis, and a linearized system is studied to establish some of the basics of device operation. To explain some of the nonlinear phenomena, a perturbation analysis is carried out. The chapter concludes with a proposal for a resonant eccentric rotor harvester.

Chapter 5 summarizes the results of the work of this project, which focuses primarily on eccentric rotor harvesters and their potential for wrist-worn energy harvesting. Original contributions are identified and suggestions for future work are provided.

This dissertation is concluded with an appendix that provides detailed model and excitation derivations, information on simulation error convergence, exploratory metaheuristic optimization results, an alternative approach to nondimensionalization, and a survey of vibration signals from a vibration signal library. The signal survey is a reprint of a journal manuscript published in *Energy Harvesting and Systems*.

1.6 References

[1] P. D. Mitcheson, E. M. Yeatman, G. K. Rao, A. S. Holmes, and T. C. Green, "Energy harvesting from human and machine motion for wireless electronic devices," *Proc. IEEE*, vol. 96, no. 9, pp. 1457–1486, 2008.

[2] S. J. Roundy, P. K. Wright, and J. Rabaey, "A study of low level vibrations as a power source for wireless sensor nodes," *Comput. Commun.*, vol. 26, no. 11, pp. 1131–1144, 2003.

[3] G. Apostolou and A. H. M. E. Reinders, "Overview of design issues in product-integrated photovoltaics," *Energy Technol.*, vol. 2, no. 3, pp. 229–242, 2014.

[4] J. J. Carr, *Old Time Radios! Restoration and Repair*, 1st ed. Tab Books, 1991.

[5] S. Y. R. Hui, Z. Wenxing, and C. K. Lee, "A critical review of recent progress in mid-range wireless power transfer," *IEEE Trans. Power Electron.*, vol. 29, no. 9, pp. 4500–4511, 2014.

[6] H. H. Wu, A. Gilchrist, K. Sealy, P. Israelsen, and J. Muhs, "A review on inductive charging for electric vehicles," in *2011 IEEE Int. Electr. Mach. Drives Conf. (IEMDC)*, pp. 143–147, 2011.

[7] H. Basaeri, D. B. Christensen, and S. J. Roundy, "A review of acoustic power transfer for bio-medical implants," *Smart Mater. Struct.*, vol. 25, no. 12, 2016.

[8] R. L. Hills, *Power from Wind: A History of Windmill Technology*. Cambridge University Press, 1996.

[9] "Wearables Market to Be Worth $25 Billion by 2019." [Online]. Available: https://www.ccsinsight.com/press/company-news/2332-wearables-market-to-be-worth-25-billion-by-2019-reveals-ccs-insight. [Accessed: 12-Nov-2018].

[10] A. Pantelopoulos and N. G. Bourbakis, "A survey on wearable sensor-based systems for health monitoring and prognosis," *IEEE Trans. Syst. Man Cybern. Part C Appl. Rev.*, vol. 40, no. 1, pp. 1–12, 2010.

[11] K. J. Cho and H. H. Asada, "Wireless, battery-less stethoscope for wearable health monitoring," in *Proc. IEEE Annu. Northeast Bioeng. Conf. NEBEC*, vol. 2002–Janua, pp. 187–188, 2002.

[12] J. Yoo, Y. Long, L. Seulki, K. Yongsang, and Y. Hoi-Jun, "A 5.2 mW self-configured wearable body sensor network controller and a 12 μW wirelessly powered sensor for a continuous health monitoring system," *Solid-State Circuits, IEEE J.*, vol. 45, no. 1, pp. 178–188, 2010.

[13] B. Ballard, *Designing the Mobile User Experience.* Wiley, 2007.

[14] N. Thambi and A. M. Sastry, "Powering MEMS portable devices — a review of non-regenerative and regenerative power supply systems with special emphasis on piezoelectric energy," *Smart Mater. Struct.*, vol. 17, 2008.

[15] S. Lee, R. Zhang, and K. Huang, "Cognitive radio networks," *IEEE Trans. Wirel. Commun.*, vol. 12, no. 9, pp. 4788–4799, 2013.

[16] R. W. Miles, K. M. Hynes, and I. Forbes, "Photovoltaic solar cells : an overview of state-of-the-art cell development and environmental issues," *Prog. Cryst. Growth Charact. Mater.*, vol. 51, pp. 1–42, 2005.

[17] M. Chen, S. Lu, and B. Liao, "On the figure of merit of thermoelectric generators," *J. Energy Resour. Technol.*, vol. 127, no. March 2005, pp. 37–41, 2013.

[18] J. Chen, Z. Yan, and L. Wu, "The influence of Thomson effect on the maximum power output and maximum efficiency of a thermoelectric generator The influence of Thomson effect on the maximum power output and maximum efficiency of a thermoelectric generator," *J. Appl. Phys.*, vol. 79, no. 11, pp. 8823–8828, 1996.

[19] X. Lu, P. Wang, D. Niyato, D. Kim, and Z. Han, "Wireless networks with RF energy harvesting: a contemporary survey," *IEEE Commun. Surv. Tutorials*, vol. 17, no. 2, pp. 757–789, 2014.

[20] V. H. Schmidt, "Piezoelectric energy conversion in windmills," in *IEEE 1992 Ultrason. Symp. Proc.*, pp. 897–904, 1992.

[21] S. Priya, "Modeling of electric energy harvesting using piezoelectric windmill," *Appl. Phys. Lett.*, vol. 87, no. 18, 2005.

[22] R. Myers, M. Vickers, H. Kim, S. Priya, R. Myers, M. Vickers, and H. Kim, "Small scale windmill," *Appl. Phys. Lett.*, vol. 90, no. 5, 2007.

[23] T. Starner, "Human-powered wearable computing," *IBM Syst. J.*, vol. 35, no. 3.4, pp. 618–629, 1996.

[24] P. C. Shih, K. Han, E. S. Poole, M. B. Rosson, and J. M. Carroll, "Use and adoption challenges of wearable activity trackers," in *iConference 2015 Proc.*, 2015.

[25] T. J. M. Kooiman, M. L. Dontje, S. R. Sprenger, W. P. Krijnen, C. P. Van Der Schans, and M. de Groot, “Reliability and validity of ten consumer activity trackers,” *BMC Sports Sci. Med. Rehabil.*, vol. 7, no. 24, 2015.

[26] P. D. Mitcheson, “Energy harvesting for human wearable and implantable bio-sensors,” in *2010 Annu. Int. Conf. IEEE Eng. Med. Biol.*, pp. 3432–3436, 2010.

[27] C. B. Williams, R. C. Woods, and R. B. Yates, “Feasibility study of a vibration powered micro-electric generator,” in *Proc. IEE Colloq. Conf. Power Sources (Digest No. 96/107)*, 1996, pp. 2–4.

[28] C. B. Williams and R. B. Yates, “Analysis of a micro-electric generator for microsystems,” *Sensors Actuators A Phys.*, vol. 52, no. 1–3, pp. 8–11, 1996.

[29] P. D. Mitcheson, T. C. Green, E. M. Yeatman, and A. S. Holmes, “Architectures for vibration-driven micropower generators,” *J. Microelectromechanic Syst.*, vol. 13, no. 3, pp. 429–440, 2004.

[30] V. P. Generation, R. Amirtharajah, and A. P. Chandrakasan, “Self-powered signal processing using vibration-based power generation,” *IEEE J. Solid-State Circuits*, vol. 33, no. 5, pp. 687–695, 1998.

[31] C. B. Williams, C. Shearwood, M. A. Harradine, P. H. Mellor, T. S. Birch, and R. B. Yates, “Development of an electromagnetic micro-generator,” *IEE Proc. - Circuits, Devices Syst.*, vol. 148, no. 6, p. 337, 2001.

[32] W. J. Li, T. C. H. Ho, G. M. H. Chan, P. H. W. Leong, and H. Y. Wong, “Infrared signal transmission by a laser-micromachined vibration-induced power generator,” in *Proc. 43rd IEEE Midwest Symp. Circuits Syst.*, no. 2150201, pp. 236–239, 2000.

[33] J. Yun, S. N. Patel, M. S. Reynolds, and G. D. Abowd, “Design and performance of an optimal inertial power harvester for human-powered devices,” *IEEE Trans. Mob. Comput.*, vol. 10, no. 5, pp. 669–683, 2011.

[34] R. Watkins, *The Origins of Self-Winding Watches 1773 - 1779*, 2nd ed. Richard Watkins, 2013.

[35] J. Nakano, K. Komori, Y. Hattori, and Y. Suzuki, “MEMS rotational electret energy harvester for human motion,” in *J. Phys. Conf. Ser.*, vol. 660, 2015.

[36] E. Romero, M. R. Neuman, and R. O. Warrington, “Rotational energy harvester for body motion,” in *2011 IEEE 24th Int. Conf. Micro Electro Mech. Syst.*, pp. 1325–1328, 2011.

[37] M. Hayakawa, “Electronic wristwatch with generator,” US5001685 A, 1991.

[38] Q. C. Tang, Y. L. Yang, and X. Li, “Bi-stable frequency up-conversion piezoelectric energy harvester driven by non-contact magnetic repulsion,” *Smart Mater. Struct.*,

vol. 20, no. 12, 2011.

[39] Y. Naruse, N. Matsubara, K. Mabuchi, M. Izumi, and S. Suzuki, “Electrostatic micro power generation from low-frequency vibration such as human motion,” *J. Micromechanics Microengineering*, vol. 19, no. 9, 2009.

[40] N. G. Elvin and A. A. Elvin, “An experimentally validated electromagnetic energy harvester,” *J. Sound Vib.*, vol. 330, no. 10, pp. 2314–2324, 2011.

[41] M. A. Halim and J. Y. Park, “A non-resonant, frequency up-converted electromagnetic energy harvester from human-body-induced vibration for hand-held smart system applications,” *J. Appl. Phys.*, vol. 115, no. 9, 2014.

[42] M. Renaud, P. Fiorini, R. van Schaijk, and C. van Hoof, “Harvesting energy from the motion of human limbs: the design and analysis of an impact-based piezoelectric generator,” *Smart Mater. Struct.*, vol. 18, no. 3, 2009.

[43] T. Xue, X. Ma, C. Rahn, and S. J. Roundy, “Analysis of upper bound power output for a wrist-worn rotational energy harvester from real-world measured inputs,” in *J. Phys. Conf. Ser.*, vol. 557, 2014.

[44] T. Xue and S. J. Roundy, “On magnetic plucking configurations for frequency up-converting mechanical energy harvesters,” *Sensors Actuators A. Phys.*, vol. 253, pp. 101–111, 2017.

[45] J. Boland, Y.-H. C. Y.-H. Chao, Y. Suzuki, and Y. C. Tai, “Micro electret power generator,” in *Sixt. Annu. Int. Conf. Micro Electro Mech. Syst. 2003*. MEMS-03 Kyoto. IEEE, pp. 538–541, 2003.

[46] E. M. Yeatman, “Energy harvesting from motion using rotating and gyroscopic proof masses,” *Proc. Inst. Mech. Eng. Part C J. Mech. Eng. Sci.*, vol. 222, no. 1, pp. 27–36, 2008.

[47] R. Lockhart, P. Janphuang, D. Briand, and N. F. de Rooij, “A wearable system of micromachined piezoelectric cantilevers coupled to a rotational oscillating mass for on-body energy harvesting,” in *2014 IEEE 27th Int. Conf. Micro Electro Mech. Syst.*, pp. 370–373, 2014.

[48] P. Pillatsch, E. M. Yeatman, and A. S. Holmes, “A piezoelectric frequency up-converting energy harvester with rotating proof mass for human body applications,” *Sensors Actuators, A Phys.*, vol. 206, pp. 178–185, 2014.

[49] P. Pillatsch, E. M. Yeatman, and a S. Holmes, “Real world testing of a piezoelectric rotational energy harvester for human motion,” in *J. Phys. Conf. Ser.*, vol. 476, 2013.

[50] Kinetron, “Micro Generator System ‘26.4,’” 2014.

[51] Y. Rao, K. M. McEachern, and D. P. Arnold, “A compact human-powered energy

harvesting system," *Energy Harvest. Syst.*, vol. 1, no. 1–2, pp. 89–100, 2014.

[52] S. Ju and C. H. Ji, "Piezoelectric vibration energy harvester using indirect impact of springless proof mass," in *J. Phys. Conf. Ser.*, vol. 660, 2015.

[53] A. Haroun, I. Yamada, and S. Warisawa, "Investigation of kinetic energy harvesting from human body motion activities using free/impact based micro electromagnetic generator," *J. Diabetes Cholesterol Metabolism.*, vol. 1, no. 1, pp. 12–16, 2016.

[54] M. Niroomand and H. R. Foroughi, "A rotary electromagnetic microgenerator for energy harvesting from human motions," *J. Appl. Res. Technol.*, vol. 14, pp. 259–267, 2016.

[55] M. Geisler, S. Boisseau, P. Gasnier, J. Willemin, C. Gobbo, G. Despesse, I. Ait-Ali, and S. Perraud, "Looped energy harvester for human motion," *Smart Mater. Struct.*, vol. 26, no. 10, 2017.

[56] X. Zhao, J. Cai, Y. Guo, C. Li, J. Wang, and H. Zheng, "Modeling and experimental investigation of an AA-sized electromagnetic generator for harvesting energy from human motion," *Smart Mater. Struct.*, vol. 27, no. 8, 2018.

CHAPTER 2

ARCHITECTURES FOR WRIST-WORN ENERGY HARVESTING

IOP Publishing Smart Materials and Structures

Smart Mater. Struct. 27 (2018) 044001 (16pp) https://doi.org/10.1088/1361-665X/aa94d6

Architectures for wrist-worn energy harvesting

R Rantz[1], M A Halim[1], T Xue[1], Q Zhang[2], L Gu[2], K Yang[2] and S Roundy[1]

[1] University of Utah, 1495 E 100 S (1550 MEK), Salt Lake City, UT 84112, United States of America
[2] Analog Devices, Inc., 804 Woburn St, Wilmington, MA 01887, United States of America

E-mail: robert.rantz@utah.edu

Received 6 May 2017, revised 28 September 2017
Accepted for publication 20 October 2017
Published 5 March 2018

Abstract

This paper reports the simulation-based analysis of six dynamical structures with respect to their wrist-worn vibration energy harvesting capability. This work approaches the problem of maximizing energy harvesting potential at the wrist by considering multiple mechanical substructures; rotational and linear motion-based architectures are examined. Mathematical models are developed and experimentally corroborated. An optimization routine is applied to the proposed architectures to maximize average power output and allow for comparison. The addition of a linear spring element to the structures has the potential to improve power output; for example, in the case of rotational structures, a 211% improvement in power output was estimated under real walking excitation. The analysis concludes that a sprung rotational harvester architecture outperforms a sprung linear architecture by 66% when real walking data is used as input to the simulations.

Keywords: energy harvesting, metaheuristic optimization, harvester architecture

(Some figures may appear in colour only in the online journal)

1. Introduction

The mechanical substructure of a wrist-worn vibration energy harvester responsible for the absorption of kinetic energy from its environment—herein referred to as the harvester *architecture*—distinct from the particular transduction mechanism which allows for the conversion of the absorbed kinetic energy from the mechanical domain to the electrical domain, is the focus of this work. The prevailing goal of an energy harvesting architecture is to maximize the amount of kinetic energy absorbed from the environment, per unit volume, as possible over a range of input excitations; numerous novel device architectures have been developed in order to achieve this purpose.

Rotational architectures are popular for body-worn energy harvester applications [1–9], perhaps motivated by some successful commercial products with rotational architectures [10, 11], the lack of displacement limitations, and a watch-like form factor. Other architectures in the literature specialize in responding to linear forcing along a particular direction by making use of a seismic mass given one degree of translational freedom [12–16]. Some related architectures allow for a seismic mass to move in more than one dimension, or may require a nonholonomic system description [17, 18].

In spite of the numerous device architectures explored in the literature, it remains unclear if one single architecture is inherently superior to another in its capacity to absorb kinetic energy from the wrist under a range of typical excitations. One major reason for this lack of clarity is inconsistency in device volumes among the devices explored in the literature; a large device is typically capable of producing more power than a smaller device. Although comparisons of power density may provide a potential remedy, variation in the transducer technologies employed by devices in the literature serve to confound a comparison of disparate architectures; the benefits bestowed upon a device by virtue of judicious selection of a particular transducer technology may belie the disadvantages of a suboptimal choice in mechanical substructure. Decoupling the effect of each is a major difficulty when the goal is to determine a mechanical device architecture that is best suited for a particular application. Differences in parasitic losses from device to device only further complicate the issue.

Power output from harvester devices can vary wildly with the type of input excitation, and the excitations to which devices are subjected for experimental characterization differ significantly from one device to another. No standardized battery of benchtop input excitations yet exists in the literature that can allow for a proper comparison of device performance, and power output using uncontrolled inputs—such as that of arm swing during locomotion or shaking a device by hand—varies significantly from test to test even for the same device under testing, and thus cannot be used as a reliable indicator of relative device performance without a substantial population of test subjects operating under controlled conditions.

Finally, the dynamic response of the mechanical substructure of a vibration energy harvester is heavily influenced by the values of the characteristic parameters that define its design. For example, the power output of a linear resonant vibration energy harvester subjected to harmonic forcing is highly dependent on a choice of spring constant that allows for resonance with the input. How does one compare the relative merit of two dissimilar devices if one is carefully optimized for maximum power output and the other is not?

The purpose of this work is to attempt to create conditions under which a comparison of a subset of popular device architectures is as valid as possible. To this end, six simple device architectures have been selected on the basis of research interest in the literature, and a comparative analysis of these architectures under arm swing excitations has been performed to examine the relative merit of each architecture in wrist-worn energy harvesting applications.

In this work, it is not assumed that the harvester electromechanical coupling is small; thus, the backwards coupling of the transducer and its consequent effects on the mechanical dynamics cannot be ignored. Often, a linear viscous damper is employed to model the effects that the transducer has on the mechanical harvester dynamics, and the dissipative effect of this damper—herein referred to as *electrical damping*—provides a simple way to compute harvester power output; this will be the approach used for the comparative analysis presented here. By treating the energy dissipation effects that the transducer has on the mechanical dynamics in this way, the mechanical architecture may be studied as effectively 'decoupled', or independent from, the electrical domain, facilitating a comparison of mechanical architectures.

Fixing the transducer type to that which is mathematically described by a linear viscous damper may not be as restrictive a practice as it may initially appear. Firstly, a linear viscous damper can indeed represent an optimal transducer force capable of maximizing harvester power output in response to certain excitations [19, 20]. However, it would be unwise to assume the optimality of linear viscous damper transducer dynamics for all—or even most—architectures and all excitations [21–24].

More important is the observation that the effects that both piezoelectric and electromagnetic transducers have on the mechanical harvester dynamics can be effectively captured by the addition of linear damping and a shift in the harvester oscillation frequency even for nonlinear harvester architectures—at least in the case of Duffing-type oscillators [25, 26].

Because a linear viscous damper serves as a good model for low-frequency electromagnetic energy harvesting as a result of direct application of Faraday's law of induction to a purely resistive lumped element electrical domain model [27], the most narrow interpretation of this work would be limited in application to only low-frequency electromagnetic energy harvesting. However, if the observations made in [26] are permitted to extend to other nonlinear systems, such as those described in this paper, then the method used for this comparative analysis has the potential to apply to harvesters with electromagnetic, piezoelectric, and hybrid electromagnetic-piezoelectric transducers under other excitation scenarios.

2. Device architectures

Motivated by previous research efforts and commercial endeavors (see section 1), six simple device architectures are proposed for the purpose of comparative analysis: one rotational architecture, and two linear architectures, as well as counterparts with linear spring elements. Frictional losses are modeled as linear viscous in nature, with a damping coefficient b_m. As described in section 1, electrical transduction is also assumed to be linear viscous in nature, acting in parallel with the mechanical damping, with an electrical damping coefficient b_e. The total viscous damping coefficient is $b = b_m + b_e$. A discussion on the individual architectures and their mathematical models now follows.

2.1. Rotational structures

The first structure considered in the analysis, herein denoted as the *rotor, unsprung rotor,* or *unsprung rotational* structure or architecture, is comprised of an eccentric seismic mass that rotates about an axis, as in [3]. The second structure, herein denoted as the *sprung rotor* or *sprung rotational* structure or architecture, is identical to the rotor structure, except that a torsional spring acts on the mass, with a spring constant that typically causes the rotor to rest in the upper (with respect to gravity) semicircle in the absence of external input. See figure 1.

A derivation of the rotor architecture model now follows for the convenience of the reader, as well as to correct a minor error in a similar model derivation found in [3] and used in [28]. This derivation also differs from that found in [6] in its generality; instead of considering individual forcing cases, generalized forcing from arbitrary combinations of linear accelerations and rotations in the z direction (refer to figure 1) are considered. See table 1 for variable definitions.

Because the Lagrangian approach will be used to derive the equation of motion, the derivation for the rotational structure begins by considering multiple coordinate frames useful for computing the total system energy; O_0 is an inertial

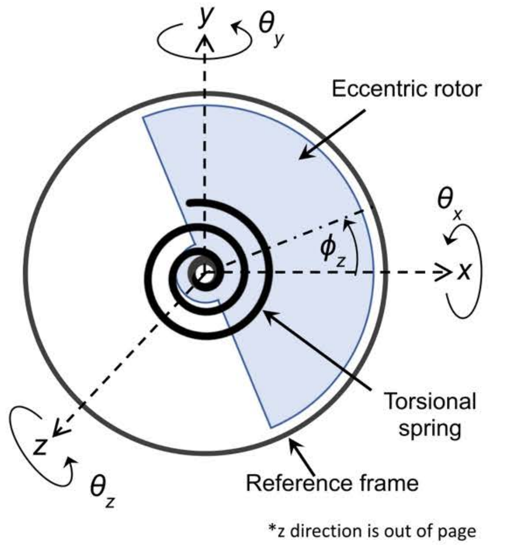

Figure 1. Illustration of the sprung rotor harvester architecture.

Table 1. Variable definitions for rotational model derivation.

Variable	Definition
m	Mass of rotor
I_g	Moment of inertia of rotor about center of gravity
b	Linear viscous damping coefficient for rotational damper
k	Linear spring constant for torsional spring
ψ	Angle of centerline of rotor as measured from basis vector $\boldsymbol{x}_0$
θ	Angle of basis vector $\boldsymbol{x}_1$ as measured from basis vector $\boldsymbol{x}_0$ ('housing angle')
ϕ	Angle of basis vector $\boldsymbol{x}_2$ as measured from basis vector $\boldsymbol{x}_1$ ('relative rotor angle')
X	Scalar displacement of O_1 in basis vector $\boldsymbol{x}_0$ direction ('absolute housing displacement')
Y	Scalar displacement of O_1 in basis vector $\boldsymbol{y}_0$ direction ('absolute housing displacement')
x'	Scalar displacement of O_2 in basis vector $\boldsymbol{x}_1$ direction
y'	Scalar displacement of O_2 in basis vector $\boldsymbol{y}_1$ direction
$\boldsymbol{p}$	Displacement vector from O_2 to center of gravity (Eccentric length, $\|\boldsymbol{p}\| = L$)
$\boldsymbol{d}_{01}$	Inter-origin vector from O_0 to O_1
d_{12}	Inter-origin vector from O_1 to O_2
${}^0R_1$	Rotation matrix from coordinate frame O_1 to O_0
${}^1R_2$	Rotation matrix from coordinate frame O_2 to O_1

reference frame, O_1 is a reference frame fixed to the rotor housing, and O_2 is a reference frame fixed to the rotating rotor mass. See figure 2. It is assumed that out-of-plane rotations contribute a negligible amount of kinetic energy to the rotor mass, and are thus ignored in the model derivation.

This derivation considers the combined effects of coordinate frame acceleration and gravity as a single effective

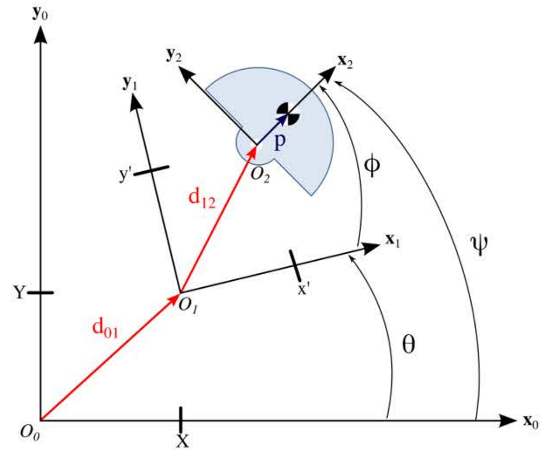

Figure 2. Schematic of rotational harvester structure used for the derivation of the equation of motion.

acceleration; the reason for this is that accelerometers typically report net acceleration—that is, total acceleration of O_1 from motion plus effective acceleration from gravity—and this approach enables the use of direct accelerometer readings as model input. Therefore, acceleration input values $\ddot{x}$ and $\ddot{y}$ (to be introduced later) are really the combination of linear acceleration and gravity, as would be reported by an accelerometer. Thus, the potential energy contribution from gravity will be ignored without any loss of model generality, making $U = 0$ in the Lagrangian.

Kinetic energy is considered at the center of mass of the rotor, and is composed of translational and rotational components:

$$T = \frac{1}{2}m\,\|\boldsymbol{v}\|^2 + \frac{1}{2}I_g\dot{\psi}^2.$$

First, locate the point ${}^2\boldsymbol{p} = \begin{bmatrix} L \\ 0 \end{bmatrix}$ in O_0. Express the displacement vector as

$$\begin{aligned}{}^0\boldsymbol{r} &= {}^0\boldsymbol{d}_{01} + {}^0R_1{}^1\boldsymbol{d}_{12} + {}^0R_1{}^1R_2{}^2\boldsymbol{p}\\ &= \begin{bmatrix} X + x'\cos\theta - y'\sin\theta + L\cos(\theta+\phi) \\ Y + x'\sin\theta + y'\cos\theta + L\sin(\theta+\phi)\end{bmatrix}.\end{aligned}$$

So far, no constraints have been placed on x' and y' (the displacements of O_2 as measured from O_1). This was done for generality. Now assume $x' = y' = 0 =$ constant, which corresponds to the axis of rotation coinciding with coordinate frame of O_1 for all time. With this assumption, differentiation of ${}^0\boldsymbol{r}$ with respect to time yields

$$\frac{\mathrm{d}}{\mathrm{d}t}{}^0\boldsymbol{r} = \boldsymbol{v} = \begin{bmatrix} \dot{X} - L\dot{\psi}\sin\psi \\ \dot{Y} + L\dot{\psi}\cos\psi \end{bmatrix}.$$

Since $\psi = \theta + \phi$, substitution of $\boldsymbol{v}$ into the expression for kinetic energy yields

$$T = \frac{1}{2}m[(\dot{X} - L\dot{\psi}\sin\psi)^2 + (\dot{Y} + L\dot{\psi}\cos\psi)^2] + \frac{1}{2}I_g\dot{\psi}^2.$$

The Lagrangian is formed by $\mathcal{L} = T - U = T$ and the Euler–Lagrange equation is invoked to find the stationarity condition, in conjunction with the Rayleigh dissipation function $R = \frac{1}{2}b(\dot{\psi} - \dot{\theta})^2$ to account for the effect of damping between O_1 and the rotor mass, to obtain the equation of motion for the rotor:

$$\ddot{\psi} = -\frac{mL(\ddot{Y}\cos\psi - \ddot{X}\sin\psi) + b(\dot{\psi} - \dot{\theta})}{mL^2 + I_g}.$$

Typically, accelerometers report acceleration values expressed in terms of a coordinate system fixed to the accelerometer. Thus, the time-varying functions $\ddot{X}(t)$ and $\ddot{Y}(t)$ (the scalar components of the vector representing the acceleration of O_1 expressed in the O_0 coordinate frame) are not useful inputs in practice. Because this acceleration is merely a vector $\boldsymbol{a} \in \mathbb{R}^2$ expressed in O_0, make use of the coordinate frame transformation to re-express this vector in O_1, denoted ${}^1\boldsymbol{a}$:

$${}^1\boldsymbol{a} = {}^0R_1^{\mathrm{T}}\begin{bmatrix}\ddot{X}\\ \ddot{Y}\end{bmatrix} = \begin{bmatrix}\cos\theta & \sin\theta\\ -\sin\theta & \cos\theta\end{bmatrix}\begin{bmatrix}\ddot{X}\\ \ddot{Y}\end{bmatrix}.$$

Make the substitutions $\ddot{X} = \ddot{x}\cos\theta - \ddot{y}\sin\theta$ and $\ddot{Y} = \ddot{x}\sin\theta + \ddot{y}\cos\theta$ then simplify:

$$\ddot{\psi} = -\frac{mL(\ddot{y}\cos(\psi - \theta) - \ddot{x}\sin(\psi - \theta)) + b(\dot{\psi} - \dot{\theta})}{mL^2 + I_g}. \tag{1}$$

Finally, note that one is often not concerned with the angle of the rotor with respect to an inertial frame; the relative angle is typically more important. Substituting $\psi = \theta + \phi$ yields

$$\ddot{\phi} = -\frac{mL(\ddot{y}\cos\phi - \ddot{x}\sin\phi) + b\dot{\phi}}{mL^2 + I_g} - \ddot{\theta} \tag{2}$$

so that the equation of motion may be solved for $\phi(t)$ directly.

The addition of a torsional spring simply adds a restoring torque to the rotational mass that is proportional to the relative angle, ϕ. The zero-torque angle is taken to be $\phi = \pi/2$ by convention. Thus, the sprung rotor architecture is described by

$$\ddot{\phi} = -\frac{mL(\ddot{y}\cos\phi - \ddot{x}\sin\phi) + b\dot{\phi} + k\left(\phi - \frac{\pi}{2}\right)}{mL^2 + I_g} - \ddot{\theta} \tag{3}$$

Note that the unsprung rotor model (2) corresponds to a special case of (3) where $k = 0$.

Average power output of a rotational device under a particular excitation signal of length T is found by solving the relevant equation of motion and numerically integrating the instantaneous power dissipated in the electrical damper over the length of the signal; that is, $P_{\mathrm{avg}} = \frac{1}{T}\int_0^T b_e\dot{\theta}^2\mathrm{d}t$.

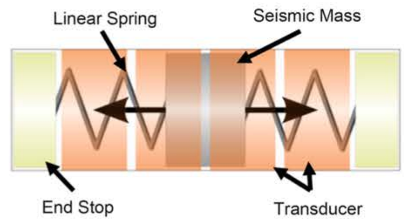

Figure 3. One-dimensional sprung linear slide architecture.

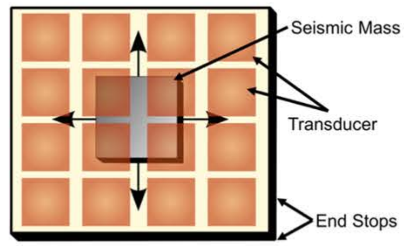

Figure 4. Two-dimensional linear slide structure.

2.2. Linear structures

Four of the six structures in the analysis are comprised of a single seismic mass free to translate within a plane with one or two degrees of freedom. The first of these four structures considered is the *one-dimensional linear slide*, comprised of a seismic mass that is free to move in a single dimension up to the length of the device, wherein impact occurs. The *one-dimensional sprung linear slide* structure or architecture is simply the one-dimensional linear slide with a restoring force provided by a spring. See figure 3. Additionally, two-dimensional analogs of the one-dimensional linear slide architectures were considered that are composed of pairs of linear damper and spring elements acting orthogonally and independently on the single seismic mass within the two available degrees of freedom. These structures are denoted as either the *two-dimensional linear slide* structure (see figure 4) or the *two-dimensional sprung linear slide* structure, depending on the presence of spring elements.

In the case of the one-dimensional slide structures, it is assumed that accelerations orthogonal to the direction of the degree of freedom have negligible impact on the dynamics and are thus ignored; the only acceleration considered in the model is that which acts along the direction in which the seismic mass may move. Additionally, the effects of rotation of the slide housing—and the resulting centrifugal forces—are also considered negligible and are ignored in the derivation. As a consequence of these simplifying assumptions, the equation of motion for the one-dimensional sprung slide may be described by the classical

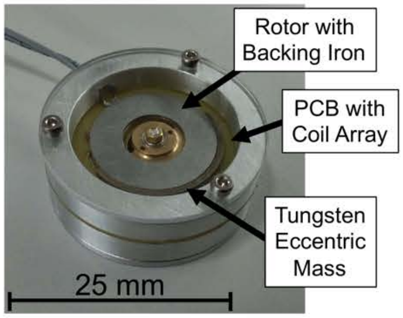

Figure 5. Sprung (and unsprung) rotational prototype device with electromagnetic transducer.

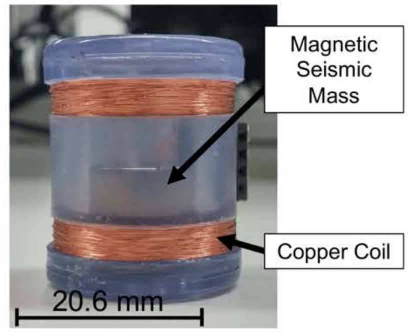

Figure 6. One-dimensional unsprung linear slide prototype device with electromagnetic transducer.

base excitation equation

$$m\ddot{z} + b\dot{z} + kz = -\ddot{a}, \tag{4}$$

where z is the displacement of the seismic mass relative to the housing, m is the seismic mass, b is the total linear viscous damping coefficient, k is the spring constant, and $\ddot{a}$ is the linear acceleration of the housing in the direction of the single degree of freedom, as in [29]. The unsprung one-dimensional slide is also modeled by (4) in the special case that $k = 0$.

It is important to note that (4) describes the motion of the seismic mass only at points where it does not make contact with the end stops. When contact occurs, it is assumed that this reaction to the end stop may be described as an impact that reverses the velocity of the seismic mass before impact, v_A, and modifies it by the coefficient of restitution $0 \leqslant e \leqslant 1$, i.e. velocity after impact $v_B = -ev_A$.

In order to model the two-dimensional slide structures, (4) is applied independently in each direction of motion using independent values of k and b in each direction.

Finally, average power output of a linear device under a particular excitation signal of length T is found by solving the relevant equation of motion and numerically integrating the instantaneous power dissipated in the electrical damper over the length of the signal; that is, $P_{\text{avg}} = \frac{1}{T}\int_0^T b_e\dot{z}^2\mathrm{d}t$.

3. Model validation

In order to corroborate the harvester architecture models developed in section 2, prototype devices were constructed and their performance quantified under various excitations.

To validate the rotational harvester models, a rotational prototype device was fabricated. An electromagnetic transducer was selected for ease of construction and for desirable transducer physics; that is, the transducer torque is approximately proportional to angular velocity. The prototype can be unsprung, or house a torsional spring. See figure 5.

Similarly, a simple one-dimensional linear slide prototype device was fabricated. Again, an electromagnetic transducer was selected. See figure 6.

The workflow for corroborating all of the models involves first characterizing the device in order to determine the various coefficient values to be used in the model—spring constants, damping coefficients, mass, etc. Then, the prototype is subjected to either a known vibrational input and the voltage output waveform across a resistive load is recorded, or is subjected to an uncontrolled input and both the output waveform and inertial data are simultaneously recorded using an inertial measurement unit (IMU). Power dissipation in a resistive load is computed. The values of the coefficients characterizing the prototype device, along with the necessary vibrational input, is fed into the corresponding model, and the dissipated power from the model is compared with the dissipated power computed from empirically measuring output voltage waveforms.

3.1. Device characterization

In order to make use of the models developed in section 2, values for the various coefficients were determined for the prototype under consideration.

For the rotational prototypes, mass, inertia and center of mass location were determined using SolidWorks Computer Aided Design software's Mass Properties tool. The values for mass estimated from this tool were checked against empirical mass measurements of individual prototype components to help ensure reasonable accuracy of the other estimated parameters. Values for torsional spring constants were estimated by observing the frequency of free oscillation of the rotor mass and recording the response with a high-speed camera. See figure 7. Values for mechanical and electrical viscous damping coefficients were also found by recording the free oscillation of the rotor mass with a high-speed camera and applying the log decrement method to the response decay envelope. This process was repeated for all spring constants used in the sprung rotor device prototype, as well as the unsprung rotor prototype which was allowed to oscillate under the effect of gravity. Finally, the obtained values for b_m and b_e for the sprung and unsprung prototypes were averaged to map the list of damping values to single-valued coefficients to be used for all simulations.

Figure 7. Experimental setup for estimating viscous damping coefficients.

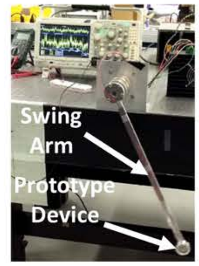

Figure 8. Swing arm experimental setup during operation.

For the linear slide prototype, the seismic mass (a cylindrical magnet) was measured with a scale. The coefficient of restitution was estimated by dropping the mass from a known height in an elongated version of the prototype and observing the height after collision with an end stop. Mechanical damping was estimated by inclining an elongated version of the prototype at a known angle with respect to gravity and recording the time taken by the seismic mass to traverse the length of the prototype; with all other coefficients known, the damping coefficient can then be backed out of (4). The electrical damping of the linear prototype was far more difficult to measure primarily because of the small range of displacements (the distance between coils) over which significant electrical damping is applied to the seismic mass. Thus, the approach for estimating this parameter involved solving for the magnetic field of the magnet using finite element software and performing numerical surface integration to estimate flux through the coils over a range of magnet displacements. The rate of change of flux with respect to displacement could then be computed and, after assuming a load resistance matched with the measured coil resistance, the electrical damping coefficient could be computed.

3.2. Swing arm test setup

A controlled input excitation can aid in the understanding of the dynamical behavior of harvester architectures, as well as provide a reasonable means for a performance comparison of prototype devices. To this end, a *swing arm* benchtop empirical testbed was developed, which is composed of a computer-controlled stepper motor driving a 0.5 m long aluminum pendulum. Prototype devices are mounted on the distal end of the swing arm and are driven using a sinusoidal excitation with a fixed swing frequency and swing angle amplitude; an input signal hereafter referred to as *pseudo-walking* input. See figure 8. A coil-resistance-matched resistive load is installed across the output terminals of the prototype under consideration in order to provide a means of power dissipation. Voltage waveforms across the resistive load are recorded using a data acquisition system. Because the stepper motor and the motor controller generate a considerable amount of electromagnetic interference in the prototype electromagnetic transducers, a low pass filter with a cutoff frequency of 10 Hz is used to filter the voltage waveforms. The voltage waveforms are then stored and exported for processing after each experimental run.

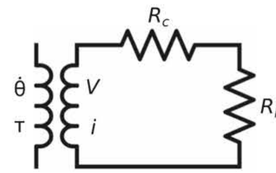

Figure 9. Lumped element model of harvester electrical domain showing power conjugate variables. Notice that coil inductance is neglected.

Figure 10. Example voltage waveform across load resistor generated by unsprung rotational prototype under pseudo-walking excitation.

To compute average power dissipation in the load resistances, the root mean square (rms) voltage across the resistive load, V_{rms}, is computed at each sampled point, and the instantaneous power at each sampled point found using $P_{\mathrm{inst}} = V_{\mathrm{rms}}^2/R_l$. Average power dissipation in the load resistance is determined by taking the mean of the regularly sampled instantaneous power values P_{inst} over the entire signal. See figure 9. An example of a load voltage waveform across coil-resistance-matched resistive load produced by the unsprung rotational prototype under pseudo-walking excitation is shown in figure 10.

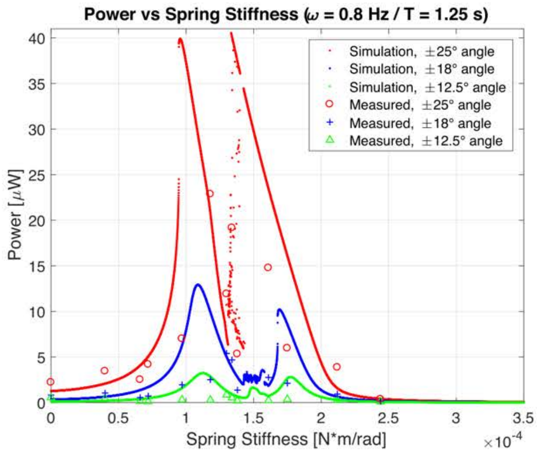

Figure 11. Average power versus torsional spring stiffness plot for pseudo-walking swing arm frequency of 0.8 Hz (1.25 s period) at multiple excitation amplitudes.

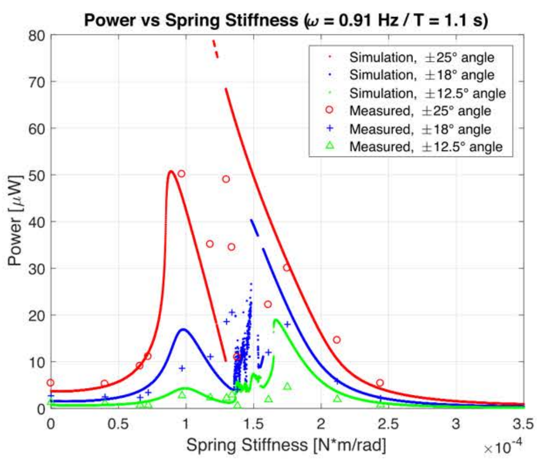

Figure 12. Average power versus torsional spring stiffness plot for pseudo-walking swing arm frequency of 0.91 Hz (1.1 s period) at multiple excitation amplitudes.

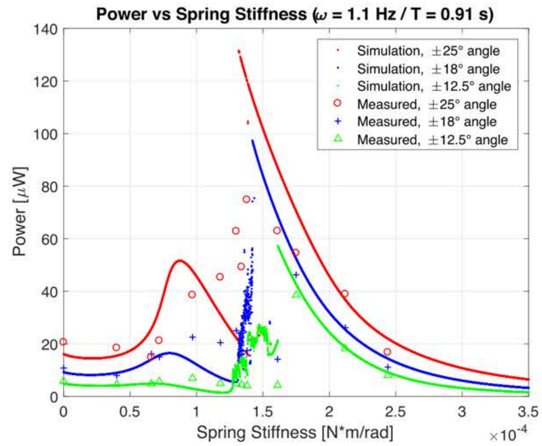

Figure 13. Average power versus torsional spring stiffness plot for pseudo-walking swing arm frequency of 1.1 Hz (0.91 s period) at multiple excitation amplitudes.

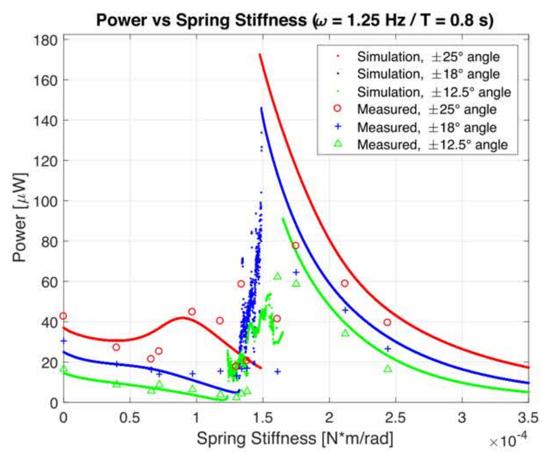

Figure 14. Average power versus torsional spring stiffness plot for pseudo-walking swing arm frequency of 1.25 Hz (0.8 s period) at multiple excitation amplitudes.

3.3. Rotational structure swing arm results

The stiffness of the torsional spring plays a major role in the dynamic response of the sprung rotor, and thus has the potential to greatly impact power output. Considering the importance of this parameter on device performance, a natural choice in evaluating the predictive power of the mathematical models is examining how well empirical measurement of average device power fits a simulated average power versus spring stiffness plot under swing arm excitation. A coil-resistance-matched resistive load of $R_l = 240\ \Omega$ was installed across the output terminals to provide a means for power dissipation and measurement. See figures 11–14, and note that the performance of an unsprung rotor device corresponds to zero spring stiffness in the plots.

In order to produce the plots found in figures 11–14, 10 000 regularly spaced spring constant values ranging from $k = 0\ \mathrm{N\,m\,rad^{-1}}$ (unsprung) to $k = 3.5 \times 10^{-4}\ \mathrm{N\,m\,rad^{-1}}$ were fed into the sprung rotor model, along with the relevant device parameters, and various types of swing arm excitation. The length of simulation was 90 s. The average power calculation did not begin until 60 s into each simulation to reduce the effect that initial conditions may have on average output power. Due to the presence of a matched load resistance, it was assumed that half of the power reported by the model was lost to the coil resistance. Consequently, a factor of ½ was applied to the average power value reported by the model.

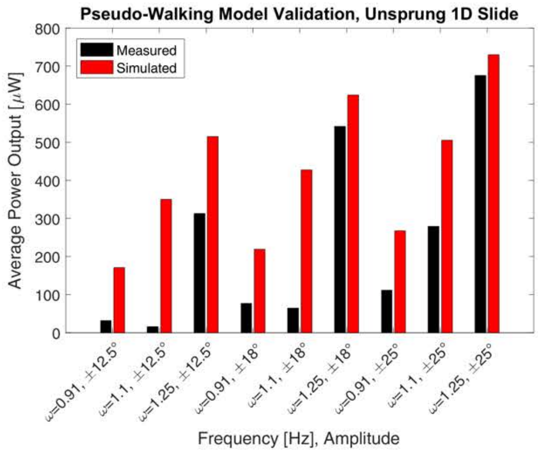

Figure 15. Measured versus simulated power output of the unsprung linear slide prototype subject to pseudo-walking excitation.

Note that the impedance due to coil inductance at the low frequencies used in this analysis is negligible.

Figures 11–14 indicate generally good agreement between simulation and empirical measurement over most spring constants. However, experimentally validating the sharp peak in power output at specific spring stiffness values was particularly challenging as only a finite number of spring stiffness values could be tested, and a measurement of the spring stiffness could not be performed with accuracy until after the spring was installed in the prototype device. Initial conditions may also play a significant role in the long-term behavior of the rotational architectures that can make empirical corroboration of the peaks difficult; see section 4.3 for further discussion.

3.4. Linear structure swing arm results

Being that the linear model proposed in section 2.2 has been corroborated under a variety of circumstances in the literature, only a simplified model validation procedure was carried out for the unsprung one-dimensional slide prototype pictured in figure 6 for the sake of completeness. The battery of pseudo-walking signals used to validate the sprung and unsprung rotational models (see sections 3.2 and 3.3) was employed to validate the unsprung linear model. A coil-resistance-matched resistive load of $R_l = 420\,\Omega$ was installed across the output terminals of the linear prototype in order to provide a means of power dissipation and measurement. A factor of ½ was applied to the average power value reported by the model, as in section 3.3. The experimental results are plotted in figure 15.

It is clear from figure 15 that the behavior of the prototype device is not captured particularly well by the model presented in section 2.2. However, there are several important points to note: firstly, the prototype was not designed to exhibit friction that is linear viscous in nature (nor was the prototype fabricated with low-friction materials; note the relatively high value for mechanical damping in table 2). It is quite possible that, at low excitation frequencies and amplitudes, coulombic friction effects—especially that of static friction—dominate the behavior, and these effects are not captured when the damping is modeled using a linear viscous damper. The increase in simulation accuracy seen in figure 15 as swing arm frequency or amplitude are increased appears to support this claim. Secondly, the electrical damping coefficient was not measured in as direct a manner as the mechanical damping coefficient for the linear prototype, as explained in section 3.1. Considering the relatively crude means by which this parameter was estimated, it is perhaps unsurprising that the simulation does not better fit the measured data over all tested excitations.

Figure 16. One of two prototype device and Shimmer3 pairs mounted on the right wrist of a participant before a human subject test.

3.5. Rotational structure human subject results

In order to further corroborate the rotational model developed in section 2, a comparison between empirically measured average power dissipation across a resistive load and simulated power dissipation under real walking excitation was desired. To accomplish this, 10 human subjects were tasked with walking on a treadmill at 3.5 mph (approximately $1.56\ \mathrm{m\,s^{-1}}$), a fast-paced walk. Two rotational prototypes were affixed together to either the left or right wrist; one unsprung prototype, and one sprung prototype with a spring constant $k = 1.05 \times 10^{-4}\ \mathrm{N\,m\,rad^{-1}}$, which simulations suggest is near optimal for this type of excitation and the level of damping present in the prototype. Once again, a coil-resistance-matched resistive load of $R_l = 240\,\Omega$ was installed across the output terminals of each rotational prototype in order to provide a means of power dissipation and measurement. Two Shimmer3 data acquisition units [30] independently sampled the output voltage waveforms across the load resistances of each prototype device while simultaneously recording IMU data at a sampling frequency of approximately 51 Hz during the walking activity. See figure 16. The small amount of data recorded before and after the walking activity were discarded for the power calculations and simulation

Table 2. Measured prototype parameters for use in model validation.

Rotational prototypes		Linear prototypes	
Parameter	Value(s)	Parameter	Value(s)
Rotating mass, m	10.7 g	Seismic mass, m	17.2 g
Inertia about center of gravity, I_g	819 g·mm^2	Coefficient of restitution, e	0.1
Eccentric length, L	1.52 mm	End stop distance, d	7.14 mm
Torsional spring constant, k	0–3.5 × 10^{-4} N m rad^{-1}	Linear spring constant, k	0
Mechanical damping, b_m	5.94 × 10^{-7} N m rad^{-1} s^{-1}	Mechanical damping, b_m	9.3 × 10^{-2} N m^{-1} s^{-1}
Electrical damping, b_e	1.87 × 10^{-6} N m rad^{-1} s^{-1}	Electrical damping, b_e	0.222 N m^{-1} s^{-1}

input. Average power dissipation in the load resistance was computed exactly as described in section 3.2.

To simulate average power dissipation in the prototype devices, the IMU data collected with the Shimmer3 device were fed into the mathematical models along with the relevant measured prototype parameters. The first 5 s of the simulation data were ignored in the average power calculation to reduce the effect that initial conditions have on power output. Again, it was assumed that half of the power reported by the model was lost to the coil resistance. Consequently, a factor of ½ was applied to the average power value reported by the model.

Figure 17 shows the correspondence between measured power output and predicted power output from the unsprung rotor prototype and model. Although the simulated power output mostly tracks the broad trends between subjects, there exists significant disagreement between empirically measured and simulated average power output for several individual subjects. The source of this disagreement is not clear, and such disagreement does not persist in simulations of the sprung rotational model, as will be discussed next.

Figure 18 shows the correspondence between measured power output and predicted power output from the sprung rotor prototype and model. The agreement between measurement and simulation is generally very good, even when making the comparison for most individual subjects. Binning the error in simulated power output for both the sprung and unsprung rotational models makes it clear that the model makes more accurate predictions for the sprung device in general, and the model is significantly less accurate in predicting power output for the unsprung device. See figure 19.

Sources of error in both the sprung and unsprung rotational device models include: inaccuracy in the measurement of prototype device parameters, finite IMU acceleration and rotation rate resolution, and inaccuracies in IMU data that are a consequence of the fact that the IMU cannot occupy the exact same location on the arm as the prototype device during testing, and thus collects inertial data that do not exactly reflect the real accelerations and rotations experienced by the prototype during testing.

Causes for the disparity in error between the sprung and unsprung rotor models, as summarized in figure 19, are less forthcoming, but could be a result of numerical instability in the governing differential equation for the unsprung rotational model that does not appear to be exhibited by its sprung counterpart, or even sensitivity to initial conditions exhibited by the unsprung rotational model under real walking data excitation. A study on the role that initial conditions play on the long-term power output for sprung and unsprung devices under human subject excitation is beyond the scope of this work. For a brief discussion on the effect of initial conditions on the rotational model under a particular pseudo-walking excitation, see section 4.3.

4. Comparative analysis

With the mathematical models experimentally validated and qualified, the next step in the analysis is to compare the relative performance of the different device architectures discussed in section 2 via simulation. Device volumes (defined as the volume swept by the seismic mass displaced through the configuration space of its center of mass) were first fixed to an arbitrary 1 cm^3 for the simulations. Tungsten seismic masses (density $\rho = 19\,000$ kg m^{-3}) were assumed for each device architecture. Mechanical damping coefficients were fixed. Two distinct input vibration types—pseudo-walking and data collected from real walking input—were considered in the comparison. Characteristic design parameters for each architecture model were optimized for each input signal in order to maximize average power output for that signal. Average power output was compared between device architectures, as well as power output sensitivity and variation in in optimal parameters.

4.1. Mechanical damping

The rotational viscous damping coefficient was fixed at an arbitrary $b_{m1} = 1 \times 10^{-7}$ N m rad^{-1} s^{-1}—a choice motivated by experience with achievable levels of viscous damping for rotational devices on the scale considered in the analysis. In order to derive a comparable damping coefficient for the linear structures, a cyclical energy balance was considered: given an arbitrary periodic relative rotor motion $\phi(t)$ with an associated value of work $W_{b_{m1}}$ over the period of motion, find a value of the linear viscous damping coefficient that, if a linear viscous damper applied a damping force proportional to the velocity of a particle positioned at the center of mass of the rotor undergoing the periodic motion $\phi(t)$, the damper attached to the particle would dissipate (do) an equivalent

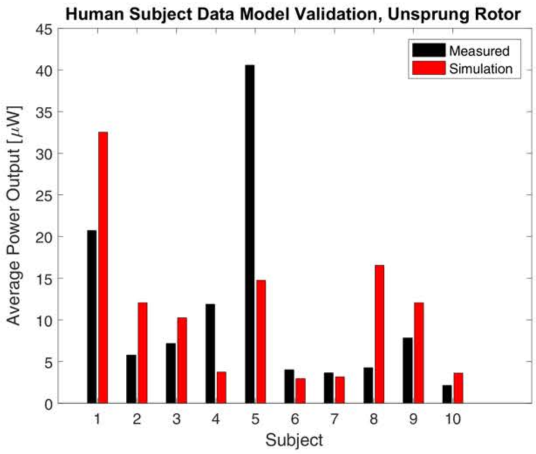

Figure 17. Measured versus simulated power output for the unsprung rotor prototype subject to real walking data.

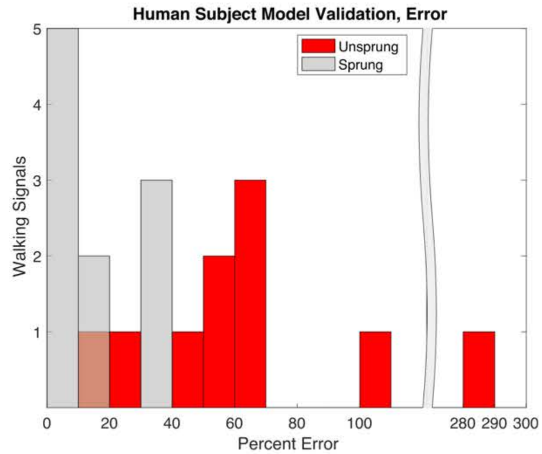

Figure 19. Histogram of error in power output for rotor models subject to real walking data.

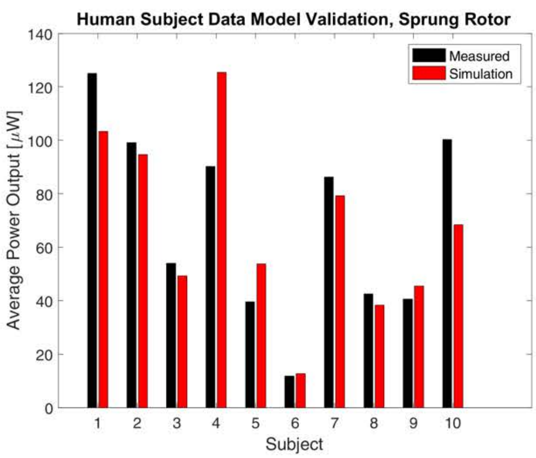

Figure 18. Measured versus simulated power output for the sprung rotor prototype subject to real walking data.

value of work, $W_{b_{m2}}$. That is,

$$W_{bm1} = W_{bm2}$$

$$\oint b_{m1}\dot{\phi}\mathrm{d}\phi = \oint b_{m2}\dot{x}\mathrm{d}x,$$

$$b_{m1}\oint \dot{\phi}^2\mathrm{d}t = b_{m2}L^2\oint \dot{\phi}^2\mathrm{d}t$$

such that $b_{m2} = b_{m1}/L^2$. Using the eccentric length of a 2 mm thick rotational device $L = 5.4$ mm, the associated linear viscous damping coefficient is $b_{m2} = 0.0034$ kg s, which was the value used for the linear devices in the comparative analysis.

4.2. Optimization

The specific set of values of an architecture's design parameters, such as electrical damping or torsional spring constant, greatly impact the nature of the dynamic response of a given architecture to excitation, and thus the performance of the architecture in terms of average power output. Consequentially, for a fair comparison of architectures, it is desirable to first find the optimal set of values for each architecture that maximize average power output in response to a particular input excitation. Then, with device volumes fixed and dissipative losses reasonably equated (see section 4.1), average power output becomes a sensible metric for gauging relative performance.

However, input signals considered in this work include those obtained from human subjects during walking that are quite complex in nature and, in the case of the rotational structures, the differential equations describing the harvester architecture are highly nonlinear. As a consequence, the relationship between design parameters, input excitation, and average power output is not known until the equations of motion describing the harvester have been numerically solved and average power output computed. In order to set up an optimization problem, an objective function was formed, which took in design parameters and input excitation data as arguments, numerically solved the relevant differential equation using zero initial conditions for the state variables and, ignoring the first portion of the solution in an attempt to reduce the effect of initial conditions, returned the average output power of the harvester. Objective functions formed using the output of numerical ordinary differential equations solvers are nonsmooth—a consequence of solution variation within the bounds of user-defined error tolerance—and many local minima appear on the objective function surface. Worse yet, larger scale local minima may also be present as a result of the problem being nonconvex, in general. Furthermore, objective function evaluations are computationally costly, as the input signals may be fairly long (40 s or more), making brute-force optimization approaches impractical. For problems involving the optimization of parameters of ordinary differential equations, such as the one described above,

Table 3. Examples of the types of optimization problems (in nonstandard form) solved for each input signal for the comparative analysis. Electrical damping b_e, spring constant k, and geometry parameters α, w, l, L serve as optimization variables, P_{avg} is the objective function that returns average power output, and x_{lb} and x_{ub} indicate lower and upper x-variable bounds, respectively.

Sprung rotational harvester		Sprung linear harvester	
$\underset{b_e,k}{\text{maximize}}$	$P_{\text{avg}}(b_e, k, \alpha)$	$\underset{b_e,k,w,l,L}{\text{maximize}}$	$P_{\text{avg}}(b_e, k, w, l, L)$
subject to	$b_{\text{lb}} \leqslant b_m \leqslant b_{\text{ub}}$	subject to	$b_{\text{lb}} \leqslant b_e \leqslant b_{\text{ub}} \quad l - L \geqslant 0$
	$0 \leqslant k \leqslant k_{\text{ub}}$		$0 \leqslant k \leqslant k_{\text{ub}} \quad lwt = V$
	$\alpha_{\text{lb}} \leqslant \alpha \leqslant \alpha_{\text{ub}}$		$d_{\text{lb}} \leqslant w, l, L \leqslant d_{\text{ub}}$

MATLAB's Pattern Search (PS) algorithm is a good solver choice [31].

In order to attempt to search through multiple basins of attraction in the search space, but allow for efficient convergence to the minimum within a promising basin of attraction, a hybrid optimization scheme was used: a genetic algorithm (GA) was used for a global search of the solution space that passed the best solution to the PS algorithm for convergence to a minimum—a routine similar to that recommended in [32]. Relatively large population sizes and elevated mutation rates were used to search the solution space with the GA, and tight mesh tolerances on the PS algorithm (in addition to tightened solution tolerances of the numerical solver) assisted in achieving consistent optimization results for a given input signal.

In addition to optimizing electrical damping coefficients and spring constants, geometric parameters were exposed as optimization variables in order to determine the geometric configuration of the architectures that maximize power output. Device thickness is a major consideration for a wrist-worn device, and this design variable will almost certainly be heavily constrained in any real application. As a result, three arbitrary thicknesses of 2, 3, and 4 mm were selected for the devices, which were fixed during the optimization procedure. In this way, unreasonably thick or thin optimization solutions were precluded from consideration, and the dimension of the solution space could be reduced by one variable. This approach also serves to make comparisons between different structures easier. If device thickness is fixed, the only remaining geometric variable for the rotational geometry is the sector angle of the rotor. For the one-dimensional linear slide structures, the total device length, the seismic mass length, and the seismic mass width are the remaining variables that define the geometry; for the two-dimensional slide structures, seismic mass length and device length in the additional dimension are also necessary to fully define the geometry.

The value for the coefficient of restitution, e, in the linear slide architectures was found to have no practical impact on device performance and was thus excluded as a design variable to be optimized. This unexpected result is a consequence of the optimization procedure itself; the optimal electrical damping for the linear models was found to be that which avoided contact with the end stops, which reduces power output. Related consequences of end stop contact are discussed in section 4.6.

Finally, in order to improve the quality and reliability of the optimization output as well as preclude impossible designs, practical bounds were placed on some of the design variables. For example, an arbitrary device length of $d_{\text{ub}} = 3$ cm was chosen to be a practical limiting case for a wrist-worn device, and a maximum rotor sector angle of $\alpha_{\text{ub}} = 2\pi$ was chosen to prevent the optimization algorithms from searching over impossible sector angles. See table 3 for examples of optimization problems that were solved in this work.

4.3. Effect of initial conditions

Being that the architectures presented in section 2 are nonlinear dynamical systems, it is reasonable to be concerned about the degree to which initial conditions may play a role in determining the long-term behavior (and, by extension, power output) of such systems under various excitations. A numerical approach was taken in an attempt to partially address this concern for the rotational architectures; 1000 regularly spaced spring constant values ranging from $k = 0$ N m rad^{-1} (unsprung) to $k = 3 \times 10^{-4}$ N m rad^{-1} were fed into the sprung rotor model, along with the relevant device parameters, to produce a plot similar to that of (the highest amplitude excitation found in) figure 13. However, for each spring constant, many ($65^2 = 4225$) initial conditions (ICs) were given to the model instead of just the zero initial condition. The ICs were evenly dispersed in a region of the phase space considered to be within nominal operating conditions for the harvester: initial angles of $-\pi/2 \leqslant \phi \leqslant \pi/2$ rad and initial angular velocities of $-6\pi \leqslant \dot{\phi} \leqslant 6\pi$ rad s^{-1}, including the origin. The simulation output is captured in the plot found in figure 20.

The plot in figure 20 suggests that there are multiple distinct orbits that persist long after the start of the simulation that produce disparate values of power. However, most of the harvester orbits described in the plot that correspond to various nonzero ICs coincide with the points that correspond to the zero initial condition, including some of the highest power orbits. This suggests that, although initial conditions do indeed play a role in the steady state dynamics of the sprung rotational architecture for certain spring stiffness values, this role does not serve to advantage the rotational architecture unfairly when zero initial conditions are assumed in the optimization procedure described in section 4.2. Furthermore, the existence of multiple steady state power values seen in figure 20 provides a plausible explanation for the

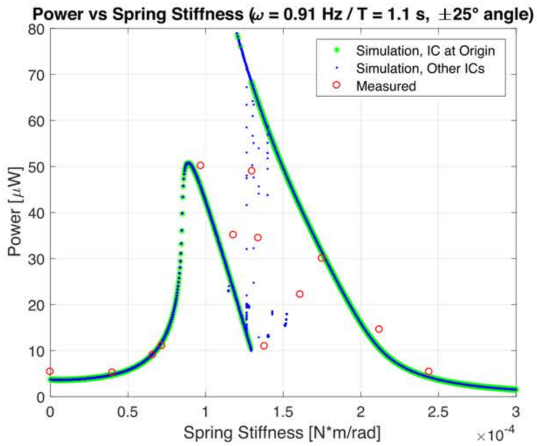

Figure 20. Power versus spring stiffness for multiple ICs. Note that for some values of spring stiffness, there are multiple stable periodic orbits that produce different mean power values.

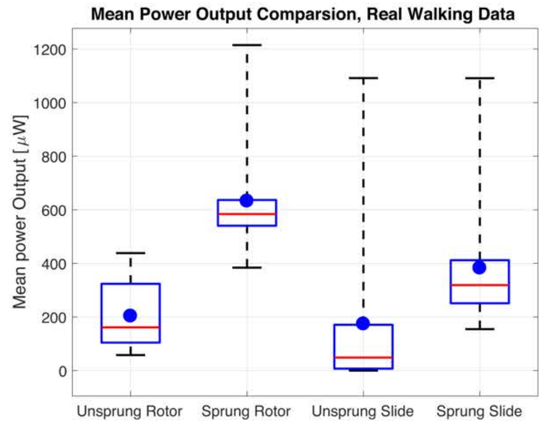

Figure 21. Box plot indicating the median, maximum, and minimum average power output for each device, along with quartiles. Mean average power output is indicated with a blue circle.

disagreement between simulation and experimental measurement seen for mid-range values of spring stiffness in figures 11–14.

The simulation-based analysis described in this section is by no means exhaustive. Generating the plot found in figure 20 is very computationally expensive, and further analysis focusing on the dynamics of the rotational system is required to better understand the nuances of this behavior—this is beyond the scope of this work.

4.4. Pseudo-walking

The first optimization routines were applied to the linear and rotational device models described in section 2 under a synthesized pseudo-walking input (see section 3.2) with a swing period of 1.1 s ($\omega \approx 0.91$) and a swing arm amplitude of $\pm 18°$. The computer-generated signals were 40 s in length, and the first 10 s of the harvester response were ignored in the calculation of average power to reduce the effect that initial conditions may have on the average output power. The primary results of the optimization can be found in table 4.

The results of the optimization across device thickness in table 4 are unsurprising; with device volumes held constant, the rotational structures benefit from an increased distance from the rotating center to the center of mass of the rotor, increasing the lever arm on which linear forces act. Thus, under the pseudo-walking signal, table 4 suggests that a thinner rotational device outperforms a thicker rotational device. The same scaling relationships are not shared among the linear devices, which is also unsurprising; if the thickness of a linear structure is constrained, the same seismic mass can be achieved by increasing the width of the device.

In all cases, sprung and unsprung, rotational and linear, the optimal design variables for geometry converged to the same point: the seismic mass consuming ½ of the total device volume. For rotational devices, this suggests that the optimal sector angle is 180° and, for linear devices where the width of the seismic mass is the same as the device width, this suggests that the seismic mass should be ½ the total device length.

Missing from table 4 are the optimized power output results from the two-dimensional linear slide device architectures; this is because these architectures consistently converge upon the optimal one-dimensional linear slide architecture parameters during optimization, suggesting that the additional degree of freedom does not result in increased harvester performance over the analogous one-dimensional architectures. For this reason, the two-dimensional linear slide architectures were omitted from further analysis after this stage of optimization.

It is clear from table 4 that the addition of a spring can greatly increase the mean output power of rotational devices under pseudo-walking input; for a 2 mm device thickness, the increase in mean power is approximately 851%. For linear devices, however, no increase in mean power output is observed at all. Notice that for a 2 mm device thickness, the one-dimensional linear slide architectures outperform the sprung rotational architecture by 21% under pseudo-walking excitation. It is important to note that the mean linear acceleration of the pseudo-walking signal along the direction of the single degree of freedom of the one-dimensional linear slide architecture is zero; this fact has implications on device performance that are discussed in section 4.6.

4.5. Real walking data

The real walking data collected from the wrists of 10 human subjects during a controlled 3.5 mph walking experiment (see section 3.5) were used as input to the rotational and linear device models described in section 2 to allow for a comparison of structures under real walking excitations. The optimization scheme described in section 4.2 was applied to each architecture for every individual input, so that the maximum average power output for all architectures was determined for every subject. However, it should be noted that the results presented in section 4.3 suggest that the

Table 4. Mean power output under pseudo-walking input for optimized structures with varying device thicknesses.

Thickness	Unsprung rotor mean power	Sprung rotor mean power	Unsprung 1D slide mean power	Sprung 1D slide mean power
2 mm	38.8 μW	369 μW	448 μW	448 μW
3 mm	30.5 μW	295 μW	448 μW	448 μW
4 mm	25.8 μW	253 μW	448 μW	448 μW

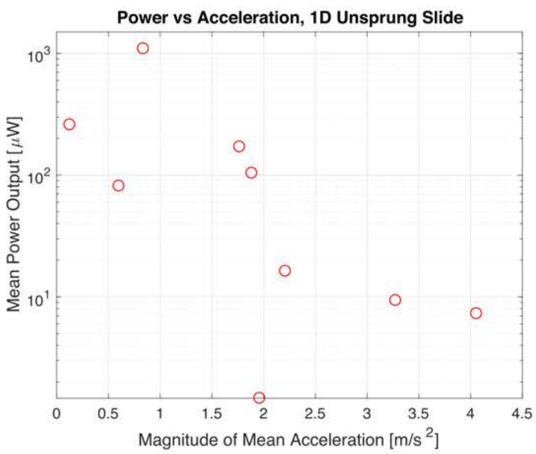

Figure 22. Semi-log plot of average power dissipation versus mean walking signal acceleration magnitude for the optimized unsprung slide.

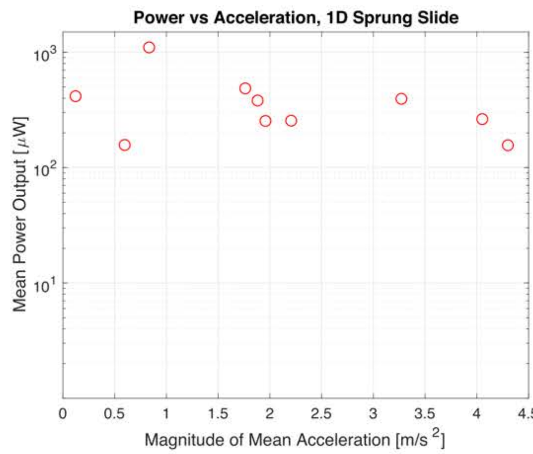

Figure 23. Semi-log plot of average power dissipation versus mean walking signal acceleration magnitude for the optimized sprung slide.

optimal geometric configuration of all harvesters ensures that the seismic mass consumes ½ of the total device volume. Running the optimization routine using other pseudo-walking signals or real walking data not discussed in this analysis suggest that this configuration is optimal regardless of the input excitation. Thus, in order to reduce the dimension of the solution space, all geometric parameters were fixed to this presumed optimal geometric configuration. The results of this study are presented in figure 21.

The results summarized in figure 21 indicate that the addition of a spring to rotational structures improves mean power output by an average of 211% under real walking excitation. For the linear structures, the addition of a spring improves power output by an average of 120% under real walking excitation. Finally, the sprung rotational architecture outperforms the sprung linear architecture by approximately 66% on average under real walking excitation.

A more thorough discussion regarding the performance of the one-dimensional slide structures can be found in section 4.6.

4.6. Power variation of the one-dimensional linear slide

The variation in power output for the one-dimensional unsprung linear slide under real walking excitation is very large relative to the other structures, as can be seen in figure 21. The trajectories of the seismic mass under these excitations appear to indicate that, if a significant *acceleration bias* exists in the input signal—that is, a nonzero mean acceleration over the length of the signal—the seismic mass tends to come to rest against the end stops of the device for a significant portion of the input signal. As a consequence, the average power output decreases. The presence of this acceleration bias in real walking signals may be explained by a tendency for the arm to swing about a nonzero angle with respect to gravitational acceleration, unlike a simple pendulum [33, 34], resulting in a nonzero net acceleration acting on the mass over the length of the signal. Such an inverse relationship between power output and acceleration bias appears to be demonstrated in figure 22, whereby the average power output of the optimized one-dimensional unsprung linear slide is plotted against the magnitude of the mean acceleration of the signal. A similar plot for the optimized one-dimensional sprung linear slide is given in figure 23. The magnitude (absolute value) was specifically considered because the orientation of the *x*-axis of the Shimmer3 device changes depending on whether the right or left wrist of the subject was used for the walking experiment described in section 3.5.

As the magnitude of the acceleration bias increases, the seismic mass is more likely to rest against an end stop for a significant duration of the signal, thereby reducing mean power output. Operating under this assumption, it is reasonable to assume that the addition of a spring, and thus a restoring force that tends to move the mass towards the center of the slide, should reduce the effect that the acceleration bias has on power output, as the restoring force tends to keep the

Table 5. Comparison of power output when architectures are individually optimized for each signal and power output when a single compromise solution is employed for the design parameters.

	Unsprung rotor	Sprung rotor	Unsprung 1D slide	Sprung 1D slide
Mean power, individual optimization	204 μW	636 μW	174 μW	383 μW
Mean power, compromise	168 μW	513 μW	138 μW	276 μW
Power reduction	18%	19%	21%	28%

mass away from the end stops. Figure 23 appears to support this claim, as the relationship between the magnitude of the acceleration bias and mean power output is far less pronounced for the sprung linear slide than it is for the unsprung linear slide.

The results presented in table 4 become more understandable when operating under this acceleration bias hypothesis; the acceleration bias of all pseudo-walking signals is zero, as the driven pendulum on which the pseudo-walking signal is based oscillates about an angle that is collinear with respect to gravitational acceleration. The linear slide structures operate with great efficacy under these conditions, producing greater power output when compared to the rotational structures under this excitation. With no restoring force necessary to compensate for nonzero acceleration bias, the spring constant of the sprung linear slide architecture approaches zero during optimization, and the power output of the sprung and unsprung slide structures converge.

Finally, the acceleration bias hypothesis may also explain why the two-dimensional linear slide structure converges to the one-dimensional analog during optimization under pseudo-walking excitation, as mentioned in section 4.3: the acceleration bias in the additional direction of motion is approximately that of Earth's gravitational acceleration, which is large relative to the orthogonal direction of motion. If it is indeed the case that it is difficult for the linear slide structures to generate power under a large acceleration bias, then it is not surprising that the optimized geometric configuration of the two-dimensional slide is to maximize displacements in a direction perpendicular to that of gravity. Thus, the optimal two-dimensional slide becomes a one-dimensional slide.

4.7. Variation in optimal parameters

Thus far, the power output of each device under consideration in the comparative analysis has been accomplished by using the set of device parameters that optimizes power output for each input signal. Fortunately, it appears that a single set of geometric parameters is optimal for all architectures under any input excitation (see section 4.3). However, this is not the case for the remaining design parameters: the electrical damping coefficient and (when applicable) spring stiffness, which vary considerably from input to input in order to achieve optimality. If the use of passive components is desired (a static transducer architecture producing a single effective electrical damping coefficient, for example, or a spring of a single stiffness value), then the characteristic harvester parameters cannot change in response to the type of input excitation. As a result, the set of parameters that are optimal for one type of input signal could be significantly suboptimal for another, and harvester power output will not be maximized over both inputs.

A *compromise solution* that generates reasonably high power output over a range of input excitations using a single, unchanging set of harvester parameters is desired. One approach to obtain such a solution is to simply average the values of the optimization solutions obtained for a set of signals of interest. For this exercise, the human subject data described in section 3.5 is used as the set of input signals over which a compromise solution will be determined. The average power output of each architecture is found first by individually optimizing each architecture to maximize power output for each of the ten walking signals and averaging the results; this is identical to the procedure described in section 4.5 yielding the average power results presented in figure 21. Then, the optimal design parameters found via optimization for each architecture are averaged, producing a single set of design parameters for each architecture. Using these parameters, the average power output over the ten walking signals is again computed for each architecture. The results of this procedure are summarized in table 5.

The results presented in table 5 make it clear that not only do the rotational architectures outperform the linear architectures under real walking excitation when each parameter is optimized from signal to signal as described in section 4.5, but the rotational architectures also suffer less performance degradation when a single set of averaged design parameters is used for all walking signals. Coincidentally, the sprung rotational architecture with averaged optimal design parameters again produced an average of 66% more mean power output than the sprung linear architecture with averaged optimal design parameters.

5. Conclusions

A simulation-based comparative analysis of six vibration energy harvesting architectures was performed. This was accomplished by first deriving device models, then validating these models by virtue of experiment. An optimization procedure was employed to find the values of the device design parameters that maximized average power output under synthesized pseudo-walking input and real walking data collected from 10 human subjects during a controlled walking experiment.

For the rotational architectures, the addition of a spring greatly improved power output. Under a pseudo-walking input, average power output for the sprung structure was

851% higher than that of the unsprung structure. Under real walking input, the addition of a spring improved mean power output over the 10 walking signals by an average of approximately 211%. It is important to point out that this improvement comes at the cost of structural asymmetry, as the zero-torque position of the sprung rotational seismic mass must be in the upper half of the device volume with respect to gravity in order to realize the power improvement.

For the linear architectures, the addition of a spring gave mixed results. Under pseudo-walking excitation, optimal spring stiffness values approached zero for the sprung devices, indicating that the addition of a spring does not provide an opportunity for enhanced power output; the performance of the sprung and unsprung architectures are identical under this type of excitation. However, using real walking data as input, the addition of a spring increased mean device power output by an average of approximately 120% over the 10 walking signals, while also reducing the variance in power output between individual walking signals. The two-dimensional linear architectures were only considered in the pseudo-walking portion of the comparative analysis, as the optimal geometry was found to be identical to that of the analogous one-dimensional structures, suggesting that the additional degree of freedom does not provide a pathway for increased power output.

The sprung architectures, rotational or linear, represented the device structures capable of producing the greatest power output in the study. Under pseudo-walking excitation, both sprung and unsprung linear architectures produced 21% more mean power than the sprung rotational architecture. However, under real waking excitation, the sprung rotational architecture outperformed the sprung linear slide architecture by 66% when optimal parameters were used for each walking signal.

Finally, an averaged optimal solution was employed for all architectures to investigate the performance impact that passive components with static parameter values would have on harvester power output. Even under these circumstances, the sprung rotational architecture outperforms the sprung one-dimensional architecture by 66%.

The limited scope of the comparative analysis represents its primary limitation. A small, albeit common, subset of device architectures was examined, and nonlinear device components, such as softening or hardening springs, were excluded from the analysis. Only a limited set of excitations were used in the study, primarily to limit computational effort in searching for optimal device parameters, but also to narrow the input signals to those which appear representative of typical wrist-worn harvester excitations during human locomotion. The effect that initial conditions has on the long-term behavior of the architectures in the study was only superficially explored in the rotational architectures and, although the brief analysis suggested that the effect is minimal, assuming zero initial conditions for all architectures remains a potential shortcoming of the study. Finally, in an effort to focus on the mechanical harvester substructures, many interesting and potentially exploitable areas of research, such as active circuit manipulation techniques, were ignored.

Acknowledgments

Funding for this research was provided by the National Science Foundation under Award Number ECCS 1342070, and a generous grant from Analog Devices Inc.

ORCID iDs

R Rantz https://orcid.org/0000-0002-5805-4170
M A Halim https://orcid.org/0000-0003-3879-9017
T Xue https://orcid.org/0000-0002-3235-7536

References

[1] Nakano J, Komori K, Hattori Y and Suzuki Y 2015 MEMS rotational electret energy harvester for human motion *J. Phys.: Conf. Ser.* **660** 12052

[2] Romero E, Neuman M R and Warrington R O 2011 Rotational energy harvester for body motion *2011 IEEE 24th Int. Conf. Micro Electro Mech. Syst.* pp 1325–8

[3] Xue T, Ma X, Rahn C and Roundy S 2014 Analysis of upper bound power output for a wrist-worn rotational energy harvester from real-world measured inputs *J. Phys.: Conf. Ser.* **557** 012090

[4] Xue T and Roundy S 2017 Sensors and actuators a: physical on magnetic plucking configurations for frequency up-converting mechanical energy harvesters *Sensors Actuators* A **253** 101–11

[5] Boland J, Chao Y-H C Y-H, Suzuki Y and Tai Y C 2003 Micro electret power generator *6th Annu. Int. Conf. Micro Electro Mech. Syst. 2003, MEMS-03 (Kyoto)* (Piscataway, NJ: IEEE) pp 538–41

[6] Yeatman E M 2008 Energy harvesting from motion using rotating and gyroscopic proof masses *Proc. Inst. Mech. Eng.* C **222** 27–36

[7] Lockhart R, Janphuang P, Briand D and de Rooij N F 2014 A wearable system of micromachined piezoelectric cantilevers coupled to a rotational oscillating mass for on-body energy harvesting *2014 IEEE 27th Int. Conf. Micro Electro Mech. Syst.* pp 370–3

[8] Pillatsch P, Yeatman E M and Holmes A S 2014 A piezoelectric frequency up-converting energy harvester with rotating proof mass for human body applications *Sensors Actuators* A **206** 178–85

[9] Pillatsch P, Yeatman E M and Holmes A S 2013 Real world testing of a piezoelectric rotational energy harvester for human motion *J. Phys.: Conf. Ser.* **476** 12010

[10] Kinetron 2014 Micro Generator System '26.4' www.kinetron.eu

[11] Hayakawa M 1991 Electronic wristwatch with generator US5001685 A

[12] Tang Q C, Yang Y L and Li X 2011 Bi-stable frequency up-conversion piezoelectric energy harvester driven by non-contact magnetic repulsion *Smart Mater. Struct.* **20** 125011

[13] Naruse Y, Matsubara N, Mabuchi K, Izumi M and Suzuki S 2009 Electrostatic micro power generation from low-frequency vibration such as human motion *J. Micromech. Microeng.* **19** 94002

[14] Elvin N G and Elvin A A 2011 An experimentally validated electromagnetic energy harvester *J. Sound Vib.* **330** 2314–24

[15] Halim M A and Park J Y 2014 A non-resonant, frequency up-converted electromagnetic energy harvester from human-body-induced vibration for hand-held smart system applications *J. Appl. Phys.* **115** 094901

[16] Renaud M, Fiorini P, van Schaijk R and van Hoof C 2009 Harvesting energy from the motion of human limbs: the design and analysis of an impact-based piezoelectric generator *Smart Mater. Struct.* **18** 35001
[17] Bowers B J and Arnold D P 2009 Spherical, rolling magnet generators for passive energy harvesting from human motion *J. Micromech. Microeng.* **19** 94008
[18] Kiziroglou M E, He C, Yeatman E M and Member S 2009 Rolling rod electrostatic microgenerator *IEEE Trans. Ind. Electron. Control Instrum.* **56** 1101–8
[19] Halvorsen E, Le C P, Mitcheson P D and Yeatman E M 2013 Architecture-independent power bound for vibration energy harvesters *J. Phys.: Conf. Ser.* **476** 117–21
[20] Heit J and Roundy S 2015 A framework to find the upper bound on power output as a function of input vibration parameters *Energy Harvest. Syst.* **1** 69–78
[21] Hosseinloo A H and Turitsyn K 2014 Fundamental limits to nonlinear energy harvesting *Phys. Rev. Appl.* **4** 064009
[22] Hosseinloo A H, Vu T L and Turitsyn K 2015 Optimal control strategies for efficient energy harvesting from ambient vibrations *Proc. 54th Ann. Conf. on Decis. Control* pp 5391–6
[23] Le T T, Truong B D, Le C P and Sager S 2016 On the power optimization of the vibration-based energy harvesters under swept input acceleration *Proc. IEEE Sensors 2016* pp 1–3
[24] Truong B D, Le C P and Halvorsen E 2015 Experiments on power optimization for displacement-constrained operation of a vibration energy harvester *J. Phys.: Conf. Ser.* **660** 1–5
[25] Daqaq M F, Masana R, Erturk A and Dane Quinn D 2014 On the role of nonlinearities in vibratory energy harvesting: a critical review and discussion *Appl. Mech. Rev.* **66** 40801
[26] Karami M A and Inman D J 2011 Equivalent damping and frequency change for linear and nonlinear hybrid vibrational energy harvesting systems *J. Sound Vib.* **330** 5583–97
[27] Mitcheson P, Green T C, Yeatman E M and Holmes A S 2004 Architectures for vibration driven micropower generators *J. Microelectromechanic Syst.* **13** 429–40
[28] Rantz R, Xue T, Zhang Q, Gu L, Yang K and Roundy S 2016 Comparative analysis of wrist-worn energy harvesting architectures *J. Phys.: Conf. Ser.* **773** 012076
[29] Inman D J 2014 *Engineering Vibration* 4th edn (London: Pearson)
[30] Realtime Technologies Ltd 2016 'Shimmer User Manual Revision 3m', http://shimmersensing.com/images/uploads/docs/Shimmer_User_Manual_rev3n.pdf, (Accessed: 01-January-2017)
[31] Mathworks 2016 'Global Optimization Toolbox: User's Guide (R2016b)', http://mathworks.com/help/pdf_doc/gads/gads_tb.pdf, (Accessed: 15-September-2016)
[32] Wetter M and Wright J 2003 Comparison of a generalized pattern search and a genetic algorithm optimization method *8th Int. IBPSA Conf.* pp 1401–8
[33] Gutnik B, MacKie H, Hudson G and Standen C 2005 How close to a pendulum is human upper limb movement during walking? *HOMO- J. Comput. Hum. Biol.* **56** 35–49
[34] Kuhtz-Buschbeck J P, Brockmann K, Gilster R, Koch A and Stolze H 2008 Asymmetry of arm-swing not related to handedness *Gait Posture* **27** 447–54

CHAPTER 3

IMPLEMENTATION AND CHARACTERIZATION OF THE ECCENTRIC ROTOR ARCHITECTURE

The addition of a torsional spring to the eccentric rotor architecture, presented in Chapter 2, complicates the design of eccentric rotor harvesters significantly, and the claim of a substantial improvement in power output from the addition of the spring demands experimental verification. Although significant experimental characterization efforts were carried out in Chapter 2 for both sprung and unsprung rotational prototypes, far more were performed that have heretofore not been presented that further reify the mathematical model's predictions concerning the eccentric rotor architecture and explore some of the nuances of electromagnetic harvester design. Given that this project was executed in coordination with an industry partner, experimental demonstration of performance was given a slightly more elevated status than it might be given otherwise, and progressive improvements in prototype engineering – even if accomplished using conventional engineering practice – were a requirement. Prototype aesthetics and total device package volume were serious considerations. It is therefore appropriate that this manuscript contain a history of the prototyping efforts and additional information on experimental device characterization.

This chapter begins with some remarks on the design methodology employed to realize energy harvester prototypes. This is followed by a description of the series of prototype iterations used to corroborate models and demonstrate performance. A detailed results section that compares measured power outputs to those predicted by the mathematical model under both a benchtop "swing arm" excitation and real human subject excitation provides experimental evidence of the validity of the model and a demonstration of the improved performance that the addition of a spring yields in the eccentric rotor harvester architecture. Some conclusions drawn from the material presented in the chapter complete the discussion.

3.1 Design Methodology

A 2 cm^3 device was desired with dimensions that generally conform to those of a typical wristwatch. Initially, this volume was taken to be the total *swept volume* (volume of the rotor and transducer as the rotor coordinate moves through all points on its configuration manifold), although devices with a total package volume of 2 cm^3 were also fabricated.

The mathematical eccentric rotor model (2-3) represents the transduction of kinetic energy into the electrical domain using a linear viscous damper element. Thus, the torque applied to the rotor by the damper element is proportional to the angular velocity of the rotor, and the constant of proportionality is the linear viscous damping coefficient. As this model was developed for use in the comparative analysis first, it was desirable to then find the transducer technology that best mimicked the behavior of a viscous damper in order to corroborate the model. It is, however, worth noting that a linear viscous damper can accurately represent the effects of the extraction of kinetic energy from an energy harvester's seismic mass for transducer technologies that do not have a linear relationship between velocity and force, even in nonlinear systems [1], as discussed in Chapter 2. Freedom in the choice of transducer notwithstanding, electromagnetic transducers do exhibit a transducer force (torque) that is approximately, and sometimes exactly, proportional to velocity (angular velocity) in the case of a purely resistive electrical domain model [2], and are also fairly easy to fabricate by hand in a laboratory setting, making an electromagnetic transducer an ideal choice for validating the model and experimentally exploring dynamical behavior. The transducers used in this project are comprised of an array of permanent magnet pairs of opposing magnetization direction, and an array of tightly-wound copper coils in a wound/ antiwound configuration wired in series. Ferromagnetic components fabricated from low carbon ASTM 1008-1010 steel sheet (referred to as *backing iron*) were used to concentrate the magnetic field density produced by the magnet array. Relative motion is induced between the magnets and the coils, and a time-varying flux linkage results. The voltage V induced on a single coil of wire is then governed by Faraday's Law of induction:

$$V = \frac{d\lambda}{dt} \tag{3-1}$$

where $d\lambda/dt$ is the time rate of change of the flux linkage.

With a transducer selected, an appropriate rotor structure must be decided that can conform to the geometry of the electromagnetic transducer. Devices were designed under the general assumption that additional rotor mass and *eccentricity* (length from the rotating center to the center of mass of the rotor) will generally result in more power output, provided sufficient levels of electrical damping are present – a claim that is explored in greater detail in Chapter 4. To this end, parts for the rotor were developed with features designed to accentuate eccentricity, and dense brass (density $\rho \approx 8.7$ g cm^{-3}) and highly dense tungsten (density $\rho \approx 19$ g cm^{-3}) materials were leveraged wherever possible to improve the inertial properties.

Finally, commercial off-the-shelf clock hairsprings were used in earlier generations of the prototypes to experimentally confirm the relationship between spring stiffness and power output predicted by the mathematical model. As the total volumes of the prototype devices were reduced to something more appropriate for a commercially viable product, the integration of custom torsional springs into the designs became necessary.

3.1.1 Modeling

In order to use the mathematical model to make predictions about real prototypes, data must be collected from the prototypes in order to populate the values of all parameters in (2-3).

Mass, eccentricity, and inertia about the rotating assembly's (i.e., rotor's) center of gravity were determined using the Mass Properties tool in the SolidWorks Computer Aided Design (CAD) software in which the prototypes were designed. Predictions from the software were vetted by checking measurements of the mass (the only directly-measurable property) of each component against the software prediction, which were always in good agreement. However, real prototypes always differ from their CAD representations due to natural variations in the geometry and material of each component (and their assemblies) within the prescribed tolerance band; this represents a source of error in the values of the parameters that contributes to error in power output predictions from the model.

Measurements for viscous damping coefficients require significantly more effort to obtain, as this property is not directly measurable and varies significantly from device to device due to minute differences in each assembly. To measure mechanical damping, a linear viscous model for friction is assumed, which allows for the use of the well-known *logarithmic decrement method*. The logarithmic decrement δ is defined using the ratio between any two successive peaks for an exponentially-decreasing periodic solution $x(t)$ and is given as

$$\delta = \frac{1}{n} \ln \frac{x(t)}{x(t+nT)} \tag{3-2}$$

where $n \in \mathbb{Z}$ is the number of successive, positive peaks, and T is the period. The mechanical damping ratio may then be found by

$$\beta_m = \frac{1}{\sqrt{1 + \left(\frac{2\pi}{\delta}\right)^2}} \tag{3-3}$$

To compute the mechanical damping for the unsprung rotor, the rotor is suspended such that gravitational acceleration acts on the rotor, as it would a pendulum, and data from the small-angle oscillations are retained for the calculation of the damping. To avoid unnecessarily confounding the result with the nonlinear effect of gravity on the rotor, all sprung rotor prototypes were tested on a flat tabletop. For both types of device, a small pin was attached to the rotor and an angular dial was used to measure the angle of the rotor (Figure 3-1). The rotor was given a small initial displacement and the resultant oscillation was recorded in a video, with the numerical decay envelope data transcribed from the video for use in (3-3).

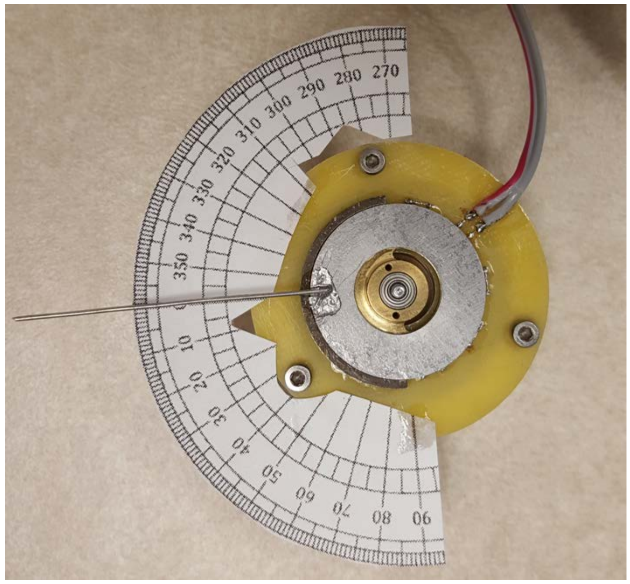

Figure 3-1 – Experimental setup for the measurement of damping ratios

The total damping, defined as the sum of the mechanical and electrical damping, was found using a similar method. A resistive load was connected to the transducer to allow for the dissipation of energy across the load, and the total damping was measured in an identical manner as with the mechanical damping alone. To extract the electrical damping ratio, the mechanical damping ratio is simply subtracted from the total damping ratio.

Obviously, electrical damping cannot be estimated using the aforementioned procedure during the design process, unlike the inertial properties, which are estimated via software. Since the electrical damping parameter is a critical design variable, it was useful to devise a method for estimating the total electrical damping of the device before committing to a design. To this end, for any proposed magnet array and coil array geometry, COMSOL Multiphysics finite element analysis software was used to perform static electromagnetic simulations of the magnetic field produced by the permanent magnet array in the transducer. To estimate the flux linkage, circular surfaces of various radii, representing coil turns, were used in the calculation of a surface integral of the component of the magnetic field density vector normal to the surface at various angular positions of the rotor (Figure 3-2). A table of the total flux vs. coil radius and rotor position could then be constructed from the integration data. A circular geometry is assumed for each coil turn such that, for a given coil geometry and magnet wire gauge, the total number of turns and the geometry of each turn can be estimated and, by interpolating the table of integration data, the flux contribution of each turn in a coil is found. The sum of all flux contributions from all turns in all coils gives the total flux linkage λ expressed as a function of the rotor angle ϕ. From (3-1), the output voltage of the transducer is then related to the rotor kinematics by

$$V = \frac{d\lambda}{dt} = \frac{d\lambda}{d\phi}\frac{d\phi}{dt} = \frac{d\lambda}{d\phi}\dot{\phi} \tag{3-4}$$

where $d\lambda/d\phi$ is the rate of change of the total flux linkage with respect to the rotor angle. Finally, a purely resistive lumped parameter model of the electrical domain is assumed, composed of transducer voltage V, coil resistance R_c, and load resistance R_l elements connected in series. Using this model, a relationship between transducer-induced torque τ and rotor velocity is given by

$$\tau = \frac{\left(\frac{d\lambda}{d\phi}\right)^2}{R_c + R_l}\dot{\phi} = b_e(\phi)\dot{\phi} \tag{3-5}$$

where the electrical damping coefficient $b_e = b_e(\phi)$ may be averaged over ϕ for a linear constant of proportionality, or used directly in the model.

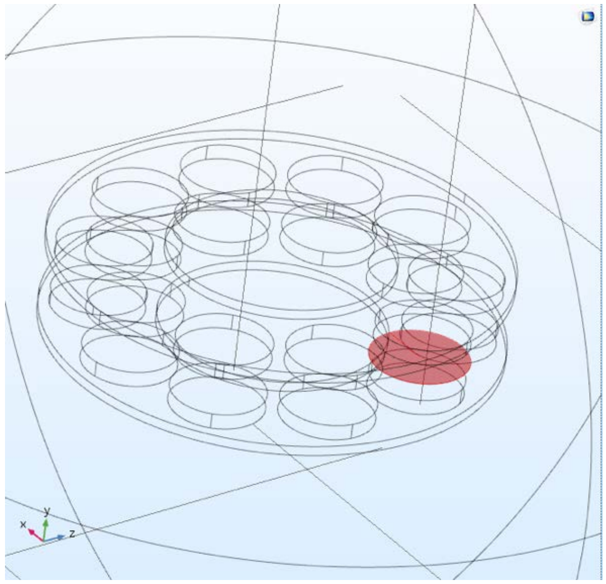

Figure 3-2 – Screenshot of software used for flux linkage estimation. The circular surface (red) was used to compute flux linkage for a coil turn using a COMSOL finite element magnetic field solution

3.2 Prototype Iterations

Early prototypes were designed primarily to demonstrate the validity of the mathematical modeling and to experiment with rotor geometries. As the iterations continued, the primary goal became a demonstration of a compact device capable of achieving a relatively high power density that also allows for a more seamless transition to a commercial product. A short description of each generation now follows.

3.2.1 First Generation

With the primary goal of determining the validity of the mathematical model, a simple, open structure was chosen for the first-generation prototype. An array of cylindrical N52 grade neodymium magnets housed in a brass rotor structure supported by ball bearings was sandwiched between two arrays of wound AWG 44 enameled copper coils and two backing iron components. A torsional spring acting between the housing and the rotor shaft on the top of the device provided the desired restoring torque. A tungsten eccentric mass served to increase the total rotor mass and eccentricity. The overall structure is presented in Figure 3-3.

The simple structure chosen for the first-generation prototype had many drawbacks that precluded the collection of much of the desired data. Because the magnet array lies between two layers of ferromagnetic backing iron material, attractive forces from the permanent magnets cause significant axial loads to develop in the bearings, inducing a large amount of friction. Even if the load had been supported by, for example, an appropriately designed thrust bearing, the design would still likely suffer from significant parasitic losses due to the formation of eddy currents in the backing iron material as the magnet array moved relative to the housing.

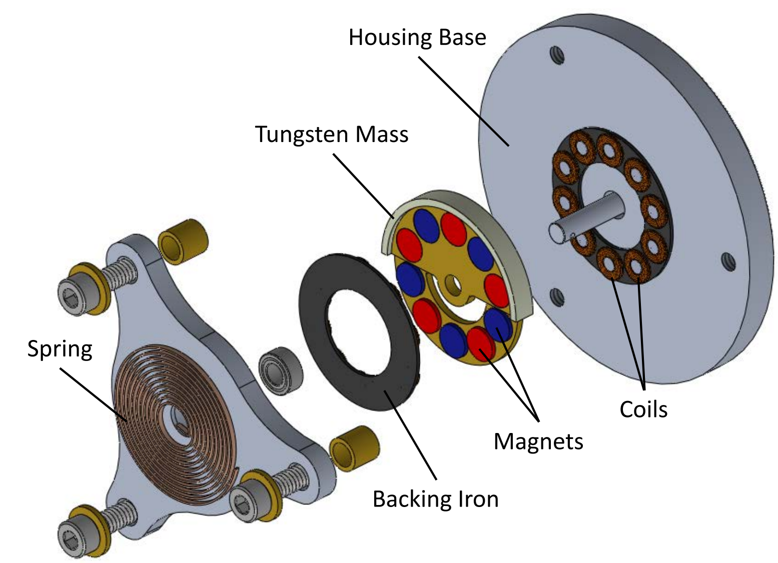

Figure 3-3 – Exploded view of first-generation prototype

3.2.2 Second Generation

The second-generation prototype design sought to remedy the axial load issues observed in the first-generation prototype. Instead of directing the load through the rolling elements of the bearings, the attractive force between the magnets and backing iron components is supported by a solid brass rotor structure; this design choice effectively results in a two-part rotor with a split tungsten eccentric mass, with a Printed Circuit Board (PCB), which carries the coil array, lying between each rotor half (Figure 3-4).

Many experiments were carried out using prototypes from the second-generation design; the rotational prototype data presented in Chapter 2 were collected entirely from prototypes of this generation, as were much of the data collected during extensive human subject experiments. A completed second-generation prototype is shown in Figure 3-5.

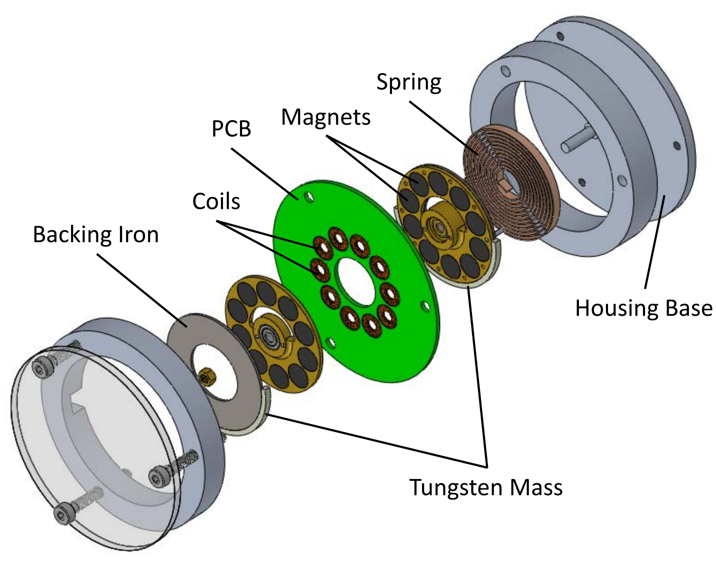

Figure 3-4 – Exploded view of second-generation prototype

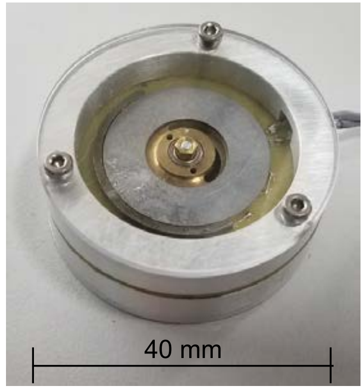

Figure 3-5 – A second-generation prototype

3.2.3 Third Generation

Following the success of the second-generation prototype in corroborating the model, the focus of the third-generation prototypes turned to improving inertial properties and making better use of the design volume. To achieve this, the PCB no longer splits the rotor into two components, allowing for a single piece of tungsten for increased rotor mass and eccentricity. The torsional spring is placed in the top of the device with a custom spring retainer for easier installation and removal. The third-generation prototypes were also the first to introduce custom annular segment neodymium magnets which, according to COMSOL simulations, increase total flux linkage slightly and have the added benefit of not requiring interstitial material to retain the magnets in the desired array configuration. The overall structure is presented in Figure 3-6.

The third generation of prototypes also represents the only generation with several *subiterations* within the generation, which varied from the original (3.0) design by components as trivial as electrical connectors (3.1) for easier data collection to massive overhauls in packaging and the introduction of custom, internally-nested torsional springs (3.2, 3.3) as well as scaled internal rotor components (3.4). The fundamental rotor structure

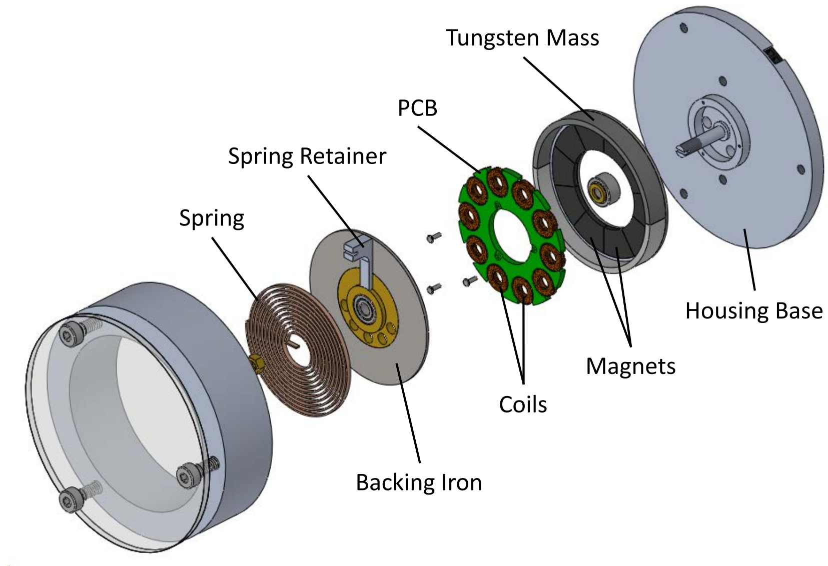

Figure 3-6 – Exploded view of the third-generation (3.1) prototype

– one that wraps around a central PCB so as to not split the tungsten eccentric mass – characterizes the third-generation prototypes, and thus remains the same throughout all of the subiterations; see Figure 3-7 for a section view illustrating this rotor design using a 3.3 device as an example.

The total volume of the first design (generation 3.0) and first subiteration (3.1) within the third generation of prototypes remained largely the same: approximately 20 cm^3. Beginning with generation 3.2, the design goal was to shrink the overall device volume by minimizing and reconfiguring the packaging. Generation 3.2 achieved a total package volume of 6.5 cm^3 by reducing the overall packaging and internally nesting the torsional spring, and 3.3 achieved a total of 5.6 cm^3 by additionally reducing the thickness of the housing base – this was all accomplished without any significant changes to the internal rotor structure, and thus no significant change in power output. In an effort to push the limit of the third-generation design, generation 3.4 was designed with a total package

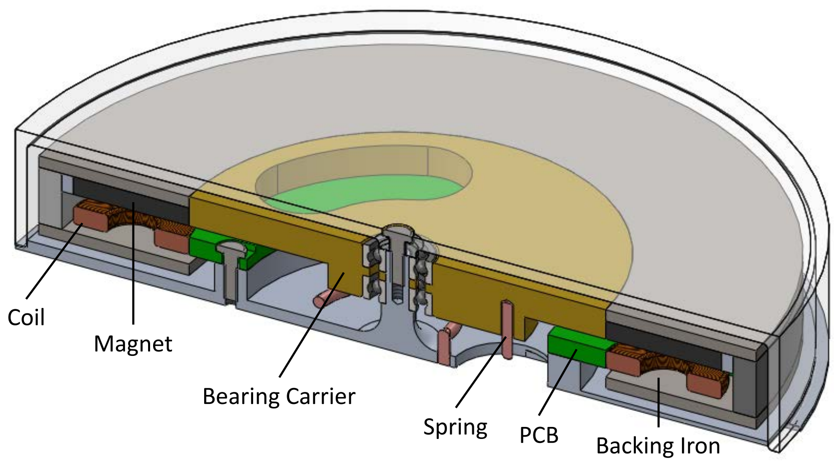

Figure 3-7 – Section view of third-generation (3.3) prototype rotor structure with reduced packaging volume and custom torsional spring

volume of approximately 2 cm^3, although this was achieved by reducing the size of the rotor at the expense of power output. See Figure 3-8 for a comparison of some of the third-generation prototypes.

3.2.4 Fourth Generation

A more ambitious internal structure was proposed for the fourth-generation prototype in order to maximize power density in an attempt to meet a target of approaching the third-generation power performance in a total device volume of 2 cm^3. To achieve this, the PCB, which supports the coil array, now comprises the majority of the rotating assembly, which allows for backing iron components to serve the dual purpose of providing most of the exterior packaging in addition to directing more of the magnetic field through the coil turns (Figure 3-9).

To create a closed electrical circuit for the coil array, current from one terminal of

Figure 3-8 – Selection of third-generation prototypes. From left to right: 3.0, 3.1, 3.2, 3.4

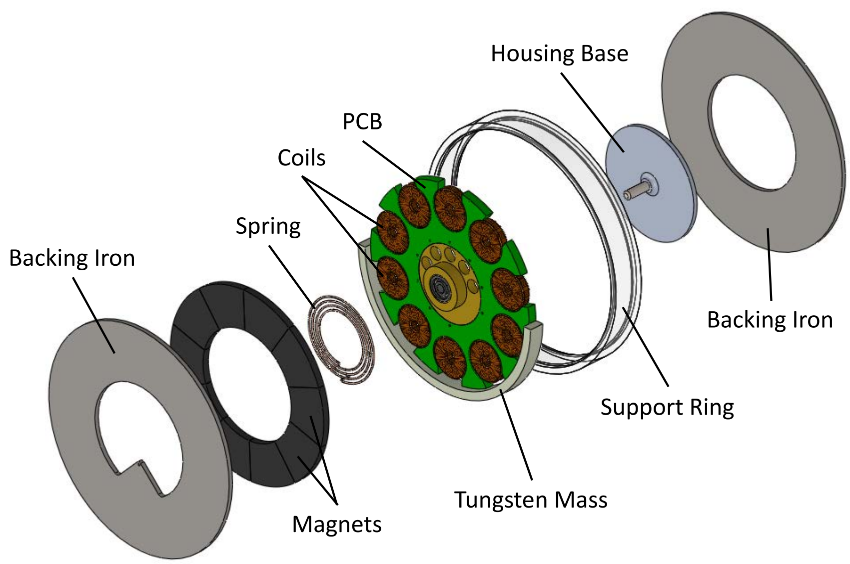

Figure 3-9 – Exploded view of fourth-generation prototype the coil array is passed through the rolling elements of the ball bearings to the housing base, which requires the use of a carbon-impregnated, electrically conductive lubricant to maintain continuity. A path for conduction to the backing iron component opposite to the housing base is made by virtue of the torsional spring. The result is a device with terminals formed by the electrically conductive upper and lower portions of the packaging in the spirit of a button cell battery. A completed fourth-generation prototype is shown in Figure 3-10.

3.3 Prototype Results

A summary of the most important prototype test results using a benchtop excitation, as well as excitation from real human subjects during locomotion, are presented here. The primary conclusion from the data is evident: the addition of a torsional spring to eccentric rotor devices allows for a substantial increase in harvester power, as predicted by the mathematical model.

Figure 3-10 – A fourth-generation prototype

3.3.1 Swing Arm Test Results

A simple, repeatable benchtop signal that is not far removed from the excitation to which a wrist-worn harvester would be subjected during typical walking motions was desired in order to corroborate the mathematical model and benchmark prototype performance; an excitation derived from the motion of a driven pendulum, herein referred to as *swing arm* excitation for its crude resemblance to arm motion during walking, was proposed to fulfill this purpose.

To create the swing arm excitation, a 0.5 m aluminum pendulum is driven by a stepper motor affixed to an optical table. The prototype device is fixed to the dorsal end of the pendulum and connected to a data acquisition system to measure transducer output (Figure 3-11). Four frequencies, selected to be representative of low- and high-frequency arm swing during walking, of 0.8 Hz, 0.91 Hz, 1.1 Hz, and 1.25 Hz were used for testing purposes, with swing arm amplitudes of 12.5°, 18°, and 25°.

To determine the relationship between power output and torsional spring stiffness for a given prototype, the mathematical model is solved using a swing arm input excitation for a series of spring stiffness values, and the average power during steady-state operation is recorded. The predictions of the model were then validated by installing a series of off-the-shelf clock hairsprings of various torsional spring stiffness values into the second-generation prototype devices. Because only a finite number of devices were fabricated, this required the installation, and removal, of many springs in a single prototype build. As a consequence of the small variations in the springs used, as well as the idiosyncrasies of each assembly after every spring installation, the degree of mechanical damping varied significantly between spring stiffness values, even for the same prototype build. This

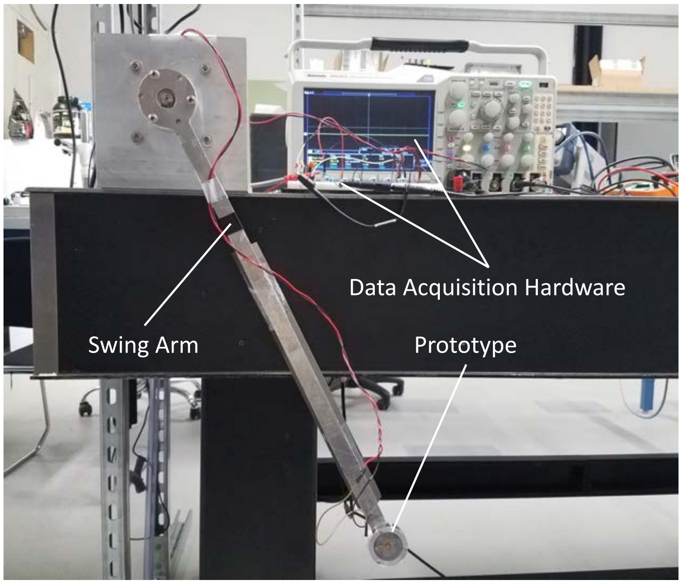

Figure 3-11 – Swing arm benchtop excitation setup

variation in the level of friction almost certainly contributes a significant amount to the varying degree of agreement with the mathematical model each spring stiffness value attains.

The results of the swing arm tests using the second-generation prototype builds are shown graphically in the plots of Figures 3-12 through 3-15. Note that the unsprung rotor output corresponds to the far left of the power vs. spring stiffness plot, at an abscissa of zero.

The theme of both the simulated and measured data presented in Figures 3-12 through 3-15 is clear: the addition of a spring can greatly enhance power output under swing arm excitation. With the exception of some points – especially for the lowest-energy excitations, where rotor amplitude is low and coulomb friction effects may be more significant than viscous effects – the experimental data generally agree well with the predictions made by the mathematical model. However, some of the highest power points in the simulation were not captured by any experimental data; confirming the existence of some of the highest-power points in the simulation is desirable to ensure that these points are not a byproduct of a poor model or related to issues in the numerical solution of the model.

The form of the curves of Figures 3-12 through 3-15 requires some remarks. Notice that there often appear two, distinct peaks in the power vs. spring stiffness plots. In examining the numerical solutions that correspond to points on each peak, it becomes clear that each peak represents a mode of oscillation; for the first peak, oscillations occur in which the rotor stays on a single side of the device. For the second peak, the rotor oscillates from one side of the device to the other, generally resulting in large displacements and thus more power output. This behavior is reminiscent of another system: the forced Duffing oscillator with a bistable nonlinearity. Intrawell and interwell oscillations are analogous to the single-sided and double-sided sprung eccentric rotor modes of oscillation and, in

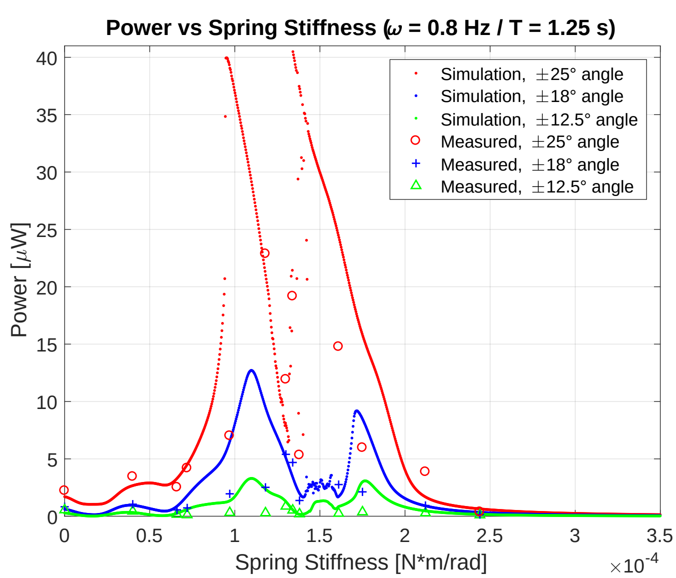

Figure 3-12 – Measured vs. simulated power output for second-generation prototype using lowest frequency (0.8 Hz) swing arm excitation

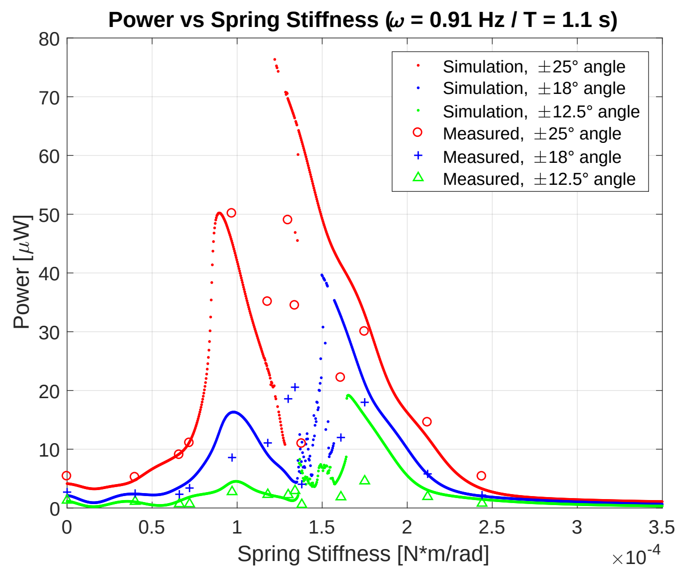

Figure 3-13 – Measured vs. simulated power output for second-generation prototype using second lowest frequency (0.91 Hz) swing arm excitation

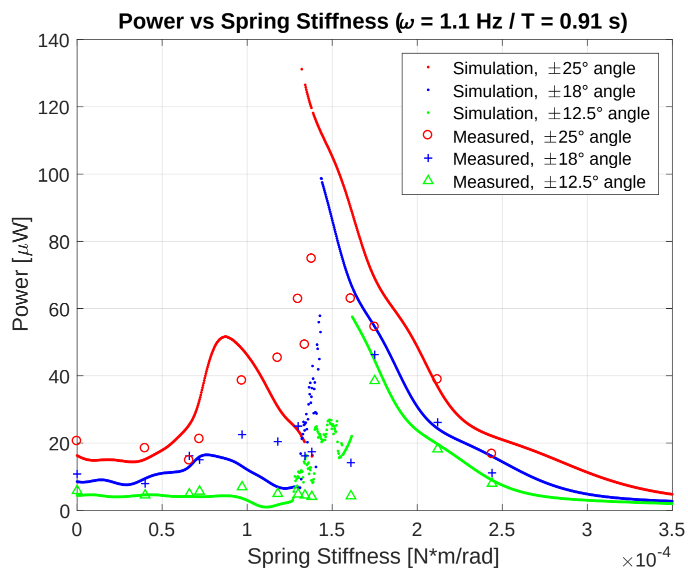

Figure 3-14 – Measured vs. simulated power output for second-generation prototype using second highest frequency (1.1 Hz) swing arm excitation

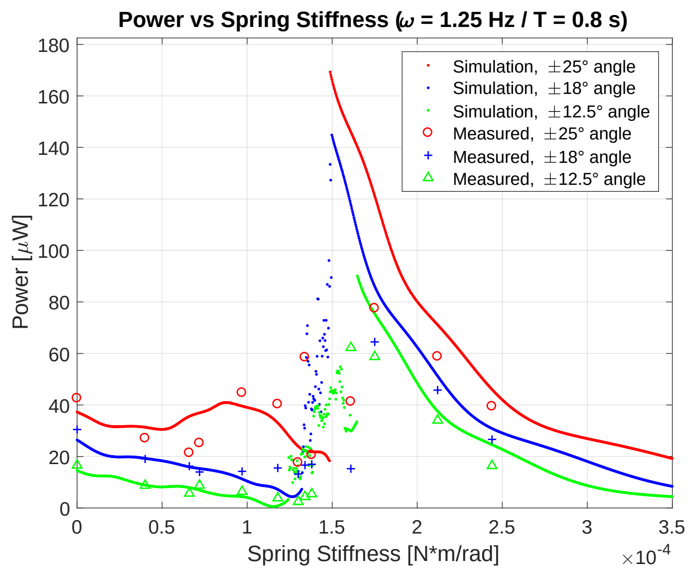

Figure 3-15 – Measured vs. simulated power output for second-generation prototype using highest frequency (1.25 Hz) swing arm excitation

addition, the Duffing oscillator can exhibit chaotic behavior at the point of transition between intrawell and interwell oscillations [3, p. 84]; if this analogy is permitted to extend to the eccentric rotor system, then this may also explain the bizarre behavior – and difficulty of empirically corroborating the simulated power output points – between the two peaks in the power vs. spring stiffness plots.

The results of the swing arm tests using the third-generation (specifically, the first design of the third generation, 3.0) prototype builds are shown graphically in the plots of Figures 3-16 through 3-19. Notice that far fewer spring stiffness values were tested than in the second-generation prototype.

The message of the data presented in Figures 3-16 through 3-19 for the third-generation (3.0) prototypes remains largely the same as with the second-generation: the addition of a torsional spring to the eccentric rotor architecture can improve power output

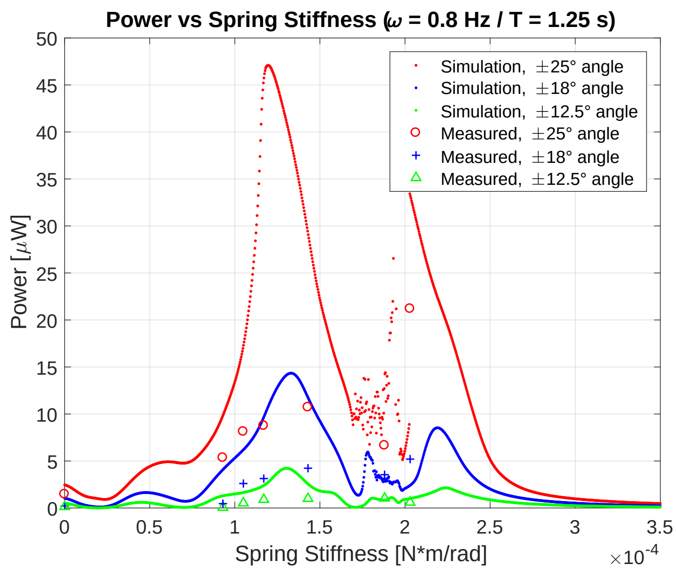

Figure 3-16 – Measured vs. simulated power output for third-generation (3.0) prototype using lowest frequency (0.8 Hz) swing arm excitation

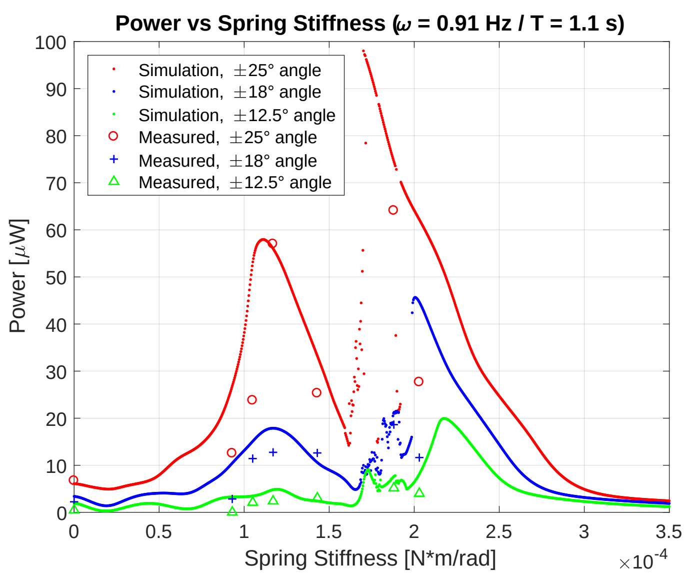

Figure 3-17 – Measured vs. simulated power output for third-generation (3.0) prototype using second lowest frequency (0.91 Hz) swing arm excitation

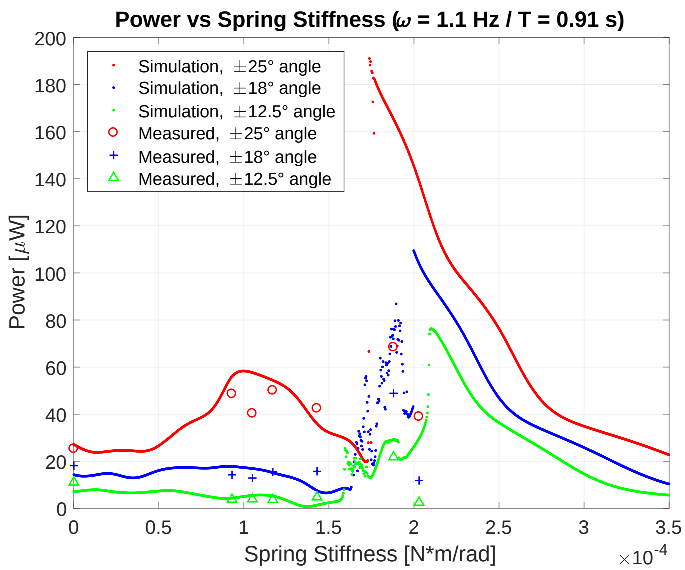

Figure 3-18 – Measured vs. simulated power output for third-generation (3.0) prototype using second highest frequency (1.1 Hz) swing arm excitation

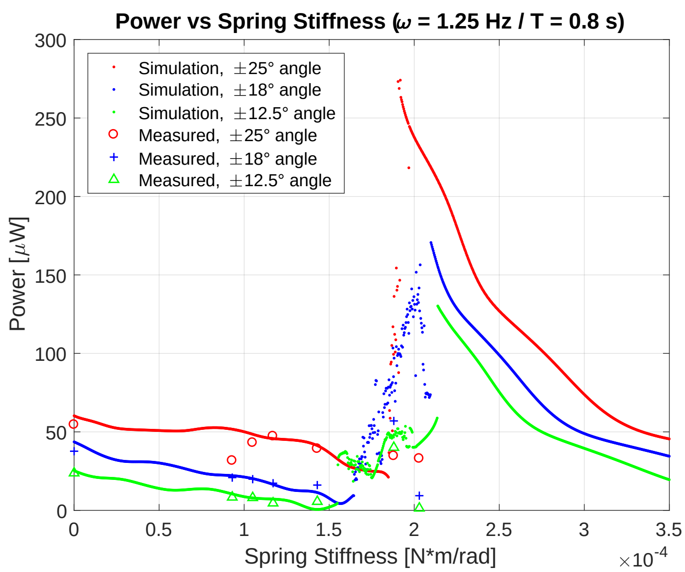

Figure 3-19 – Measured vs. simulated power output for third-generation (3.0) prototype using highest frequency (1.25 Hz) swing arm excitation over an unsprung counterpart, as predicted by the model. However, there were two major concerns with the data. First, in the case of the highest frequency swing arm excitation only, no empirical data points were observed that exceeded the unsprung device's power output – although it is worth noting that this result was predicted by the model, and appears to be explained by a lack of test points at a sufficiently high spring stiffness value (refer again to, for example, Figure 3-19). Secondly, certain spring stiffness values exhibited a concerning degree of disagreement with the model, and specific reasons as to why were difficult to ascertain. Consequently, continued investigation of the power vs. spring stiffness curve was warranted, and carried out using a subiteration in the third generation of prototypes.

The second subiteration of the third-generation prototypes (3.2) introduced custom torsional springs into a more compact design; this additional design complication, in conjunction with a desire to address concerns with the data collected using the original third-generation prototype (3.0) design, provided justification to continue to seek data to strengthen confidence in the power vs. spring stiffness curves predicted by the mathematical model. The results of the swing arm tests are summarized in Figures 3-20 through 3-23. Long lead times and significant deviation from the nominal spring stiffness values requested from the manufacturer made validation of the power vs. spring stiffness curve with many evenly distributed spring stiffness values difficult to accomplish.

In spite of the difficulties obtaining custom springs with accurate stiffness values, the presence of some of the highest-power points in the power vs. spring stiffness curve was demonstrated experimentally, as evidenced in the plots of Figures 3-20 through 3-23, confirming their existence and yielding a device with exceptionally high power output in a

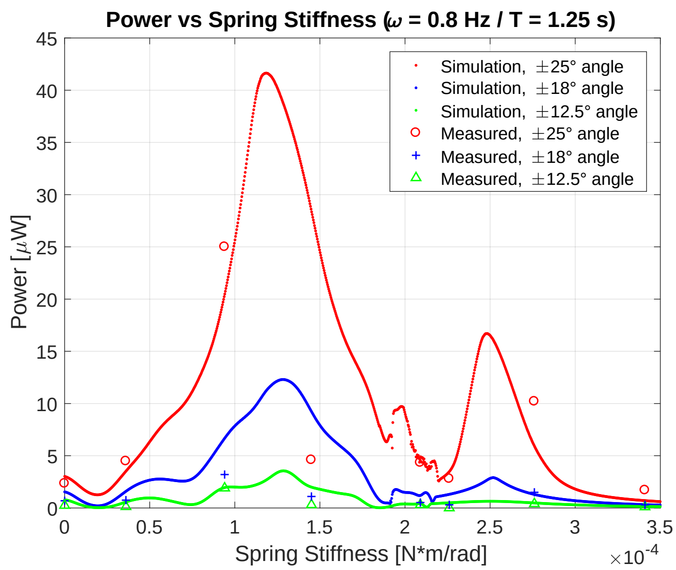

Figure 3-20 – Measured vs. simulated power output for third-generation (3.2) prototype using lowest frequency (0.8 Hz) swing arm excitation

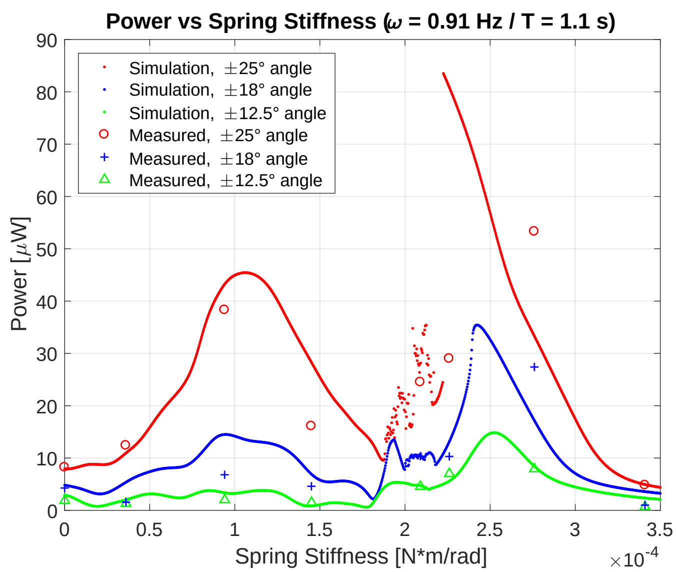

Figure 3-21 – Measured vs. simulated power output for third-generation (3.2) prototype using second lowest frequency (0.91 Hz) swing arm excitation

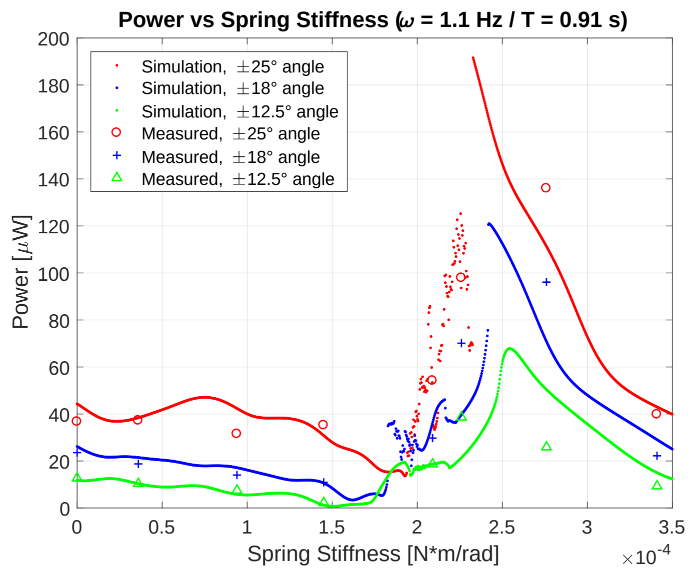

Figure 3-22 – Measured vs. simulated power output for third-generation (3.2) prototype using second highest frequency (1.1 Hz) swing arm excitation

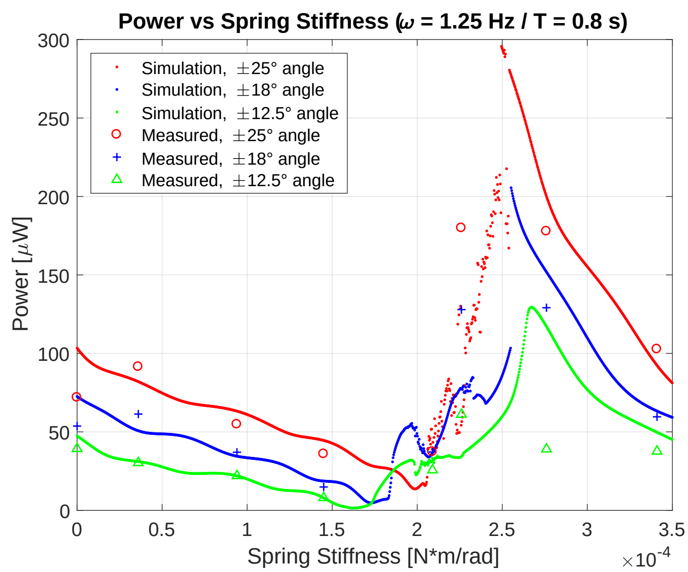

Figure 3-23 – Measured vs. simulated power output for third-generation (3.2) prototype using highest frequency (1.25 Hz) swing arm excitation relatively small package volume.

3.3.2 Human Subject Test Results

Although the benchtop swing arm excitation provides a repeatable input useful for empirically validating models and gauging prototype performance, it is still far removed from the excitation experienced by a harvester worn on the wrist during walking; the use case for wrist-worn energy harvesters thus demands empirical testing on human subjects that serves as the ultimate benchmark for harvester performance. An experimental procedure involving subjects is complicated by the normal variation in gait – and, perhaps most importantly, arm swing – that is observed during locomotion in humans [4], and it is therefore additionally necessary to control the conditions under which a subject walks as much as possible. In spite of putting controls in place, the variations in gait from subject to subject have a major impact on the performance of a prototype, as will be shown later in this section.

The human subject experiments were carried out for the second- and third-generation (3.0) prototype devices using a treadmill to control the speed. Three treadmill belt speeds of 2.5 mph, 3.5 mph, and 5.5 mph were selected, which loosely correspond to a casual walk, a brisk walk, and light jogging – however, the point of transition between different types of gait correlates with the height of the subject and along with the speed [5] and power output results would perhaps be more consistent if future tests used a dimensionless speed, such as body lengths per second, instead of a fixed speed. A spring stiffness of $1.05 \cdot 10^{-4}$ N·m·rad^{-1} was used in the second-generation sprung prototype for the entirety of the human subject tests, and a stiffness of $1.15 \cdot 10^{-4}$ N·m·rad^{-1} was used in the sprung third-generation prototype; the choice of spring stiffness was motivated by a combination of some preliminary results collected from human subjects and promising simulated power outputs using real excitation as input.

A new population of human subjects ($n = 10$) was used to test each prototype generation. The both sprung and unsprung versions of the prototype device to be tested were affixed to the wrist of the subject, along with Shimmer3 Consensys Inertial Measurement Unit (IMU) devices, which record both the voltage output of the prototypes across a resistive load using analog-to-digital converters while simultaneously recording linear accelerations in three dimensions and rotation rates about the basis vectors (Figure 3-24). Subjects were asked to walk on the treadmill for 1 minute at the desired speed, and this process was repeated for every treadmill belt speed used in the study.

Power was computed using the voltage waveform across a resistive load beginning 10 seconds after the subject achieved the desired walking speed in an effort to reduce the effects that initial rotor conditions may have on steady-state power output. The prototype was simulated using the IMU data collected during the experiment as input to the model, and the first 10 seconds of the rotor solution were neglected in the power calculation

Figure 3-24 – Experimental setup on subject’s wrist for human walking tests in order to better reflect the real power measurement procedure.

The results of the human subject experiments for the second-generation prototype are displayed graphically in Figures 3-25 through 3-27.

The results presented in Figures 3-25 through 3-27 clearly indicate that the addition of a torsional spring can greatly improve the power output of an eccentric rotor device for walking excitation. For the 5.5 mph treadmill belt speed (Figure 3-27), the addition of a spring does not have a large impact on the power output; this is most likely explained by the transition from walking to jogging that was observed for most subjects between 3.5 mph and 5.5 mph treadmill belt speeds. Both of these trends are captured by the numerical solution of (2-3) and subsequent power calculation; however, for any particular subject, there can exist serious disagreement between the measured and simulated power numbers – although this disagreement is generally reduced with the addition of a torsional spring and with higher-energy excitation. A summary of all of the human subject tests for the

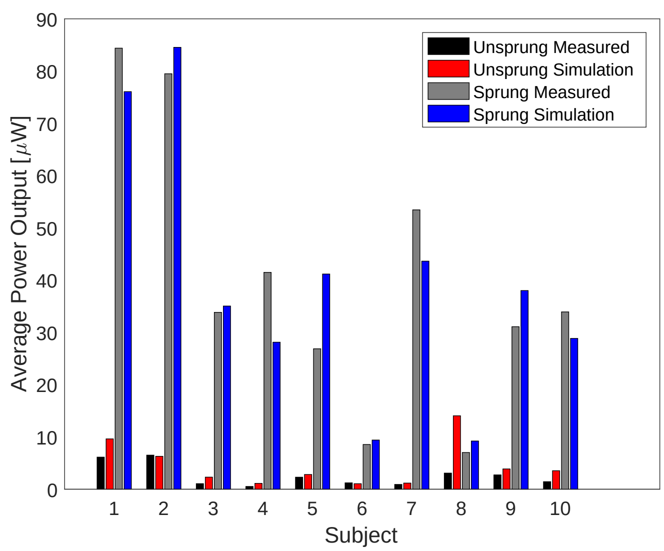

Figure 3-25 – Second-generation prototype results from human subject experiments, 2.5 mph treadmill belt speed

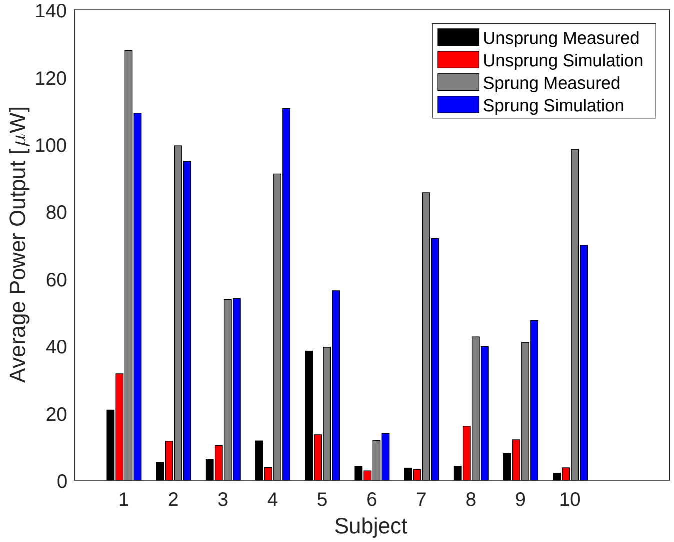

Figure 3-26 – Second-generation prototype results from human subject experiments, 3.5 mph treadmill belt speed

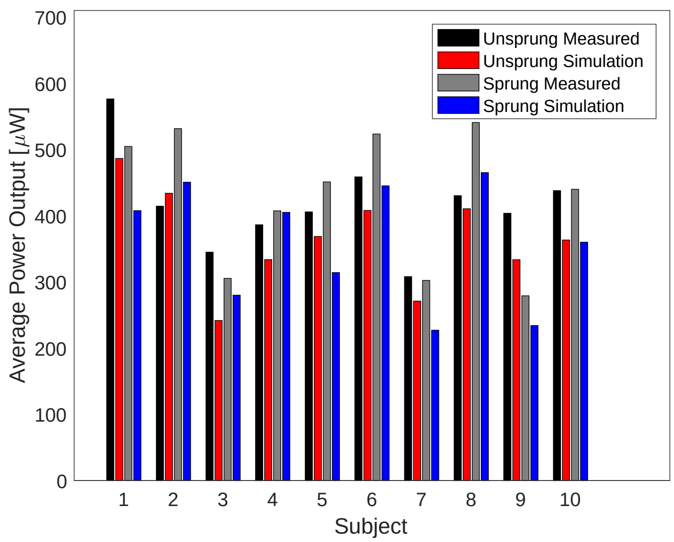

Figure 3-27 – Second-generation prototype results from human subject experiments, 5.5 mph treadmill belt speed second-generation prototypes in which the power output for all subjects has been averaged across each treadmill belt speed is given in Table 3-1.

Interestingly, although the values of simulated power sometimes exhibit large disagreement with the measured output when human subject excitation is used as input, the mean values across subjects for any particular prototype device and treadmill belt speed agree very closely for all but the highest treadmill belt speed, for which the model routinely under predicts harvester performance (Table 3-1).

Recall that the derivation of the planar rotor model (2-3) neglects the effect of rotation rates about directions not normal to the plane, which is why the inertia about the center of gravity of the rotor is scalar-valued; this appears to be a good assumption for mildly energetic human motions, like casual walking. However, for fast treadmill belt speeds (when a transition from a walking gait to a jogging or running gait occurs and arm motion becomes far more jarring), there is a valid concern that the input from the neglected rotation rates begins to represent a significant unmodeled effect. Since a consideration of the extra rotation rates as input to the model would represent a net addition of excitation to the rotor mass – likely with a commensurate increase in power output – then it is not unreasonable to speculate that the absence of the additional rotation rates as input to (2-3)

Table 3-1 – Summary of all human subject experiments using second-generation prototype devices. Power values are averaged over all subjects.

Units: μW	**Test Subjects 1 (Prototype Generation 2 Human Subject Test)**					
Device	2.5 miles per hour		3.5 miles per hour		5.5 miles per hour	
	Measured	Simulation	Measured	Simulation	Measured	Simulation
Unsprung	2.6	4.6	10.4	11.0	417	363
Sprung	40.0	38.8	69.1	68.7	428	361

contributes to the routine underprediction of power output at the highest treadmill belt speed observed in Table 3-1.

The summary in Table 3-1 indicates that the addition of an appropriately selected torsional spring increased power output by a factor of 20 for 2.5 mph walking speed, and by a factor of 7 for 3.5 mph walking speed. The addition of the spring does not appear to have much of an effect for speeds of 5.5 mph, in which most subjects adopted a jogging instead of walking gait.

The results of the human subject experiments for the third-generation prototype are displayed graphically in Figures 3-28 through 3-30.

The results presented in Figures 3-28 through 3-30 again indicate that the addition of a torsional spring can greatly improve the power output of an eccentric rotor device for walking excitation. As with the second-generation prototypes, the addition of a spring does not have a large impact on the power output in the case of a treadmill belt speed of 5.5 mph

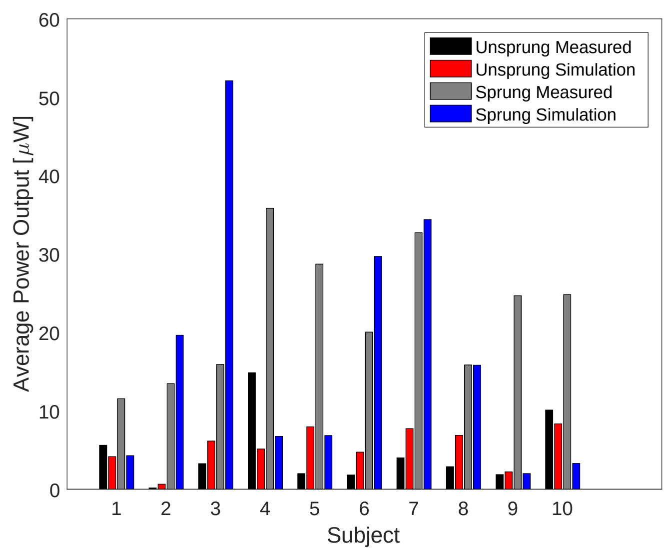

Figure 3-28 – Third-generation prototype results from human subject experiments, 2.5 mph treadmill belt speed

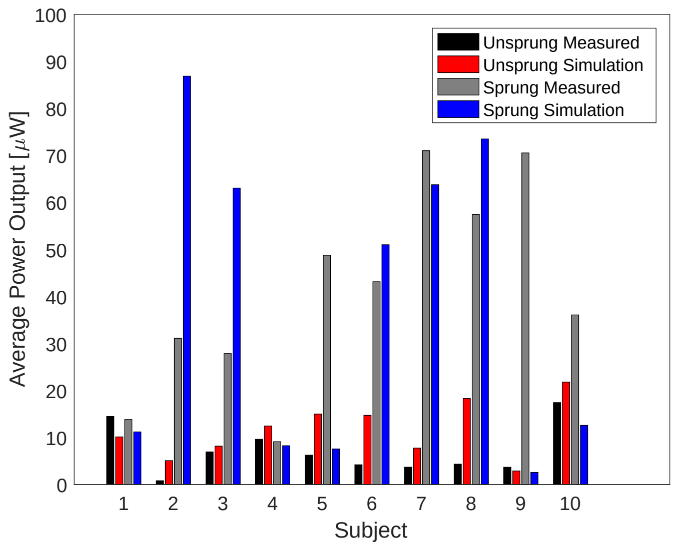

Figure 3-29 – Third-generation prototype results from human subject experiments, 3.5 mph treadmill belt speed

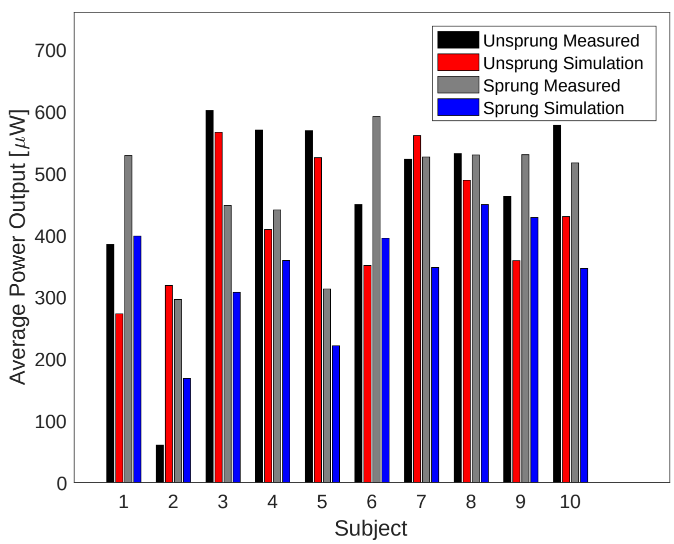

Figure 3-30 – Third-generation prototype results from human subject experiments, 5.5 mph treadmill belt speed where subjects are likely jogging (Figure 3-30). A summary of all of the human subject tests for the third-generation prototypes in which the power output for all subjects has been averaged across each treadmill belt speed is given in Table 3-2.

As with the human subject test with the second-generation prototypes, the mean values of power output for the third-generation prototype devices across subjects for a given treadmill belt speed agree very closely for all but the highest treadmill belt speed, for which the model routinely under predicts harvester performance (Table 3-2).

Also, as with the second-generation prototypes, Table 3-2 shows that in the case of the third-generation prototypes, the addition of a torsional spring can greatly enhance power output under 2.5 mph and 3.5 mph walking excitations and has no significant impact on power output for the excitation at 5.5 mph.

3.4 Conclusions

The addition of a torsional spring with appropriate spring constant can greatly enhance the power output of eccentric rotor energy harvesters when swing-arm excitation is considered. The enhancement in power output appears to be due to the development of a bistable potential caused by a combination of gravitational and spring effects on the rotor.

Table 3-2 – Summary of all human subject experiments using third-generation prototype devices. Power values are averaged over all subjects

Units: µW	**Test Subjects 2 (Prototype Generation 3 Human Subject Test)**					
Device	2.5 miles per hour		3.5 miles per hour		5.5 miles per hour	
	Measured	Simulation	Measured	Simulation	Measured	Simulation
Unsprung	4.7	5.5	7.1	11.6	473	418
Sprung	22.4	17.1	40.9	38.2	472	343

By selecting an optimal spring constant, power output is increased many times over that of the unsprung rotor with the same excitation. This behavior is predicted by the model, and experimental data generally conform to the model predictions well.

The addition of a torsional spring with appropriate spring constant can also greatly enhance the power output of wrist-worn eccentric rotor energy harvesters when real human walking excitation is considered. This effect was predicted by the model and demonstrated experimentally. The experimental data for the population under consideration for a particular excitation agree well with the model predictions for the population for 2.5 mph and 3.5 mph walking speeds, although the model generally underpredicts device performance for the 5.5 mph treadmill belt speed.

Before concluding this chapter, some remarks on the practicality of spring implementation are warranted. The spring improves power output only when installed such that the restoring torque resists the effects of gravitational acceleration, and simulations predict that power output is reduced below that of the unsprung eccentric rotor if the opposite orientation is employed. This represents a major drawback of the sprung eccentric rotor in a consumer product, as the orientation in which the product is used has a major impact on device performance. Potential strategies to address this limitation include user or retailer device setup and education prior to product use (to ensure correct harvester orientation on the wrist), or left- and right-handed product versions that encourage use in the correct orientation; of course, these are admittedly clumsy remedies, and the simplicity of the orientation-independent unsprung rotational harvester makes it an attractive alternative to its sprung counterpart, in spite of its generally lower power output.

3.5 References

[1] M. A. Karami and D. J. Inman, “Equivalent damping and frequency change for linear and nonlinear hybrid vibrational energy harvesting systems,” *J. Sound Vib.*, vol. 330, no. 23, pp. 5583–5597, 2011.

[2] P. D. Mitcheson, T. C. Green, E. M. Yeatman, and A. S. Holmes, “Architectures for vibration-driven micropower generators,” *J. Microelectromechanic Syst.*, vol. 13, no. 3, pp. 429–440, 2004.

[3] J. Guckenheimer and P. Holmes, *Nonlinear Oscillations, Dynamical Systems, and Bifurcations of Vector Fields*, 5th ed. Springer-Verlag New York Inc., 1983.

[4] B. Hejrati, S. Chesebrough, K. B. Foreman, J. J. Abbott, and A. S. Merryweather, “Comprehensive quantitative investigation of arm swing during walking at various speed and surface slope conditions,” *Hum. Mov. Sci.*, vol. 49, pp. 104–115, 2016.

[5] A. Hreljac, “Effects of physical characteristics on the gait transition speed during human locomotion,” *Hum. Mov. Sci.*, vol. 14, no. 2, pp. 205–216, 1995.

CHAPTER 4

ON THE DYNAMICS OF WRIST-WORN ECCENTRIC ROTOR ENERGY HARVESTERS

This chapter concerns the steady state dynamics of eccentric rotor harvesters under the excitation of a forced pendulum, selected as a simplified representation of the swinging motion of the human arm during locomotion, to better understand their use for wrist-worn energy harvesting applications. A linearized model predicts the behavior of non-resonant eccentric rotor devices well and provides insight into the relationship between the rotor natural frequency and transducer-imposed electrical damping. Approximate analytical solutions are obtained via perturbation methods that show that the eccentric rotor shares many characteristics of a Duffing oscillator with softening spring nonlinearity. Finally, an interesting property of the eccentric rotor's dynamics – namely, invariance of power output to changes in forcing frequency and amplitude over certain ranges of design parameters – is exploited to propose a novel resonant eccentric rotor harvester with a wideband power output response.

4.1 Introduction

Eccentric rotors have maintained a position of particular interest in the literature as a choice of inertial mass architecture for wrist-worn vibration energy harvesting applications [1]–[7], and this harvester architecture even appears in consumer products designed to scavenge energy from the motion of the body [8], [9]. These asymmetric, rotational, inertial vibration energy harvesters exhibit several desirable properties for a wrist-worn application, including sensitivity to both rotational and translational motion [1], a lack of hard displacement limits, and a watch-like form factor.

In spite of its popularity as an alternative to more traditional, translational harvester architectures for body-worn applications, surprisingly little has been published on the complex dynamics that these devices exhibit. Although mathematical models have been proposed to describe these devices, their use has been limited primarily to the assistance of design by virtue of numerical investigation of the effects of dimensioned design parameters on power output. Much has been published on forced and parametrically excited pendula in the mathematics and dynamics literature, with [10]–[13] representing only a minute sample of such work, but, to the authors' knowledge, no such publications exist that study the nonlinear model of an eccentric rotor harvester, such as that derived in [14], for the purpose of better understanding the relationship between design parameters and power output.

Some authors have suggested [1], [2], [15], [16] that the dynamic magnification that resonance can provide is either infeasible or impossible to achieve for applications on the human body due to either the low-frequency, high-amplitude nature of human motion, device size constraints, or both. It is perhaps due to the prevalence of this belief that non-resonant designs dominate the eccentric rotor harvesters proposed in the literature; this work also serves as a point refutation for this assertion, as the dynamical analysis presented herein suggests that a wideband, resonant eccentric rotor harvester may indeed perform well in a wrist-worn application.

This work begins by a deriving a nondimensionalized unsprung eccentric rotor model, beginning with a dimensioned nonlinear model that has been derived and empirically validated elsewhere [14]. A dimensionless power output equation and the input excitation functions of interest are also derived. A linearized model is derived to obtain a closed-form, analytical power output equation, which is useful for understanding how design parameters impact device performance; this equation is contrasted with its well-known translational energy harvester counterpart and is followed by a brief demonstration of the linear model's validity for non-resonant eccentric rotor harvesters. The limitations of the linear model are then examined, followed by an analysis of the nonlinear dynamics using both numerical and approximate analytical methods. The nonlinear analysis shows that the eccentric rotor system shares many features in common with a Duffing oscillator with softening spring nonlinearity and that the primary resonance is a particularly attractive point around which to base a harvester design. The manuscript concludes with a proposal for a novel, resonant eccentric rotor harvester for wrist-worn application, which is compared with a non-resonant design via simulation.

4.2 System Model

A planar model that governs the dynamics of an eccentric rotor harvester has been derived and experimentally corroborated in [14] and is given by

$$\ddot{\phi} + \frac{b_e + b_m}{ml^2 + I_g}\dot{\phi} + \frac{ml}{ml^2 + I_g}a_y(t)\cos\phi \\ - \frac{ml}{ml^2 + I_g}a_x(t)\sin\phi + \frac{k}{ml^2 + I_g}\left(\phi - \frac{\pi}{2}\right) + \ddot{\theta}(t) = 0 \tag{4-1}$$

where ϕ is the displacement of the eccentric rotor relative to the harvester housing coordinate frame, b_e and b_m are the electrical and mechanical linear viscous damping coefficients, respectively, m is the mass of the rotor, l is the distance from the rotating center to the rotor's center of gravity, I_g is the inertia of the rotor about its own center of gravity, k is the torsional spring stiffness, $a_y(t)$ and $a_x(t)$ are the input linear accelerations of the harvester housing (which typically include gravitational acceleration) in the $\boldsymbol{y}$- and $\boldsymbol{x}$-directions, respectively, $\ddot{\theta}(t)$ is the input angular acceleration of the housing, and overdots represent differentiation with respect to time (Figure 4-1).

The parameters b_e, m, l, I_g, and k in (4-1) are treated as design variables, selected

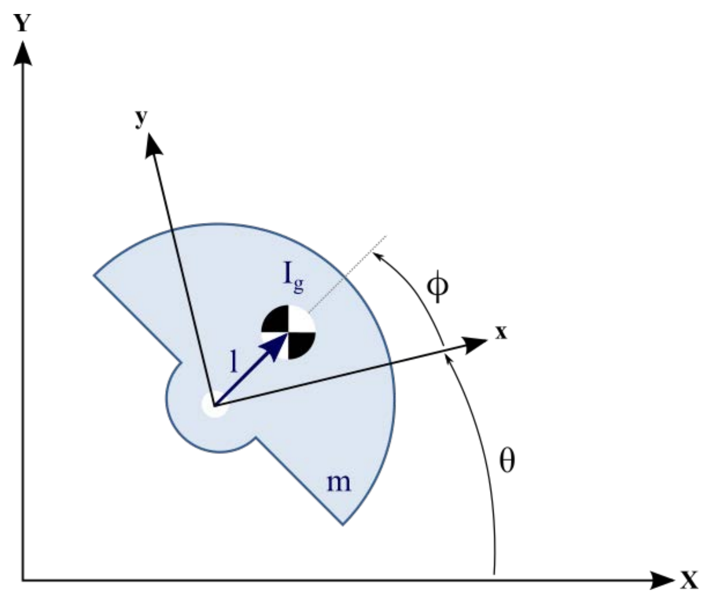

Figure 4-1 – Schematic of planar rotor model. Torsional spring not shown.

by the designer of the harvester. Although the designer may have some control over the degree of loss, determined by b_m, this parameter is not treated as a design variable and is instead given. Also note that the variables m, l, and I_g are not truly free parameters to be selected, as they are constrained by the choice of rotor geometry, which must be physically realizable for any practical implementation of a design.

Notice that (4-1) has been put in monic form and is therefore well-defined only when the total rotational inertia about the center of rotation $ml^2 + I_g \neq 0$. Furthermore, to make (4-1) physically meaningful, it is assumed that b_e, b_m, m, l, I_g, and k are nonnegative. As this paper is concerned with the dynamics of the eccentric rotor harvester without a torsional spring, only the case of the unsprung rotor ($k = 0$) will be considered hereafter.

By defining the effective length of the eccentric mass as $l_{eff} = \left(ml^2 + I_g\right)/(ml)$, and letting $k = 0$, (4-1) may be rewritten more compactly as

$$\ddot{\phi} + \frac{b_e + b_m}{ml^2 + I_g}\dot{\phi} + \frac{a_y(t)}{l_{eff}}\cos\phi - \frac{a_x(t)}{l_{eff}}\sin\phi + \ddot{\theta}(t) = 0 \qquad \text{(4-2)}$$

To ensure that l_{eff} is well-defined, assume $m, l > 0$. Finally, (4-2) can be represented in an alternative coordinate frame that will be the focus of the remainder of this paper (Figure 4-2). Let $\gamma = \phi + {}^{\pi}/_{2}$. Equation (4-2) becomes

$$\ddot{\gamma} + \frac{b_e + b_m}{ml^2 + I_g}\dot{\gamma} + \frac{a_x(t)}{l_{eff}}\cos\gamma + \frac{a_y(t)}{l_{eff}}\sin\gamma + \ddot{\theta}(t) = 0 \qquad \text{(4-3)}$$

Let $\dot{\gamma}_0(t)$ represent the time derivative of any solution to (4-3). The focus of this paper is (4-3) subject to periodic forcing and, particularly, the behavior of the time

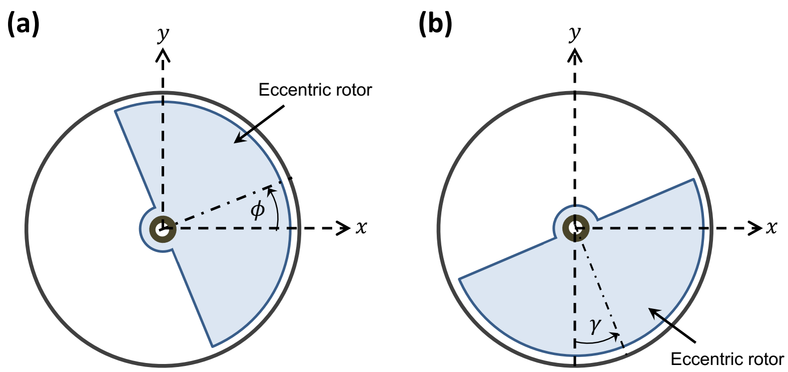

Figure 4-2 – Schematic of (a) the ϕ-coordinate frame used in (4-1) and (4-2), and (b) the γ-coordinate frame used in (4-3)

derivative of solutions after much time has passed; in other words, the steady state behavior. With this focus in mind, it is assumed that, after a long time, $\dot{\gamma}_0(t)$ converges to a periodic solution $\dot{\gamma}(t)$; that is

$$\lim_{\omega} \dot{\gamma}_0(t) = \dot{\gamma}(t) = \dot{\gamma}(t+T)$$

where $\lim_{\omega}$ is the ω-limit set and T is a period. Note that the assumption that steady state is achieved neglects the possibility of long-term, aperiodic or chaotic behavior. The power output of an eccentric rotor device modeled using (4-3) is found by computing the power dissipated by the "electrical damper," a linear viscous rotational damper with damping coefficient b_e. The average power dissipated by this damper over a period of $\dot{\gamma}$, and therefore the steady state power output, is

$$P = \frac{\mathrm{b_e}}{T}\int_0^T \dot{\gamma}^2 dt \qquad (4\text{-}4)$$

4.2.1 Swing Arm Kinematics

In this study, the arm motion of humans during walking is modeled using the kinematics of a driven pendulum, with the resultant excitation at the distal end of the pendulum hereafter referred to as *swing arm* excitation (Figure 4-3). Although this represents a major simplification in excitation for the purpose of analysis, actual human arm swing during locomotion shares several characteristics in common with the motion of a simple pendulum [17], [18] and therefore makes for an appropriate first-order approximation of the excitation of interest.

The tangential component of acceleration induced by the swing arm motion is given by:

$$a_t = \frac{d}{dt}\left(l_{arm}\dot{\theta}\right) = l_{arm}\ddot{\theta}$$

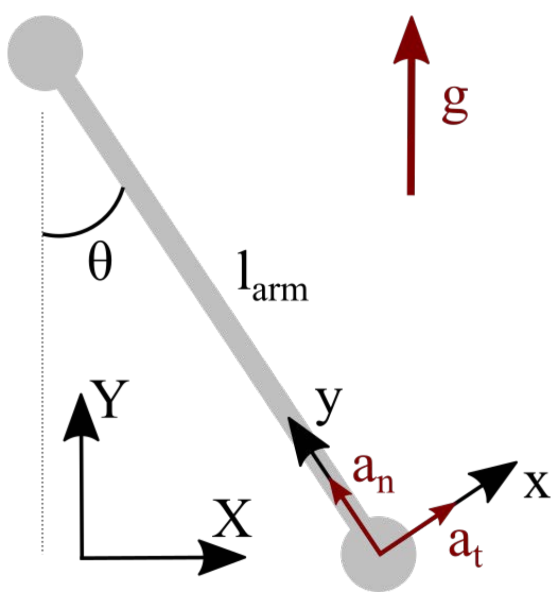

Figure 4-3 – Schematic of the swing arm. Coordinate frames are consistent with those of Figure 4-1.

where l_{arm} is the length of the swing arm, θ is the angular displacement of the swing arm, and overdots represent differentiation with respect to time. Similarly, the normal component of acceleration induced by the swing arm motion is given by:

$$a_n = \frac{\left(l_{arm}\dot{\theta}\right)^2}{l_{arm}} = l_{arm}\dot{\theta}^2$$

Rather than consider a downward gravitational force acting on the eccentric mass directly, instead consider gravity as an effective acceleration of the housing reference frame (the $\boldsymbol{xy}$-coordinate frame in Figure 4-3)

The swing arm excitation is derived from the kinematics of a harmonically-driven pendulum. Consider:

$$\ddot{\theta}(t) = -\omega^2\theta_{max}\sin\omega t \tag{4-5}$$

The total acceleration in the $\boldsymbol{x}$-direction is then

$$\begin{aligned} x_{total} &= g\sin\theta + l_{arm}\ddot{\theta} \\ &= g\sin(\theta_{max}\sin\omega t) + l_{arm}(-\omega^2\theta_{max}\sin\omega t) \end{aligned}$$

and the total acceleration in the $\boldsymbol{y}$-direction is

$$\begin{aligned} y_{total} &= g\cos\theta + l_{arm}\dot{\theta}^2 \\ &= g\cos(\theta_{max}\sin\omega t) + l_{arm}(\omega\theta_{max}\cos\omega t)^2 \end{aligned}$$

Note that it is assumed that $g, l_{arm}, \theta_{max}, \omega \geq 0$.

4.2.2 Approximation of Kinematic Functions

Assuming small angles for θ_{max} allows for considerable simplification of the expression for total acceleration in the $\boldsymbol{x}$-direction:

$$x_{total} \approx \theta_{max}(g - l_{arm}\omega^2)\sin\omega t$$

Similarly, the small-angle approximation can reduce the complexity of the expression for total acceleration in the $\boldsymbol{y}$-direction:

$$\begin{aligned} y_{total} &\approx g\left(1 - \frac{\theta_{max}^2 \sin^2\omega t}{2}\right) + \theta_{max}^2 l_{arm}\omega^2\cos^2\omega t \\ &\approx g\left(1 - \frac{\theta_{max}^2}{4}\right) + \frac{\theta_{max}^2 l_{arm}\omega^2}{2} + \frac{\theta_{max}^2}{2}\left(\frac{g}{2} + l_{arm}\omega^2\right)\cos 2\omega t \end{aligned}$$

Denoting the average over one swing arm period $2\pi/\omega$ as $\langle\cdot\rangle$, let

$$\bar{y} = g\left(1 - \frac{\theta_{max}^2}{4}\right) + \frac{\theta_{max}^2 l_{arm}\omega^2}{2} \approx \langle y_{total}\rangle$$

Finally, let

$$x = \theta_{max}(l_{arm}\omega^2 - g)$$

$$y = \theta_{max}^2\left(\frac{g}{2} + l_{arm}\omega^2\right)$$

Note that x and y (not to be confused with the $\boldsymbol{x}$- and $\boldsymbol{y}$-basis vectors for the housing coordinate frame) have dimension of acceleration. The approximate acceleration functions $a_x(t)$ and $a_y(t)$ for swing arm excitation may now be expressed compactly as

$$a_x(t) \approx -x \sin \omega t \tag{4-6}$$

$$a_y(t) \approx \bar{y} + y \cos 2\omega t \tag{4-7}$$

4.2.3 Kinematic Analysis

It is clear from the definition of the amplitude of the $\boldsymbol{x}$-acceleration, $x = \theta_{max}(l_{arm}\omega^2 - g)$, that the total $\boldsymbol{x}$-acceleration vanishes when

$$\omega = \sqrt{\frac{g}{l_{arm}}}$$

which is the (linearized) natural frequency, sometimes referred to as the *natural pendular frequency,* of the swing arm. At slow walking speeds, fewer muscle contractions occur at the shoulder to produce additional acceleration beyond that due to gravity alone, which means that the arm will tend to oscillate close to its natural pendular frequency [18]; this presents a major challenge in harvesting energy at the wrist during casual locomotion, since the true $\boldsymbol{x}$-accelerations at the wrist are expected to all but disappear when the arm oscillates near its natural frequency.

4.2.4 Nondimensionalization

Consider (4-3) subject to the swing arm excitation functions given by (4-5), (4-6), and (4-7):

$$\ddot{\gamma} + \frac{b_e + b_m}{ml^2 + I_g}\dot{\gamma} + \omega_0^2\left(1 + \frac{y}{\bar{y}}\right)\cos 2\omega t \sin\gamma - \omega_0^2 \frac{x}{\bar{y}} \sin\omega t \cos\gamma$$
$$= \omega^2 \theta_{max} \sin\omega t \tag{4-8}$$

where $\omega_0 = \sqrt{\bar{y}/l_{eff}}$ is taken to be the natural frequency of the rotor. To reduce the number of parameters under consideration to only those that are essential, (4-8) may be nondimensionalized by introducing the following normalized variables: time $\tau = \omega_0 t$, electrical damping $\beta_e = b_e/\left(2\omega_0\left(ml^2 + I_g\right)\right)$, mechanical damping $\beta_m = b_m/\left(2\omega_0\left(ml^2 + I_g\right)\right)$, frequency ratio $\Omega = \omega/\omega_0$, $\boldsymbol{y}$-acceleration amplitude $A_y = y/\bar{y}$, and $\boldsymbol{x}$-acceleration amplitude $A_x = x/\bar{y}$. Equation (4-8) may now be written as

$$\gamma'' + 2(\beta_e + \beta_m)\gamma' + \left(1 + A_y \cos 2\Omega\tau\right)\sin\gamma - A_x \sin\Omega\tau\cos\gamma$$
$$= \Omega^2 \theta_{max} \sin\Omega\tau \tag{4-9}$$

where the prime denotes differentiation with respect to dimensionless time τ.

It is desired to find a dimensionless analogue to the dimensioned power (4-4) that can be scaled back to the dimensioned power by virtue of variables independent of dimensionless design parameters. To derive such an expression, it is useful to first define one last dimensionless parameter, $\lambda = l/l_{eff}$. Notice that, given the nonnegativity constraint on m, l, and I_g, and since $\lambda = ml^2/\left(ml^2 + I_g\right)$, λ is bounded from above by unity. Given that $m, l > 0$, the parameter $\lambda = 1$ only when $I_g = 0$, which corresponds to a rotor geometry described by a point mass m at a distance l from the rotating center (i.e., the eccentric mass acts as a simple pendulum). When $0 < \lambda < 1$, the eccentric mass acts as a compound pendulum. As λ becomes small, the eccentric mass becomes less and less eccentric, losing all eccentricity when $\lambda = 0$, at which point $l = 0$ and l_{eff} is no longer well-defined. Consequentially, $\omega_0 = \sqrt{\bar{y}/l_{eff}}$ is also not well-defined, and the scale used to derive (4-9) breaks down. λ is, therefore, a geometric parameter describing the distribution of mass of the rotor, and lies on the interval $0 < \lambda \leq 1$.

Let the dimensionless upper bound on integration be $\tau_0 = \omega_0 T$. Beginning with (4-4)

$$
\begin{aligned}
P &= \frac{\mathrm{b_e}}{T}\int_0^T \dot{\gamma}^2 dt \\
&= \frac{2\omega_0^3\left(ml^2 + I_g\right)\beta_e}{\tau_0}\int_0^{\tau_0} \gamma'^2 d\tau \\
&= \frac{2\bar{y}\omega_0 ml\beta_e}{\tau_0}\int_0^{\tau_0} \gamma'^2 d\tau \\
&= \frac{2\bar{y}\omega_0 ml_{eff}\beta_e\lambda}{\tau_0}\int_0^{\tau_0} \gamma'^2 d\tau \\
&= \frac{2\bar{y}^2 m\beta_e\lambda}{\omega_0\tau_0}\int_0^{\tau_0} \gamma'^2 d\tau \\
&= \frac{\bar{y}^2 m}{\omega}\frac{2\beta_e\Omega\lambda}{\tau_0}\int_0^{\tau_0} \gamma'^2 d\tau
\end{aligned}
\tag{4-10}
$$

Equation (4-10) may be divided into dimensioned and dimensionless components; analysis is greatly aided by defining a *dimensionless power* Π:

$$
\Pi = \frac{2\beta_e\Omega\lambda}{\tau_0}\int_0^{\tau_0} \gamma'^2 d\tau \tag{4-11}
$$

such that the dimensioned power $P = \bar{y}^2 m\Pi/\omega$; stated another way, the dimensioned power P is normalized by $\bar{y}^2 m/\omega$ to give Π, as in [19].

Thus, by (4-11), given the input excitation parameters (A_y, A_x, θ_{max}) and the mechanical damping β_m, the dimensionless power, $\Pi = \Pi(\beta_e, \Omega, \lambda)$, is determined over a span of dimensionless time τ_0 by the three dimensionless design parameters β_e, Ω, and λ alone. The dimensionless power is scaled to the dimensioned power P by $\bar{y}^2 m/\omega$, which is independent of the dimensionless design variables for a fixed excitation. Thus, the problem of determining the optimal m, l, I_g, and b_e given an input excitation and degree of mechanical damping reduces to determining the β_e, Ω, and λ that maximize Π, with m acting as a scaling factor for the dimensioned power output P.

4.2.5 Excitations

Several fixed excitations, treated as representative of arm swing exhibited over a range of walking speeds [18], are considered in this work (Table 4-1). With $l_{arm} = 0.5\ m$ (an approximation of the mean length from the acromion (shoulder) to the ulnar styloid process (wrist) in humans [17]), the excitations are fully defined when the swing arm excitation parameters A_y and A_x are computed using l_{arm}, ω, and θ_{max} according to their definitions given in the previous subsection.

4.3 Linearized System

An analytical solution to (4-9) is desired in order to better understand the relationship between the design variables, input excitation, and power; however, due to the nonlinearity and periodic coefficients present in (4-9), an analytical solution is difficult, if

Table 4-1 – List of excitations and associated parameter values used in this work

Excitation	$\boldsymbol{\theta_{max}}$ **[deg]**	$\boldsymbol{\omega}$ **[Hz]**	$\boldsymbol{\theta_{max}}$ **[rad]**	$\boldsymbol{A_x}$	$\boldsymbol{A_y}$
EX1	12.5	0.8	0.2182	0.0616	0.0418
EX2	12.5	1	0.2182	0.2131	0.0577
EX3	12.5	1.25	0.2182	0.4401	0.0816
EX4	25	0.8	0.4363	0.1168	0.1583
EX5	25	1	0.4363	0.3861	0.2090
EX6	25	1.25	0.4363	0.7474	0.2771

not impossible, to obtain. Instead, linearization may provide solutions valid over a particular regime of operation. Linearization of (4-9) about $\gamma = 0$ yields the following linear, inhomogeneous differential equation:

$$\gamma'' + 2(\beta_e + \beta_m)\gamma' + \left(1 + A_y \cos 2\Omega\tau\right)\gamma = (A_x + \Omega^2\theta_{max}) \sin \Omega\tau \qquad (4\text{-}12)$$

Equation (4-12) is a forced, damped Mathieu differential equation, for which, once again, an analytical solution is difficult, if not impossible, to obtain. Since an analytical solution is desired, consider instead the case where A_y is negligibly small; this assumption is warranted for most of the excitations listed in Table 4-1. Under this assumption, (4-12) becomes

$$\gamma'' + 2(\beta_e + \beta_m)\gamma' + \gamma = (A_x + \Omega^2\theta_{max}) \sin \Omega\tau \qquad (4\text{-}13)$$

Equation (4-13) is a linear, inhomogeneous differential equation with constant coefficients that is easily solvable. As the focus of this work is on the steady state behavior of the eccentric rotor, only the particular solution to (4-13) is required for analysis. To this end, the method of undetermined coefficients is employed using the ansatz $\gamma(\tau) = A\cos\Omega\tau + B\sin\Omega\tau$ and solving for A and B. Substitution of γ' in (4-11) with $\tau_0 =$

$\omega_0 T = 2\pi/\Omega$ (one swing arm cycle) gives the dimensionless power output

$$\Pi = \frac{\beta_e \Omega^2 \lambda}{\pi} \int_0^{2\pi/\Omega} \gamma'^2 d\tau = \frac{\beta_e \Omega^3 \lambda (A_x + \Omega^2 \theta_{max})^2}{(\Omega^2 - 1)^2 + [2(\beta_e + \beta_m)\Omega]^2} \tag{4-14}$$

There are several similarities and differences of note between (4-14) and the well-known power output equation for translational vibration energy harvesters [20], [21], provided below for the convenience of the reader

$$P_{translational} = \frac{A^2 m}{\omega} \frac{\zeta_e r^3}{(r^2 - 1)^2 + [2(\zeta_e + \zeta_m) r]^2} \tag{4-15}$$

where A is the input acceleration amplitude, ω is the input frequency, m is the seismic mass, ζ_e and ζ_m are the electrical and mechanical damping ratios, respectively, and r is the ratio of the input frequency to the harvester natural frequency. The leftmost fraction in (4-15) is similar to the dimensioned factor $\bar{y}^2 m/\omega$ used to scale (4-14), the eccentric rotor dimensionless power, back to the dimensioned power. The rightmost fraction in (4-15) is dimensionless, very similar in form to (4-14), and yields several of the same results. For example, (4-14) exhibits a resonance peak at $\Omega \approx 1$ for systems with sufficiently low damping. Additionally, letting $\Omega = 1$ in (4-14) and finding the stationary point on $d\Pi/d\beta_e$ gives the optimal electrical damping ratio of $\beta_e = \beta_m$, similar to the result found in [19], [22].

However, there are also major differences between the power output functions in the eccentric rotor and the translational case. First, there is an additional variable in the eccentric rotor case, λ, which is required since a particular rotor natural frequency can be achieved in an infinite number of geometric configurations for a given rotor mass m; this is unlike the translational case, where a particular natural frequency is uniquely determined by the choice of linear spring stiffness once the seismic mass has been fixed. Since λ is entirely independent of the other dimensionless parameters on the interval $0 < \lambda \leq 1$, it is clear from the form of (4-14) that the optimal λ is $\lambda^{\star} = 1$ (Figure 4-4).

Secondly, the topology of the power function in the eccentric rotor case and that of the translational case are different. Assuming a sufficiently low level of damping, the eccentric rotor case described by (4-14) is characterized by a sharp resonance peak, but power will also grow without bound as $\beta_e, \Omega \to \infty$, unlike in the analogous translational case; this is due to the fact that a finite amount of mass may be distributed so as to produce any arbitrary amount of inertia about the center of rotation (Figure 4-5). Without constraining the geometry to the practical bounds imposed by a wrist-worn energy harvester, such solutions cannot be avoided; note that a volumetric constraint on the geometry is insufficient to preclude such solutions. Note that all excitations in Table 4-1

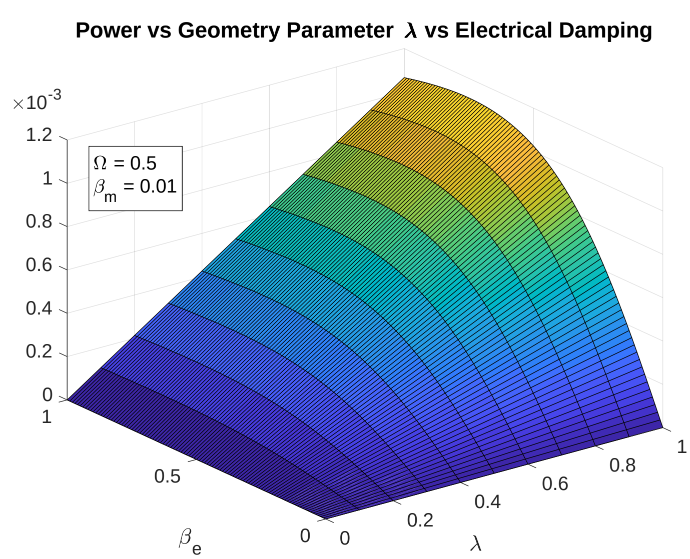

Figure 4-4 – Dimensionless power as a function of the geometric parameter λ and electrical damping ratio for excitation EX1.

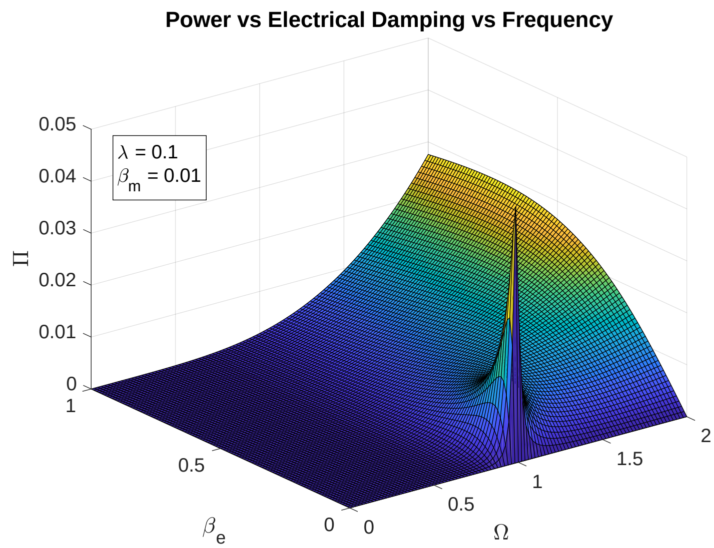

Figure 4-5 – Dimensionless power as a function of electrical damping ratio and frequency ratio for excitation EX1. Note the sharp resonance peak at $\Omega \approx 1$, and continued increase in dimensionless power for large β_e and Ω.

produced a qualitatively similar plot for sufficiently low levels of damping.

Finally, it should be noted that the interpretation of the frequency ratio in the rotational case can be substantially different from the translational case. Since the input frequency ω cannot change without a corresponding change in the linear accelerations (and thus a change in, for example, A_x), disparate values of Ω for a given excitation, such as those plotted in Figure 4-5, are achieved by changing the harvester natural frequency, ω_0, since $\Omega = \omega/\omega_0$.

Figure 4-5 illuminates an interesting feature of the design of eccentric rotor harvesters: as the design moves away from $\Omega \approx 1$ (or, phrased differently, as the device becomes more *non-resonant*) the electrical damping required for optimal power output increases. Non-resonant harvesters, therefore, require a relatively high degree of electrical damping for acceptable performance.

4.3.1 A Fixed Geometry

The description of a rotor in terms of mass m, eccentric length l, and inertia about its own center of gravity I_g is very general; the rotor could be composed of many complex solid bodies with varying density or a collection infinitesimally small particles of mass; the rotor may even be radially symmetric under such a description and therefore not eccentric at all – although the use of (4-2) and its dimensionless counterpart (4-9) do prohibit this limiting case. Partially as a consequence of this generality, the power result described by (4-14) is difficult to interpret with regard to practical design guidance. For example: since large Ω can result in high power output, would it be advisable to modify the geometry of a rotor in order to reduce the natural frequency of oscillation (increase Ω) if this comes at the cost of reducing λ? A question such at this may be answered by constraining the geometry under consideration, which imposes relationships between the design variables in (4-14), such as Ω and λ.

Consider the choice of a homogeneous cylindrical sector of material density ρ with angle $\alpha = 2\psi$, radius r, and height h for the geometry of an eccentric rotor. This choice of geometry permits the expression of some design variables in (4-14) in terms of ψ and r:

$$m = \rho h \psi r^2 \qquad \lambda = \frac{8\sin^2\psi}{9\psi^2}$$

Additionally, let the total device volume $V = \pi r^2 h$; this is the volume swept by the cylindrical sector as the rotor coordinate γ moves through all points on its configuration manifold. Using the result from linearization (4-14), the power per unit volume for an eccentric rotor with cylindrical sector geometry is

$$\frac{P}{V} = \frac{\bar{y}^2 m}{\omega V}\Pi = \frac{\bar{y}^2\rho}{\omega}\frac{8\beta_e\Omega^3\sin^2\psi\,(A_x + \Omega^2\theta_{max})^2}{9\pi\psi[(\Omega^2 - 1)^2 + (2(\beta_e + \beta_m)\Omega)^2]} \tag{4-16}$$

For a given material density ρ and input excitation, maximizing $m\lambda/V$ amounts to maximizing $\sin^2\psi/\psi$, which occurs at a sector angle of $\alpha = 2\psi \approx 134°$. A plot of power density vs. frequency vs. electrical damping ratio for a given excitation and mechanical damping ratio then shares the topology of (4-14) for a given value of λ, as in Figure 4-5. Therefore, constraining the geometry of an eccentric rotor device does not appear to obviate infinite power density solutions. If the sector angle is fixed to maximize $m\lambda/V$, then the only means by which the frequency may change for a given excitation while preserving the volume is by modifying the thickness of the rotor, which consequentially changes the rotor radius. To maximize power density, one then either chooses a rotor thickness and electrical damping ratio that allows for resonance with the input excitation, or one reduces the thickness indefinitely while simultaneously increasing the electrical damping so that power grows without bound as $\beta_e, \Omega \to \infty$; this corresponds to a device of infinitesimal thickness and infinite radius.

It is possible to express the frequency in terms of the geometric design variables as well so that the device radius may be constrained:

$$\Omega = \omega\sqrt{\frac{3\psi r}{4\bar{y}\sin\psi}}$$

Substitution of this result into (4-16) yields a very complex expression for power density that warrants a brief numerical investigation. Consider a tungsten ($\rho = 19000\ kg\ m^{-3}$) cylindrical sector eccentric rotor device with a volume of $V = 1cm^3$ and thickness 2 mm, requiring a radius $r \approx 12.6\ mm$. Using a swing arm excitation described by a swing arm length of $l_{arm} = 0.5\ m$, swing frequency of $\omega = 0.91\ Hz$, and a swing amplitude of $\theta_{max} = 25°$, with a device mechanical damping ratio of $\beta_m = 0.0012$, a plot of power vs. sector angle vs. damping ratio may be generated (Figure 4-6).

The power density surface presented in Figure 4-6 now only contains two peaks; the first, larger peak corresponds to resonance with the swing arm excitation. In order to achieve resonance, the rotor requires a very large sector angle. The second peak occurs at a sector angle of $\alpha \approx 3.42\ rad \approx 196°$ and electrical damping ratio $\beta_e \approx 2.08$. This corresponds to a non-resonant design, and the maximizer agrees with optimization results for the nonlinear system (4-1) presented in [14] very closely.

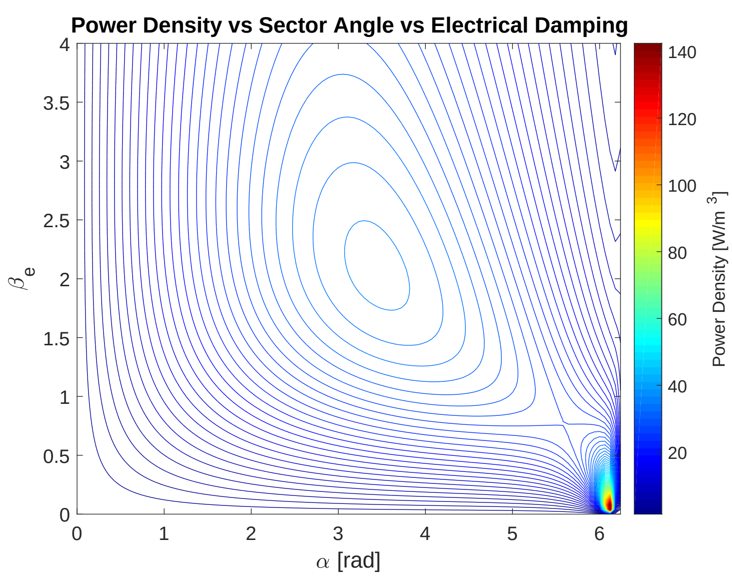

Figure 4-6 – Contour plot of power density vs. rotor sector angle and electrical damping ratio under a particular swing arm excitation

4.4 Nonlinear Dynamical Analysis

To observe the correspondence between the power output of the nonlinear system and its linearization, consider a plot of dimensionless power Π vs. Ω for a fixed amount of damping ($\beta_e = 0.02,\ \beta_m = 0$) and fixed $\lambda = 1$ in which the linearized system power output (4-14) is evaluated and the nonlinear system (4-9) is numerically solved for use in (4-11) over a range of Ω values. The result, using EX1 as the input excitation, is shown in Figure 4-7.

In spite of the mild excitation, it is clear from Figure 4-7 that the linearization fails to predict the sharp onset of the primary resonance peak for the nonlinear system at $\Omega \approx 0.8$, and consequently overpredicts the power output at the linear resonance of $\Omega \approx 1$. The linearization does not capture the leftward bending of the nonlinear primary resonance at all. However, it appears that the linearized result agrees closely with the nonlinear system

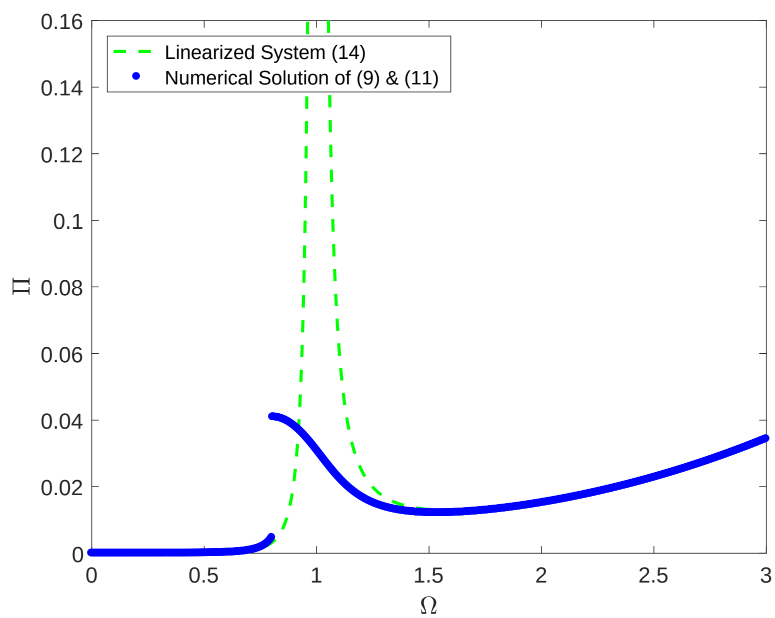

Figure 4-7 – Numerical vs. analytical (linearization) results for power vs. frequency ratio using EX1 input as long as Ω is far from the primary resonance peak. Consider a similar plot to Figure 4-7, but using the much more vigorous EX5 as the excitation input, shown in Figure 4-8.

As seen in Figure 4-8, the predictive power of the linearization is much worse for the higher-energy EX5 excitation, which is to be expected due to the small angle approximation used to derive (4-14), and additional nonlinear behavior is evident. A very wide, high-power peak now appears near $\Omega \approx 2.5$; several scattered, higher-power points also lie above this peak that are not shown in Figure 4-8 in order to improve the scale of the plot. Additionally, a sharp peak now clearly appears at $\Omega \approx 1/3$, although it should be noted that this peak is present for all excitations in Table 4-1 – albeit at much smaller magnitudes under light excitation – which is why this peak cannot be seen with the scale used in Figure 4-7. These additional peaks are referred to as *secondary resonances*. Additional nonlinear behavior can also be observed in Figure 4-8 (for example, near

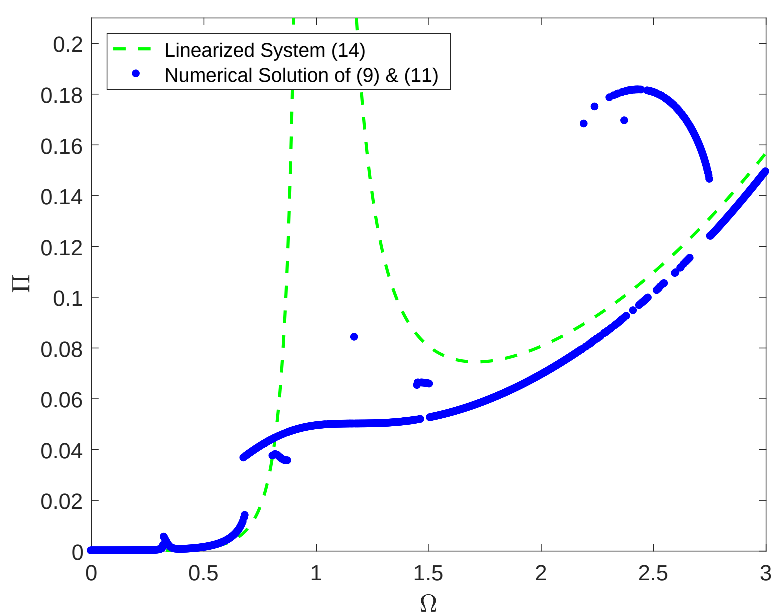

Figure 4-8 – Numerical vs. analytical (linearization) results for power vs. frequency ratio using EX5 input

$\Omega \approx 1.5$) but are much less consistent between excitations.

In order to develop a theory to explain the nonlinear behavior exhibited by the eccentric rotor system, approximate solutions are sought using perturbation methods. Note that all simulations carried out for the remainder of this section will assume $\beta_e = 0.02$, $\beta_m = 0$, and $\lambda = 1$.

4.4.1 System Approximation

Consider the following approximation to (4-9):

$$\begin{aligned} \gamma'' + 2(\beta_e + \beta_m)\gamma' + \left(1 + A_y \cos 2\Omega\tau\right)\left(\gamma - \frac{1}{6}\gamma^3\right) \\ - A_x \sin \Omega\tau \left(1 - \frac{1}{2}\gamma^2\right) = \Omega^2\theta_{max} \sin \Omega\tau \end{aligned} \tag{4-17}$$

Equation (4-17) is derived by taking the Taylor series of the trigonometric functions in (4-9) about $\gamma = 0$ (the Maclaurin series) and retaining the first two nonzero terms in the series.

The approximate system (4-17) will be used to study (4-9) by employing perturbation methods. Equation (4-17) may be rewritten as

$$\begin{aligned} \gamma'' + \gamma + \epsilon\left[2(\bar{\beta}_e + \bar{\beta}_m)\gamma' + \bar{A}_y \cos 2\Omega\tau\, \gamma + \frac{1}{2}\bar{A}_x \sin \Omega\tau\, \gamma^2 - \gamma^3\right] \\ + O(\epsilon^2) = F \sin \Omega\tau \end{aligned} \tag{4-18}$$

where ϵ is a small, but finite, dimensionless quantity that indicates the degree of the perturbation, and the substitutions $\beta_e = \epsilon\bar{\beta}_e$, $\beta_m = \epsilon\bar{\beta}_m$, $A_y = \epsilon\bar{A}_y$, $A_x = \epsilon\bar{A}_x$ are used to track parameters that are considered small, and $F = A_x + \Omega^2\theta_{max}$. Noting that the term

$O(\epsilon^2) = -\epsilon^2 \bar{A}_y \cos 2\Omega\tau\, \gamma^3$, it is clear that (4-17) is recovered from (4-18) when $\epsilon = 1/6$, which will be considered small enough for satisfactory results, similar to [23, pp. 133-134].

One may be concerned that the forcing amplitude F, which is not treated as small, contains A_x, which is treated as small. However, consider the excitations of Table 4-1; for some of the excitations, such as EX1, A_x is certainly small. For other excitations, such as EX3, EX5, or EX6, A_x is arguably a large term; for this reason, it may perhaps best be considered a *borderline case*. On the other hand, $A_x/2$, which appears in a different role in a parametric forcing term in (4-17), is a much clearer case of a small term. Additionally, when Ω is small, the $\Omega^2\theta_{max}$ term in F is very small, which means A_x will dominate the forcing amplitude; if this is ignored, the accuracy of the unperturbed solution will suffer greatly since it is already clear that (4-13) accurately captures much of the dynamics for small Ω. For this reason, the somewhat unorthodox assumption that A_x is large but $A_x/2$ is not will be used in the analysis whenever strong forcing is considered.

A uniform approximate solution to (4-18) is sought in the form

$$\gamma(\tau; \epsilon) = \gamma_0(T_0, T_1, T_2, \dots) + \epsilon\gamma_1(T_0, T_1, T_2, \dots) + \cdots \tag{4-19}$$

where one writes $\gamma = \gamma(\tau; \epsilon)$, with the parameter ϵ separated by a semicolon, since γ is a function of both the independent variable τ and parameter ϵ. When $\epsilon = 0$, (4-18) becomes linear and its solution is denoted γ_0. Terms in the series in (4-19) of $O(\epsilon)$ and higher are corrections to the terms that come before, called the *correction series*, with the goal of additional terms yielding an asymptotic approximation to the solution of (4-18). When one retains a single term in the correction series – that is, terns up to $O(\epsilon)$ – then (4-19) is called a *first-order expansion*. Because functional dependence of γ on τ and ϵ is not disjoint – the solution approximation is dependent on the combination of $\epsilon\tau$ terms as well as on individual τ and ϵ – the solution may be written as $\gamma(\tau;\epsilon) = \hat{\gamma}(\tau, \epsilon\tau, \epsilon^2\tau, \dots; \epsilon) = \hat{\gamma}(T_0, T_1, T_2, \dots; \epsilon)$ with $T_0 = \tau$, $T_1 = \epsilon\tau$, $T_2 = \epsilon^2\tau$, etc., representing different time scales, since ϵ is a small parameter. First-order expansions will be the focus of this section, and such expansions may be obtained without actually having to solve for γ_1; only secular terms in the expression for γ_1 need be considered, which determine the dependence of the γ_0 on T_1 [24, pp. 122-126]. Thus, solutions in this section will be in the form

$$\gamma(\tau;\epsilon) = \gamma_0(T_0, T_1) + \epsilon\gamma_1(T_0, T_1) + \cdots \tag{4-20}$$

where only the γ_0 term, herein denoted simply as γ, needs to be found, and $O(\epsilon)$ terms are neglected. The methods of variation of parameters and averaging will be used to approximate solutions to (4-17).

A final remark before the analysis: applying the method of averaging to systems with both quadratic and cubic nonlinearities can sometimes give erroneous results due to interactions between approximation orders; such an interaction was shown to occur between first- and second-order approximations when a third-order approximation was sought for a system with quadratic and cubic nonlinearities in [24, pp. 168-169]. Although (4-18) differs significantly from this example and only a first-order approximation is desired, the analysis will be validated by comparing predictions made by the perturbation solutions of (4-18) to those made using numerical integration of (4-9).

4.4.2 Secondary Resonances

To apply the method of averaging to the secondary resonances, the method of variation of parameters is first applied. The solution of (4-18) with $\epsilon = 0$ is

$$\gamma = a\cos(\tau + b) + 2\Lambda \sin \Omega\tau \tag{4-21}$$

where the *free-oscillation* term is $a\cos(\tau + b)$ with a and b as constants, which are sometimes referred to as *parameters*, and $\Lambda = (A_x + \Omega^2\theta_{max})/[2(1-\Omega^2)]$. Notice that (4-21) contains a term with a small divisor that becomes very large as $\Omega \to 1$; the existence of this term is why the primary and secondary resonances are treated separately in this analysis.

When $\epsilon \neq 0$, it is assumed that the solution is still given by (4-21), but with slowly time-varying parameters $a(T_1)$ and $b(T_1)$. The solution (4-21) may be viewed as a transformation from $\gamma(\tau)$ to $a(T_1)$ and $b(T_1)$, wherein three unknowns are to be found using two equations, (4-18) and (4-21). As a consequence, there is freedom in choosing a third equation that imposes a condition on the unknowns. A convenient choice is taking the (dimensionless) time derivative of (4-21) while treating a and b as constants:

$$\gamma' = -a\sin(\tau + b) + 2\Lambda\Omega \cos \Omega\tau \tag{4-22}$$

However, when $\epsilon \neq 0$, the solution is still of the form (4-21), subject to the constraint (4-22), but with $a = a(\tau)$ and $b = b(\tau)$. Differentiation of (4-21) in light of this gives

$$\gamma' = -a\sin(\tau + b) + a'\cos(\tau + b) - ab'\sin(\tau + b) + 2\Lambda\Omega \cos \Omega\tau \tag{4-23}$$

Equation (4-22) with (4-23) implies

$$a' \cos(\tau + b) - ab' \sin(\tau + b) = 0 \tag{4-24}$$

Differentiating (4-22) once more yields

$$\gamma'' = -a \cos(\tau + b) - a' \sin(\tau + b) - ab' \cos(\tau + b) - 2\Lambda\Omega^2 \sin \Omega\tau \tag{4-25}$$

Substitution of (4-21), (4-22), and (4-25) into (4-18) gives

$$\begin{aligned}
&-a \cos(\tau + b) - a' \sin(\tau + b) - ab' \cos(\tau + b) - 2\Lambda\Omega^2 \sin \Omega\tau \\
&\quad + a \cos(\tau + b) + 2\Lambda \sin \Omega\tau \\
&\quad + \epsilon \Big[2\big(\bar{\beta}_e + \bar{\beta}_m\big)(-a \sin(\tau + b) + 2\Lambda\Omega \cos \Omega\tau) \\
&\quad + \bar{A}_y \cos 2\Omega\tau \,(a \cos(\tau + b) + 2\Lambda \sin \Omega\tau) \\
&\quad + \frac{1}{2} \bar{A}_x \sin \Omega\tau \,(a \cos(\tau + b) + 2\Lambda \sin \Omega\tau)^2 \\
&\quad - (a \cos(\tau + b) + 2\Lambda \sin \Omega\tau)^3 - \bar{A}_x \sin \Omega\tau \Big] \\
&\quad = \Omega^2 \theta_{max} \sin \Omega\tau
\end{aligned} \tag{4-26}$$

where the interest in a first-order expansion allows for the dropping of the $O(\epsilon^2)$; this is made more plain from substitution of (4-20) into (4-18) with retention of terms up to $O(\epsilon)$, although such a procedure requires more algebra. As $\Lambda = (A_x + \Omega^2\theta_{max})/[2(1 - \Omega^2)]$, (4-26) reduces to

$$
\begin{aligned}
&a' \sin(\tau + b) + ab' \cos(\tau + b) \\
&= \epsilon \Big[2(\bar{\beta}_e + \bar{\beta}_m)(-a \sin(\tau + b) + 2\Lambda\Omega \cos \Omega\tau) \\
&+ \bar{A}_y \cos 2\Omega\tau \, (a \cos(\tau + b) + 2\Lambda \sin \Omega\tau) \\
&+ \frac{1}{2} \bar{A}_x \sin \Omega\tau \, (a \cos(\tau + b) + 2\Lambda \sin \Omega\tau)^2 \\
&- (a \cos(\tau + b) + 2\Lambda \sin \Omega\tau)^3 - \bar{A}_x \sin \Omega\tau \Big]
\end{aligned}
\tag{4-27}
$$

Multiply (4-24) by $\cos(\tau + b)$ and (4-27) by $\sin(\tau + b)$ and add the result to obtain

$$
\begin{aligned}
a' = \epsilon \sin(\tau + b) \Big[&2(\bar{\beta}_e + \bar{\beta}_m)(-a \sin(\tau + b) + 2\Lambda\Omega \cos \Omega\tau) \\
&+ \bar{A}_y \cos 2\Omega\tau \, (a \cos(\tau + b) + 2\Lambda \sin \Omega\tau) \\
&+ \frac{1}{2} \bar{A}_x \sin \Omega\tau \, (a \cos(\tau + b) + 2\Lambda \sin \Omega\tau)^2 \\
&- (a \cos(\tau + b) + 2\Lambda \sin \Omega\tau)^3 - \bar{A}_x \sin \Omega\tau \Big]
\end{aligned}
\tag{4-28}
$$

which defines the dynamics of the parameter a. The differential equation for b may be obtained similarly by multiplying (4-24) by $\sin(\tau + b)$ and (4-27) by $\cos(\tau + b)$ and adding the result to obtain

$$
\begin{aligned}
ab' = \epsilon \cos(\tau + b) \Big[& 2(\bar{\beta}_e + \bar{\beta}_m)(-a \sin(\tau + b) + 2\Lambda\Omega \cos \Omega\tau) \\
& + \bar{A}_y \cos 2\Omega\tau \, (a \cos(\tau + b) + 2\Lambda \sin \Omega\tau) \\
& + \frac{1}{2} \bar{A}_x \sin \Omega\tau \, (a \cos(\tau + b) + 2\Lambda \sin \Omega\tau)^2 \\
& - (a \cos(\tau + b) + 2\Lambda \sin \Omega\tau)^3 - \bar{A}_x \sin \Omega\tau \Big]
\end{aligned} \tag{4-29}
$$

Expanding (4-28) and (4-29) and grouping by the argument of the trigonometric functions gives

$$
\begin{aligned}
\frac{\partial a}{\partial T_1} = & -(\bar{\beta}_e + \bar{\beta}_m)a + \left(\frac{\bar{A}_x a^2}{16} - \frac{3\Lambda a^2}{4} \right) \cos[(3 - \Omega)\tau + 3b] \\
& + \left(\Lambda^3 - \frac{\bar{A}_x \Lambda^2}{4} + \frac{\bar{A}_y \Lambda}{2} \right) \cos[(1 - 3\Omega)\tau + b] + o.t.
\end{aligned}
$$

$$
\begin{aligned}
a \frac{\partial b}{\partial T_1} = & -3\Lambda^2 a + \frac{\bar{A}_x \Lambda a}{2} - \frac{3a^3}{8} \\
& + \left(-\frac{\bar{A}_x a^2}{16} + \frac{3\Lambda a^2}{4} \right) \sin[(3 - \Omega)\tau + 3b] \\
& + \left(-\Lambda^3 + \frac{\bar{A}_x \Lambda^2}{4} - \frac{\bar{A}_y \Lambda}{2} \right) \sin[(1 - 3\Omega)\tau + b] \\
& + \left(3\Lambda^2 a - \frac{\bar{A}_x \Lambda a}{2} + \frac{\bar{A}_y a}{2} \right) \cos 2\Omega\tau + o.t.
\end{aligned} \tag{4-30}
$$

where the substitution $\partial/\partial T_0 = \epsilon \partial/\partial T_1$ allows for elimination of ϵ and $o.t.$ refers to other terms that are immaterial with regard to the method of averaging near the secondary resonances, such as $\sin[(1 + 3\Omega)\tau + b]$ or $\cos[(3 + \Omega)\tau + b]$, as these fast varying terms average to zero for the secondary resonances near $\Omega \approx 3$ and $\Omega \approx 1/3$. Special consideration is required at $\Omega \approx 0$.

The terms in (4-30) are examined to demarcate frequencies of interest for the analysis.

Case 1: $\boldsymbol{\Omega \approx 3}$

In this case, the slowly-varying terms in (4-30) are $\cos[(3-\Omega)\tau + 3b]$ and $\sin[(3-\Omega)\tau + 3b]$. Thus, the solution parameters are governed by

$$\frac{\partial a}{\partial T_1} = -(\bar{\beta}_e + \bar{\beta}_m)a + \left(\frac{\bar{A}_x a^2}{16} - \frac{3\Lambda a^2}{4}\right)\cos[(3-\Omega)\tau + 3b]$$

$$a\frac{\partial b}{\partial T_1} = -3\Lambda^2 a + \frac{\bar{A}_x \Lambda a}{2} - \frac{3a^3}{8} \tag{4-31}$$

$$+\left(-\frac{\bar{A}_x a^2}{16} + \frac{3\Lambda a^2}{4}\right)\sin[(3-\Omega)\tau + 3b]$$

Substitute $\Omega = 3 + \epsilon\sigma$, where σ is referred to as a *detuning parameter* that is used to express the propinquity of Ω to 3, into (4-31) to give

$$\frac{\partial a}{\partial T_1} = -(\bar{\beta}_e + \bar{\beta}_m)a + \left(\frac{\bar{A}_x a^2}{16} - \frac{3\Lambda a^2}{4}\right)\cos[T_1\sigma - 3b]$$

$$a\frac{\partial b}{\partial T_1} = -3\Lambda^2 a + \frac{\bar{A}_x \Lambda a}{2} - \frac{3a^3}{8} + \left(\frac{\bar{A}_x a^2}{16} - \frac{3\Lambda a^2}{4}\right)\sin[T_1\sigma - 3b] \tag{4-32}$$

To make (4-32) autonomous, introduce a new independent variable

$$d = T_1\sigma - 3b \tag{4-33}$$

Hence

$$\frac{\partial d}{\partial T_1} = \sigma - 3\frac{\partial b}{\partial T_1} \tag{4-34}$$

Substituting (4-33) and (4-34) into (4-32) and simplifying yields

$$\begin{aligned} \frac{\partial a}{\partial T_1} &= -(\bar{\beta}_e + \bar{\beta}_m)a + a^2\left(\frac{\bar{A}_x}{16} - \frac{3\Lambda}{4}\right)\cos d \\ a\frac{\partial d}{\partial T_1} &= \sigma a + 9\Lambda^2 a - \frac{3\bar{A}_x\Lambda a}{2} + \frac{9a^3}{8} - 3a^2\left(\frac{\bar{A}_x}{16} - \frac{3\Lambda}{4}\right)\sin d \end{aligned} \tag{4-35}$$

which are now autonomous. It may appear that not much progress has been made; the nonlinear system (4-17) has been replaced by another nonlinear system (4-35). However, the parameters in (4-35) approach stationary values with increasing T_1, in which case the free-oscillation term in (4-21) achieves a periodic steady state with fixed amplitude. Letting $\partial a/\partial T_1 = \partial d/\partial T_1 = 0$ and, with some manipulation, d may be eliminated entirely, leaving

$$\begin{aligned} 81a^4 + 64\left[\frac{81\Lambda^2}{4} - \frac{27\bar{A}_x\Lambda}{8} + \frac{9\sigma}{4} - \frac{5}{2}(\bar{A}_x - 12\Lambda)^2\right]a^2 \\ + 16(18\Lambda^2 - 3\bar{A}_x\Lambda + 2\sigma)^2 + 64(\bar{\beta}_e + \bar{\beta}_e)^2 = 0 \end{aligned} \tag{4-36}$$

which is quadratic in a^2 and easily solved. Equation (4-36) is often referred to as a *frequency response equation*, and it relates the amplitude of the free-oscillation term to the frequency σ. For solutions satisfying $a^2 \in \mathbb{R}$, the discriminant of the solution satisfying (4-36) must be positive.

Note that (4-36) was derived by neglecting the $a = 0$ solution, which is a solution of particular interest since this implies that the free-oscillation term in (4-21) vanishes. The stability of this solution will be discussed later.

Substitution of $b = T_1\sigma/3 - d/3$ from (4-33), along with $\Omega = 3 + \epsilon\sigma$ and $T_1 = \epsilon\tau$, into (4-20) gives the solution

$$\gamma = a\cos\left(\frac{1}{3}\Omega\tau - \frac{1}{3}d\right) + 2\Lambda\sin\Omega\tau + O(\epsilon) \tag{4-37}$$

up to $O(\epsilon)$ with (dimensionless) time derivative

$$\gamma' = -\frac{1}{3}a\Omega\sin\left(\frac{1}{3}\Omega\tau - \frac{1}{3}d\right) + 2\Lambda\Omega\cos\Omega\tau + O(\epsilon) \tag{4-38}$$

for the case of $\Omega \approx 3$. Notice that the frequency of the free-oscillation term is $\Omega/3$, or one-third of the dimensionless frequency ratio; consequentially, such secondary resonances are known as *subharmonic resonances of order one-third* [24 pp. 197-198]. Such resonances can exhibit a very large response in spite of being far from $\Omega \approx 1$.

Case 2: $\boldsymbol{\Omega} \approx {}^{\mathbf{1}}/_{\mathbf{3}}$

In this case, the slowly varying terms are $\cos[(1-3\Omega)\tau + b]$ and $\sin[(1-3\Omega)\tau + b]$. Thus, the parameters are governed by

$$\frac{\partial a}{\partial T_1} = -(\bar{\beta}_e + \bar{\beta}_m)a + \left(\Lambda^3 - \frac{\bar{A}_x\Lambda^2}{4} + \frac{\bar{\mathrm{A}}_\mathrm{y}\Lambda}{2}\right)\cos[(1-3\Omega)\tau + b]$$

$$a\frac{\partial b}{\partial T_1} = -3\Lambda^2 a + \frac{\bar{A}_x\Lambda a}{2} - \frac{3a^3}{8} \tag{4-39}$$

$$+\left(-\Lambda^3 + \frac{\bar{A}_x\Lambda^2}{4} - \frac{\bar{\mathrm{A}}_\mathrm{y}\Lambda}{2}\right)\sin[(1-3\Omega)\tau + b]$$

Similar to the case of $\Omega \approx 3$, a detuning parameter σ is introduced, satisfying $3\Omega =$

$1+\epsilon\sigma$, as well as a new independent parameter defined by $d=\sigma T_1-b$ so that (4-39) may be rewritten as an autonomous system in a and d:

$$
\begin{gathered}
\frac{\partial a}{\partial T_1}=-(\bar{\beta}_e+\bar{\beta}_m)a+\left(\Lambda^3-\frac{\bar{A}_x\Lambda^2}{4}+\frac{\bar{\mathrm{A}}_\mathrm{y}\Lambda}{2}\right)\cos d \\
a\frac{\partial d}{\partial T_1}=\sigma a+3\Lambda^2 a-\frac{\bar{A}_x\Lambda a}{2}+\frac{3a^3}{8}-\left(\Lambda^3-\frac{\bar{A}_x\Lambda^2}{4}+\frac{\bar{\mathrm{A}}_\mathrm{y}\Lambda}{2}\right)\sin d
\end{gathered}
\tag{4-40}
$$

Finding the fixed points of (4-40) with subsequent elimination of d yields

$$
\begin{aligned}
&\frac{9}{64}a^6+\left(\frac{9\Lambda^2}{4}-\frac{3\bar{A}_x\Lambda}{8}+\frac{3\sigma}{4}\right)a^4 \\
&+\left[\left(3\Lambda^2-\frac{\bar{A}_x\Lambda}{2}+\sigma\right)^2+\left(\bar{\beta}_e+\bar{\beta}_m\right)^2\right]a^2 \\
&-2\left(\Lambda^3-\frac{\bar{A}_x\Lambda^2}{4}+\frac{\bar{\mathrm{A}}_\mathrm{y}\Lambda}{2}\right)^2=0
\end{aligned}
\tag{4-41}
$$

which is a cubic equation in a^2. The roots of (4-41) satisfying $a^2\in\mathbb{R}$ give the steady state amplitude of the free-response for a given σ.

Since $b=\sigma T_1-d$, $3\Omega=1+\epsilon\sigma$, and $T_1=\epsilon\tau$, the solution for the case of $\Omega\approx 1/3$ is given by

$$
\gamma=a\cos(3\Omega\tau-d)+2\Lambda\sin\Omega\tau+O(\epsilon) \tag{4-42}
$$

up to $O(\epsilon)$ with time derivative

$$
\gamma'=-3a\Omega\sin(3\Omega\tau-d)+2\Lambda\Omega\cos\Omega\tau+O(\epsilon) \tag{4-43}
$$

Notice that the frequency of the free-oscillation term is 3Ω, or three times the dimensionless frequency ratio; consequentially, such secondary resonances are known as *superharmonic resonances of order three* [24, p. 202].

Case 3: $\boldsymbol{\Omega \approx 0}$

Since τ appears explicitly in the governing equation, it is unclear which time scale (T_0 or T_1) is appropriate to describe a term such as $\cos 2\Omega\tau$. If $\Omega \approx 0$, then $\cos 2\Omega\tau$ is slowly varying. Let $\Omega = \epsilon\sigma$ to express smallness of Ω, and write $\cos 2\Omega\tau = \cos 2\sigma\epsilon\tau = \cos 2\sigma\mathrm{T}_1$. There are no slowly varying terms in the a differential equation, but there is a $\cos 2\Omega\tau$ in the b differential equation, which is slowly varying at $\Omega \approx 0$. The parameters are thus governed by

$$\frac{\partial a}{\partial T_1} = -\left(\bar{\beta}_e + \bar{\beta}_m\right)a$$

$$a\frac{\partial b}{\partial T_1} = \left(3\Lambda^2 a - \frac{\bar{A}_x \Lambda a}{2} + \frac{\bar{\mathrm{A}}_\mathrm{y} a}{2}\right)\cos 2\sigma\mathrm{T}_1 \tag{4-44}$$

From (4-44), it's clear that

$$a = a_0^{-(\bar{\beta}_e + \bar{\beta}_m)T_1}$$

which indicates that the free-oscillation term in (4-21) vanishes in steady state, leaving only the $2\Lambda \sin \Omega\tau$ term – this is the linearized solution presented in Section 4.3, albeit without damping.

Case 4: Ω away from 0, 1, 3, and 1/3

In this case, the only slowly varying terms in (4-30) are the constant terms. Thus, the parameters are governed by

$$\frac{\partial a}{\partial T_1} = -(\bar{\beta}_e + \bar{\beta}_m)a$$

(4-45)

$$a\frac{\partial b}{\partial T_1} = -3\Lambda^2 a + \frac{\bar{A}_x \Lambda a}{2} - \frac{3a^3}{8}$$

Hence both parameters rapidly approach zero, as in the $\Omega \approx 0$ case, and (4-21) becomes the solution to an undamped, harmonically-excited linear oscillator in steady state. This explains why the solution to the linearized system (4-13) presented in Section 4.3, which also includes the additional effect of damping, is predictive of the dynamics of (4-9) far from any resonance peaks.

4.4.3 Primary Resonance

Due to the small divisor term in (4-21), an alternative to (4-18) is proposed as the perturbed system for analysis:

$$\gamma'' + \gamma + \epsilon\left[2(\bar{\beta}_e + \bar{\beta}_m)\gamma' + \bar{A}_y \cos 2\Omega\tau\,\gamma + \frac{1}{2}\bar{A}_x \sin\Omega\tau\,\gamma^2 - \gamma^3 \right.$$

(4-46)

$$\left. - (\Omega^2\bar{\theta}_{max} + \bar{A}_x)\sin\Omega\tau\right] + O(\epsilon^2) = 0$$

where the substitution $\bar{\theta}_{max} = \epsilon\theta_{max}$ is introduced to reflect the smallness of the forcing term, which is valid for weak excitation. The analysis then proceeds as with the secondary resonances. The solution of (4-46) with $\epsilon = 0$ is

$$\gamma = a\cos(\tau + b) \tag{4-47}$$

Notice that (4-46) no longer contains the small divisor term. Taking the (dimensionless) time derivative of (4-47) while treating a and b as constants gives

$$\gamma' = -a\sin(\tau + b) \tag{4-48}$$

However, when $\epsilon \neq 0$, the solution is still of the form (4-47), subject to the constraint (4-48), but with $a = a(\tau)$ and $b = b(\tau)$. Differentiation of (4-47) in light of this gives

$$\gamma' = -a\sin(\tau + b) + a'\cos(\tau + b) - ab'\sin(\tau + b) \tag{4-49}$$

Equation (4-48) with (4-49) implies

$$a'\cos(\tau + b) - ab'\sin(\tau + b) = 0 \tag{4-50}$$

Differentiating (4-48) once more yields

$$\gamma'' = -a\cos(\tau + b) - a'\sin(\tau + b) - ab'\cos(\tau + b) \tag{4-51}$$

Substitution of (4-47), (4-48), and (4-51) into (4-46) with some simplification gives

$$\begin{aligned} &a'\sin(\tau + b) + ab'\cos(\tau + b) \\ &= \epsilon\Big[-2\mathrm{a}\big(\bar{\beta}_e + \bar{\beta}_m\big)\sin(\tau + b) + \mathrm{a}\bar{A}_y\cos 2\Omega\tau\cos(\tau + b) \\ &+ \frac{1}{2}a^2\bar{A}_x\sin\Omega\tau\cos^2(\tau + b) - a^3\cos^3(\tau + b) \\ &- (\Omega^2\bar{\theta}_{max} + \bar{A}_x)\sin\Omega\tau\Big] \end{aligned} \tag{4-52}$$

where the $O(\epsilon^2)$ term has again been ignored. As with the secondary resonances, (4-52) is used along with (4-50) to solve for a'

$$a' = \epsilon \sin(\tau + b) \Big[-2\mathrm{a}\big(\bar{\beta}_e + \bar{\beta}_m\big) \sin(\tau + b) + \mathrm{a}\bar{A}_y \cos 2\Omega\tau \cos(\tau + b)$$

$$+ \frac{1}{2} a^2 \bar{A}_x \sin \Omega\tau \cos^2(\tau + b) - a^3 \cos^3(\tau + b) \quad \text{(4-53)}$$

$$- (\Omega^2 \bar{\theta}_{max} + \bar{A}_x) \sin \Omega\tau \Big]$$

and ab'

$$ab' = \epsilon \cos(\tau + b) \Big[-2\mathrm{a}\big(\bar{\beta}_e + \bar{\beta}_m\big) \sin(\tau + b)$$

$$+ \mathrm{a}\bar{A}_y \cos 2\Omega\tau \cos(\tau + b) + \frac{1}{2} a^2 \bar{A}_x \sin \Omega\tau \cos^2(\tau + b) \quad \text{(4-54)}$$

$$- a^3 \cos^3(\tau + b) - (\Omega^2 \bar{\theta}_{max} + \bar{A}_x) \sin \Omega\tau \Big]$$

Expanding (4-53) and (4-54), eliminating ϵ, and noting that the slowly varying terms are $\cos[(1 - \Omega)\tau + b]$ and $\sin[(1 - \Omega)\tau + b]$, as well as $\sin[2(1 - \Omega)\tau + 2b]$ and $\cos[2(1 - \Omega)\tau + 2b]$ gives

$$\frac{\partial a}{\partial T_1} = -\big(\bar{\beta}_e + \bar{\beta}_m\big) a + \left(\frac{\bar{A}_x a^2}{16} - \frac{\Omega^2 \bar{\theta}_{max}}{2} - \frac{\bar{A}_x}{2} \right) \cos[(1 - \Omega)\tau + b]$$

$$+ \frac{\bar{\mathrm{A}}_{\mathrm{y}} a}{4} \sin[2(1 - \Omega)\tau + 2b]$$

$$\text{(4-55)}$$

$$a \frac{\partial b}{\partial T_1} = -\frac{3a^3}{8} + \left(-\frac{3\bar{A}_x a^2}{16} + \frac{\Omega^2 \bar{\theta}_{max}}{2} + \frac{\bar{A}_x}{2} \right) \sin[(1 - \Omega)\tau + b]$$

$$+ \frac{\bar{\mathrm{A}}_{\mathrm{y}} a}{4} \cos[2(1 - \Omega)\tau + 2b]$$

with $o.t.$ again representing other terms that are slowly varying near the primary resonance near $\Omega \approx 1$. Finally, the detuning parameter σ is introduced, defined by $\Omega = 1 + \epsilon\sigma$, as well as a new independent parameter satisfying $d = \sigma T_1 - b$ so that (4-55) can be represented by the autonomous system

$$\frac{\partial a}{\partial T_1} = -(\bar{\beta}_e + \bar{\beta}_m)a + \left(\frac{\bar{A}_x a^2}{16} - \frac{\Omega^2 \bar{\theta}_{max}}{2} - \frac{\bar{A}_x}{2}\right)\cos d - \frac{\bar{\mathrm{A}}_{\mathrm{y}} a}{4}\sin 2d$$

$$a\frac{\partial d}{\partial T_1} = a\sigma + \frac{3a^3}{8} + \left(-\frac{3\bar{A}_x a^2}{16} + \frac{\Omega^2 \bar{\theta}_{max}}{2} + \frac{\bar{A}_x}{2}\right)\sin d - \frac{\bar{\mathrm{A}}_{\mathrm{y}} a}{4}\cos 2d \tag{4-56}$$

The form of (4-56) differs from (4-35) and (4-40) – as well as from the system of differential equations that describe the parameters for a first-order approximation of the weakly forced Duffing oscillator [24, pp. 205-208] – in two important ways. First, the amplitudes of the $\cos d$ and $\sin d$ terms are no longer simply the inverse of each other; this appears to be a consequence of the $\sin \Omega\tau$ parametric excitation term in (4-46). Secondly, there are $\sin 2d$ and $\cos 2d$ terms (4-56); this appears to be a consequence of the $\cos 2\Omega\tau$ parametric excitation term in (4-46). Due to the additional complexity, even solving for the fixed points of (4-56) represents a challenge. However, some information may be ascertained by examination. The steady state values of a are given by $\partial a/\partial T_1 = 0$, yielding a quadratic in a. Similarly, letting $a\partial d/\partial T_1 = 0$ gives a cubic equation in a. Treating (4-56) as a system of polynomials in a with a finite number of solutions then, by Bézout's theorem, there are at most six solutions, counting multiplicity. Equation (4-56) is also invariant under the transformation $d \to d \pm n2\pi$, $n \in \mathbb{Z}$. Thus, the steady state amplitude may attain up to six values, and the interval of interest for d will be restricted to $d \in [0, 2\pi)$. For a visualization of the phase plane, see Figure 4-9.

Since $b = \sigma T_1 - d$, $\Omega = 1 - \epsilon\sigma$, and $T_1 = \epsilon\tau$, the solution for the case of $\Omega \approx 1$ is

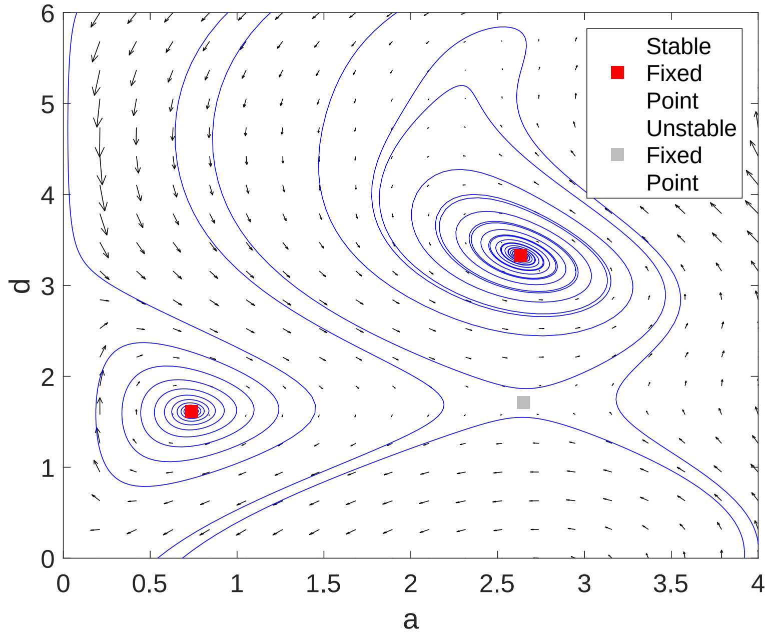

Figure 4-9 – Phase portrait of the ad-plane for (4-56), which governs the primary resonance, under EX5 at $\Omega = 0.6$. The two stable spirals represent higher and lower amplitude solution branches, and a separatrix is formed by the unstable saddle point.

given by

$$\gamma = a\cos(\Omega\tau - d) + O(\epsilon) \tag{4-57}$$

up to $O(\epsilon)$ with (dimensionless) time derivative

$$\gamma' = -a\Omega\sin(\Omega\tau - d) + O(\epsilon) \tag{4-58}$$

4.4.4 Validation of Analysis

The results presented in this section were derived from (4-17) – an approximation to the original system of interest, (4-9) – using approximate analytical methods. To assess the validity of the perturbation solutions (and the system approximation from which they were derived) in predicting the behavior of the original system, a brief comparison between numerical solutions of (4-9) and the perturbation solutions (4-37), (4-42), and (4-57) is presented in this section.

The perturbation solutions were validated in two ways. First, since the amplitude of the free-oscillation terms is the direct output of the averaging method, it is appropriate to compare the amplitude of numerical solutions of (4-9) to the amplitude of the analytical approximations (4-37), (4-42), and (4-57). Since the solutions are not typically simple sinusoids, the amplitude is approximated in all cases by computing half of the difference between the maximum and minimum values attained by the solutions in steady state. Comparisons of power output are used as the second method for validating the analysis, accomplished by the use of the second component (velocity) of the numerical solution to (4-9) and the perturbation solution derivatives (4-38), (4-43), and (4-58), in (4-11) during steady state.

The numerical simulations were performed over a length of 200 swing arm cycles of period $2\pi/\Omega$. Amplitude and power values were computed over some final number of swing arm cycles to be determined, as the solutions near the end of the simulation timespan are presumed to represent a steady state condition. The (smallest) period of (4-42) is $6\pi/\Omega$, or three swing arm cycles; this represents the perturbation solution with the longest period, and therefore three swing arm cycles represents a fair choice for the final number of cycles over which output is computed. However, to account for the possibility of a subharmonic at $\Omega \approx 2$, or any other unexpected nonlinear behavior, the final 30 swing arm cycles of the simulation were instead selected to be representative of a steady state condition. Figure 4-7 and Figure 4-8 were generated under this assumption.

Due to the complexity of the equations, a numerical approach was taken to find the fixed points of (4-56), the primary resonance. For each value of Ω to be plotted, a grid of 1024 initial guess points was formed in the region $-5 \leq a \leq 5$, $0 < d \leq 2\pi$ that was used in a Trust-Region Dogleg algorithm [25] in order to find up to six unique zeros of the right-hand side of (4-56), which correspond to the fixed points of interest. In order to assess stability, the eigenvalues $\lambda_{1,2}$ of the Jacobian

$$J_{\Omega\approx 1} = \begin{bmatrix} -(\bar{\beta}_e + \bar{\beta}_m) + \dfrac{\bar{A}_x a}{8}\cos d - \dfrac{\bar{\mathrm{A}}_{\mathrm{y}}}{4}\sin 2d & -\left(\dfrac{\bar{A}_x a^2}{16} - \dfrac{\Omega^2 \bar{\theta}_{max}}{2} - \dfrac{\bar{A}_x}{2}\right)\sin d - \dfrac{\bar{\mathrm{A}}_{\mathrm{y}} a}{2}\cos 2d \\ \dfrac{3a}{4} - \left(\dfrac{3\bar{A}_x}{16} + \dfrac{\Omega^2 \bar{\theta}_{max}}{2a^2} + \dfrac{\bar{A}_x}{2a^2}\right)\sin d & \left(-\dfrac{3\bar{A}_x a}{16} + \dfrac{\Omega^2 \bar{\theta}_{max}}{2a} + \dfrac{\bar{A}_x}{2a}\right)\cos d + \dfrac{\bar{\mathrm{A}}_{\mathrm{y}}}{2}\sin 2d \end{bmatrix}$$

derived from (4-56) by treating the system as a vector-valued function with (a, d) as the input, were numerically evaluated at each fixed point, with stable fixed points satisfying $\mathrm{Re}(\lambda_{1,2}) < 0$.

The amplitude of the free-oscillation term in steady state for the subharmonic response (4-37) is found directly by solving (4-36), retaining only solutions satisfying $a \in \mathbb{R}$; d may then be found using (4-35). For the subharmonic fixed points, the Jacobian

$$J_{\Omega\approx 3} = \begin{bmatrix} \bar{\beta}_e + \bar{\beta}_m & -\left(\sigma + 9\Lambda^2 - \dfrac{3\bar{A}_x \Lambda}{2}\right)\dfrac{a}{3} - \dfrac{3a^3}{8} \\ -\left(\sigma + 9\Lambda^2 - \dfrac{3\bar{A}_x \Lambda}{2}\right)\dfrac{1}{a} + \dfrac{9a}{8} & -3(\bar{\beta}_e + \bar{\beta}_m) \end{bmatrix}$$

derived from (4-35) was used to assess stability. To assess the stability of the $a = 0$ subharmonic solution, treat the amplitude equation of (4-35) as flow on the line, since the dynamics of the phase d are irrelevant if the amplitude of the free-oscillation term is zero. Then

$$\frac{\partial a}{\partial T_1 \partial a} = -(\bar{\beta}_e + \bar{\beta}_m) + 2a\left(\frac{\bar{A}_x}{16} - \frac{3\Lambda}{4}\right)\cos d$$

Hence

$$\left.\frac{\partial a}{\partial T_1 \partial a}\right|_{a=0} = -(\bar{\beta}_e + \bar{\beta}_m)$$

which implies $a = 0$ is always stable for the subharmonic resonance.

Finally, the amplitude of the free-oscillation term in steady state for the superharmonic response (4-42) is found directly by solving (4-41), again retaining only solutions satisfying $a \in \mathbb{R}$; d may then be found using (4-40). For the superharmonic fixed points, the Jacobian

$$J_{\Omega\approx\frac{1}{3}} = \begin{bmatrix} -(\bar{\beta}_e + \bar{\beta}_m) & -\left(\sigma + 3\Lambda^2 - \frac{\bar{A}_x\Lambda}{2}\right)a - \frac{3a^3}{8} \\ \left(\sigma + 3\Lambda^2 - \frac{\bar{A}_x\Lambda}{2}\right)\frac{1}{a} + \frac{9a}{8} & -(\bar{\beta}_e + \bar{\beta}_m) \end{bmatrix}$$

derived from (4-40) was used to assess stability.

Figure 4-10 presents the amplitude of the numerical solution of (4-9), as well as the perturbation solutions (4-37), (4-42), and (4-57), vs. frequency Ω for EX5. The correspondence is generally acceptable, especially considering the forcing is not particularly weak. Notice the additional, small resonance near $\Omega \approx 1/4$ that has not been resolved by the first-order expansion. The lack of numerical points that coincide with the highest-amplitude branches in Figure 4-10 should not be of concern, as the leftward-bending of the superharmonic and primary resonances (sometimes referred to as the *foldover effect*) produces hysteresis in the response, in which the path taken by the solution

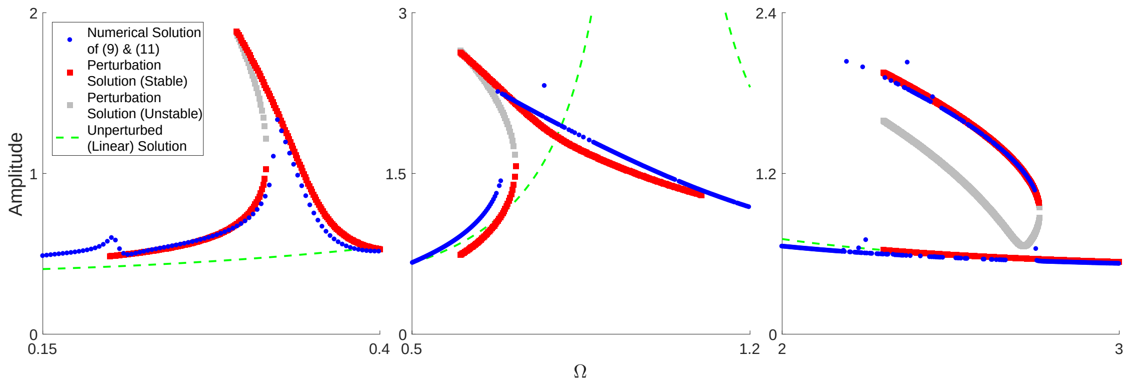

Figure 4-10 – Comparison of numerical and perturbation approximations of solution amplitude of (left) superharmonic resonance, (center) primary resonance, and (right) subharmonic resonance vs. Ω for EX5.

determines whether the steady state response lies on the higher or lower solution branch. Since all numerical simulations begin with zero initial conditions, it is unsurprising that points tend not to lie on the uppermost branches. Some license has been taken in producing a comparison between numerical and approximate solutions, as the range of frequencies over which to plot the perturbation solution may be chosen freely – although solution accuracy degrades far from the solution's corresponding resonance frequency.

Using the perturbation solutions to compute power, Figure 4-7 may now be reproduced to help explain the nonlinear behavior under EX1, shown in Figure 4-11. Notice that the perturbation solutions predict the relatively flat superharmonic response for EX1, and accurately predict the frequency of the onset of primary resonance from the lower-amplitude solution branch. As the error in the approximate solutions propagates when power is computed using (4-11), the fit is not expected to be as close in a power vs. frequency plot such as Figure 4-11.

An interesting feature of Figure 4-11 is the existence of the high-amplitude

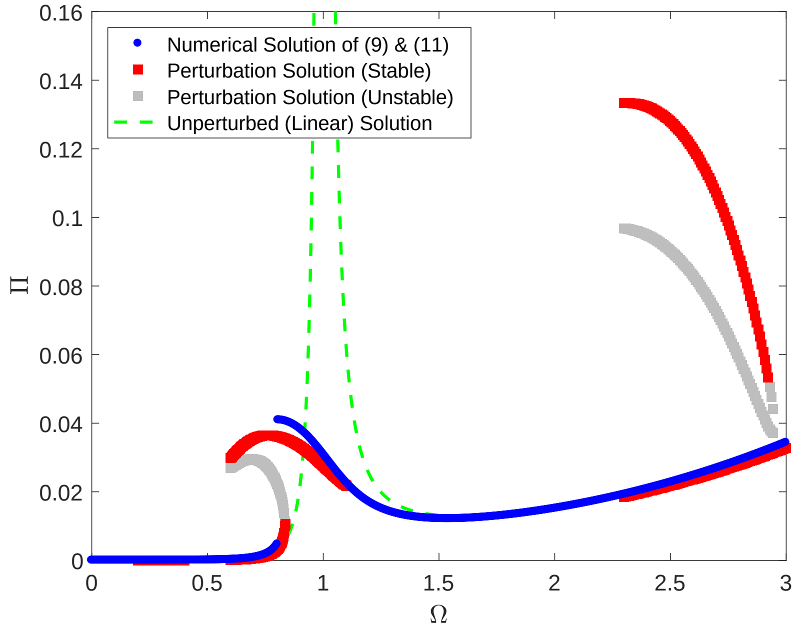

Figure 4-11 – Numerical vs. analytical (linearization and perturbation) results for power vs. frequency ratio using EX1 input

subharmonic branch with no coinciding numerical solution points, which may seem concerning with respect to validation. However, much like the high-amplitude branches of the primary resonance, this can be explained by the fact that all numerical solutions of (4-9) were integrated using zero initial conditions, and the region of attraction for the high-amplitude branch of the subharmonic is very small (Figure 4-12).

Finally, Figure 4-8 may be reproduced, again overlaying the power output of the perturbation solutions for EX5 (Figure 4-13). The perturbation solutions again accurately capture the qualitative effect of the nonlinear resonance peaks and are fairly predictive of the frequency at which the lower solution branch of the primary resonance transitions to the higher-amplitude branch.

The perturbation solutions of the system approximation (4-17) are therefore

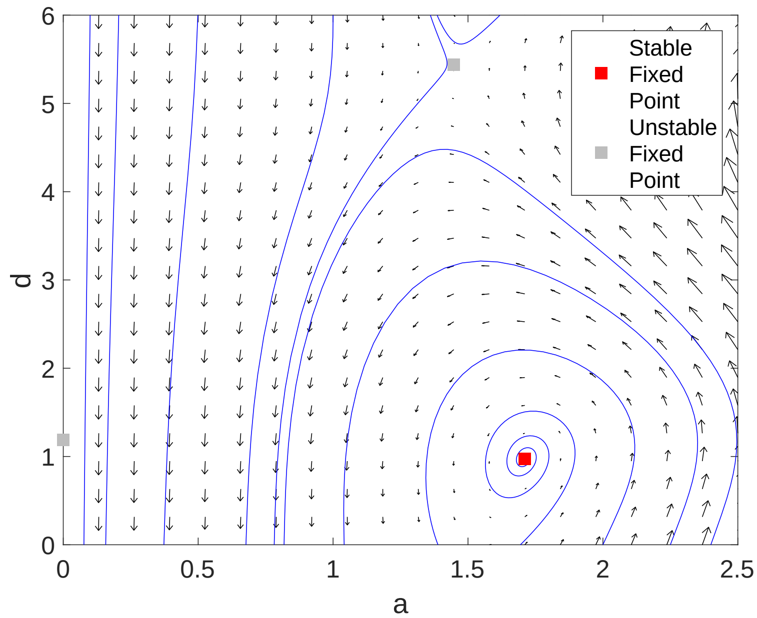

Figure 4-12 – Phase portrait of the ad-plane for (4-35)(4-56), which governs the subharmonic resonance, under EX1 at $\Omega = 2.5$. Notice that the region of attraction for the high-amplitude solution is small, and nearly all points approach $a = 0$ as $T_1 \rightarrow \infty$.

predictive of the dynamics of the true eccentric rotor model (4-9). The steady state amplitudes of the perturbation solutions are in good agreement with the amplitudes of the numerical solutions of (4-9). Power output is more difficult to predict with accuracy, however, due to the propagation of error when the approximate solutions are used in (4-11), but qualitative effects of the solutions are captured well.

4.4.5 Invariance of Power Output at Primary Resonance

Compare the steady state power output at the sharp transition to primary resonance for EX1 (Figure 4-11) and EX5 (Figure 4-13); remarkably, in spite of the substantial difference in the strength of the two excitations, the steady state power output is nearly identical ($\Pi \approx 0.04$) in either case, possibly due to the effect of saturation. An interest in

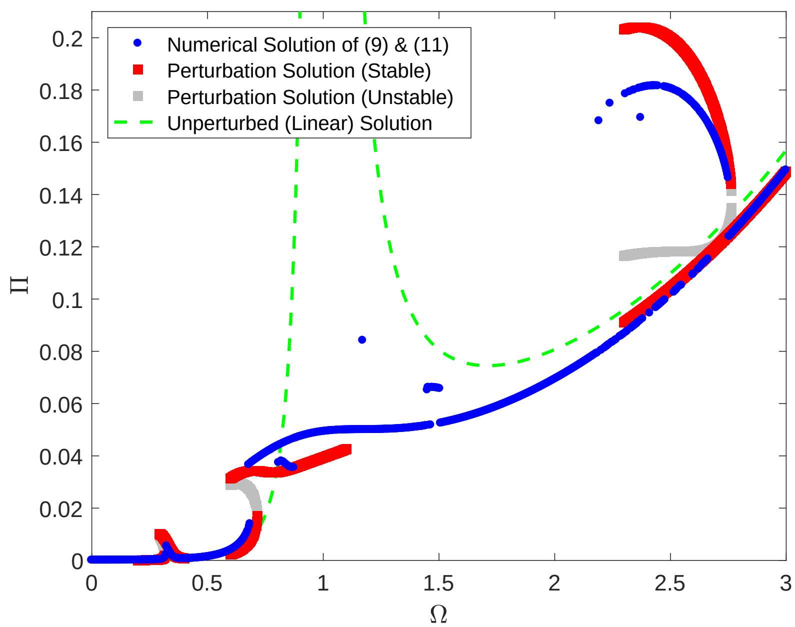

Figure 4-13 – Numerical vs. analytical (linearization and perturbation) results for power vs. frequency ratio using EX5 input

how the primary resonance peak behaves as the excitation is changed led to the numerical investigation presented in Figure 4-14, wherein the rotor model (4-9) is numerically integrated for Ω values near the primary resonance and power is again computed using (4-11). Recall that, for a given excitation, a change in Ω amounts to a change in the harvester's natural frequency.

The results of the numerical investigation of the primary resonance suggest that an eccentric rotor designed to exhibit a frequency ratio of $\Omega \approx 0.8$ under EX1 will continue to exhibit the high-amplitude response from swing arm excitation that the primary resonance affords even with increasing input frequency (as this shifts Ω rightward) and swing arm amplitude.

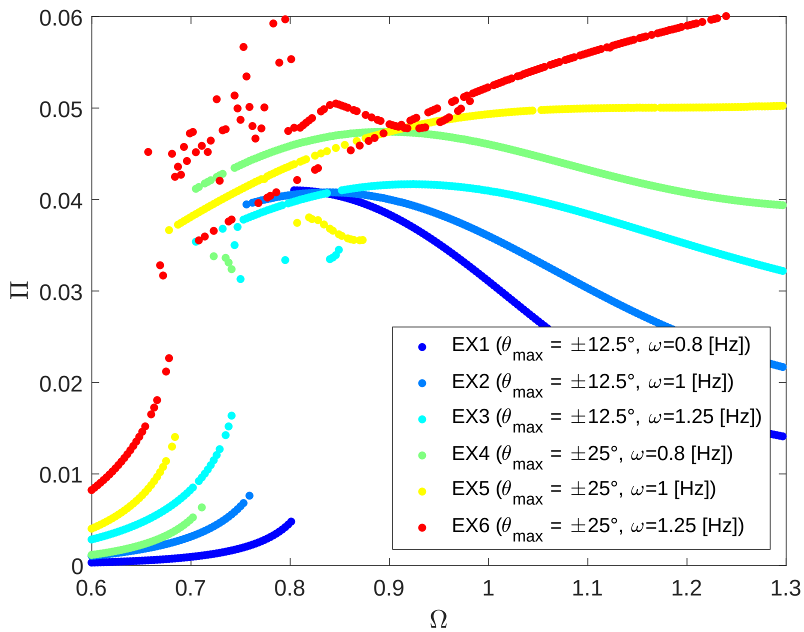

Figure 4-14 – Steady state power output at primary resonance for all excitations from Table 4-1

4.4.6 Summary

Some of the primary results of the analysis presented in this section are succinctly listed below:

- The eccentric rotor model (4-9) exhibits behavior characteristic of a Duffing oscillator with a softening spring nonlinearity in spite of differences in nonlinearities and the addition of parametric excitation. This includes secondary resonances at $\Omega \approx 1/3$ and $\Omega \approx 3$, and a primary resonance exhibiting the foldover effect.
- The peak at $\Omega \approx 1/3$ is a nonlinear superharmonic resonance. Its magnitude relative to the primary resonance is generally small and is strongly dependent on the forcing.

- The peak at $\Omega \approx 3$ is a nonlinear subharmonic resonance. Its magnitude is large and it extends over a wide range of Ω values; however, the coexistence of high-amplitude and a low-amplitude solution branches and seemingly small regions of attraction for the high-amplitude branch under weak forcing suggest that consistent operation at the high-amplitude branch would be difficult to achieve in practice.
- The amplitude of the primary resonance is highly consistent under all excitations listed in Table 4-1, and the behavior of this peak provides an exploitable design opportunity.

4.5 Resonant Eccentric Rotor Design

Following the observations of the behavior of the primary resonance peak in Section 4.4, a resonant eccentric rotor harvester design is proposed and evaluated against a comparable non-resonant design.

Consider again, as in Section 4.3.1, a homogeneous tungsten cylindrical sector rotor geometry with density $\rho = 19000$ kg·m^{-3}, angle α, radius r, height h, total device volume $\pi r^2 h = 1$ cm^{-3} and thickness 2 mm, requiring a radius $r \approx 12.6$ mm. By prudent selection of the effective length, l_{eff}, an eccentric rotor design with a frequency ratio $\Omega \approx 0.8$ under EX1 may be obtained; an effective length of $l_{eff} \approx 0.18$ m is once such choice, which can be realized with an angle $\alpha \approx 5.97$ rad – nearly a full cylinder of tungsten. Whether such a resonant design will maintain high power output as the forcing parameters A_x and A_y change with the input frequency can be ascertained via numerical simulation of the dimensioned system (4-3). A choice of $b_e = 1.3 \cdot 10^{-6}$ N·m·s·rad^{-1} for the electrical damping coefficient was selected for the resonant device. The optimized non-resonant device from Section 4.3.1 ($\alpha \approx 3.42$ rad, $b_e = 8.6 \cdot 10^{-6}$ N·m·s·rad^{-1}) was selected as a benchmark against which to gauge the performance of the resonant device. Equation (4-3) was solved numerically for each device over a period for 20 swing arm cycles, and the final three swing arm periods were used as the time span t_0 in (4-4) over which power output was calculated. An arbitrary mechanical damping coefficient of $b_m = 8.6 \cdot 10^{-6}$ N·m·s·rad^{-1} was used to represent loss in each device. The results of the numerical simulations are presented in Figure 4-15.

As can be seen in Figure 4-15, the resonant design is capable of producing high power output over a large range of swing arm frequencies. Only at the highest frequencies simulated did the non-resonant design begin to outperform the resonant design. However,

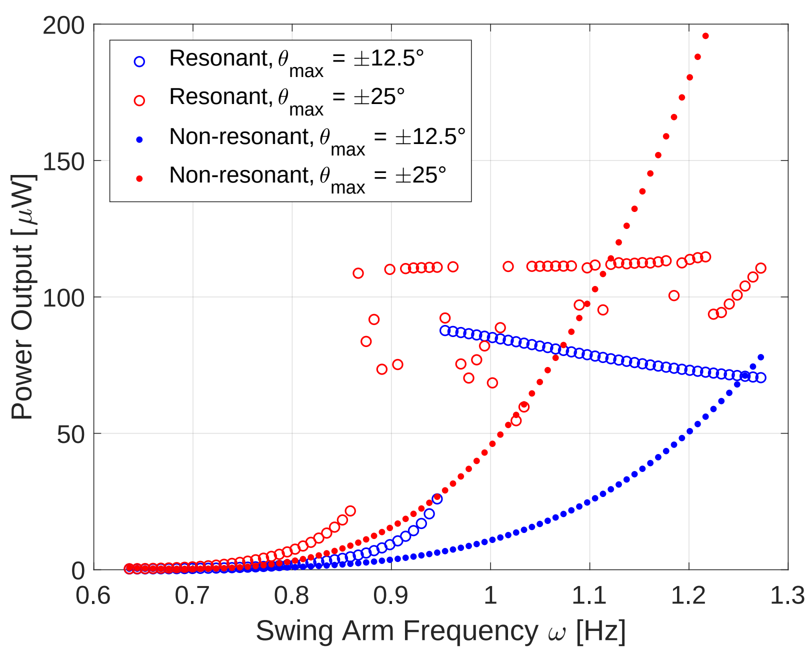

Figure 4-15 – Power vs. swing arm frequency for two example resonant and non-resonant eccentric rotor designs the non-resonant design benefits tremendously from the high degree of electrical damping – nearly seven times as high as the electrical damping of the resonant device. In order to realize such a level of damping in practice, some additional portion of the device volume would need to be consumed by a transducer, which is volume that could otherwise be shared by additional harvester mass. For a more fair comparison, another set of simulations using an electrical damping coefficient of $b_e = 1.3 \cdot 10^{-6}$ N·m·s·rad^{-1} for *both* devices was performed (Figure 4-16).

As evidenced in Figure 4-16, a resonant design is capable of producing higher power over a wider range of swing arm frequencies than a comparable non-resonant device when the device volumes and electrical damping coefficients are matched.

It is also worth noting that the design of a rotor with a wideband response at the

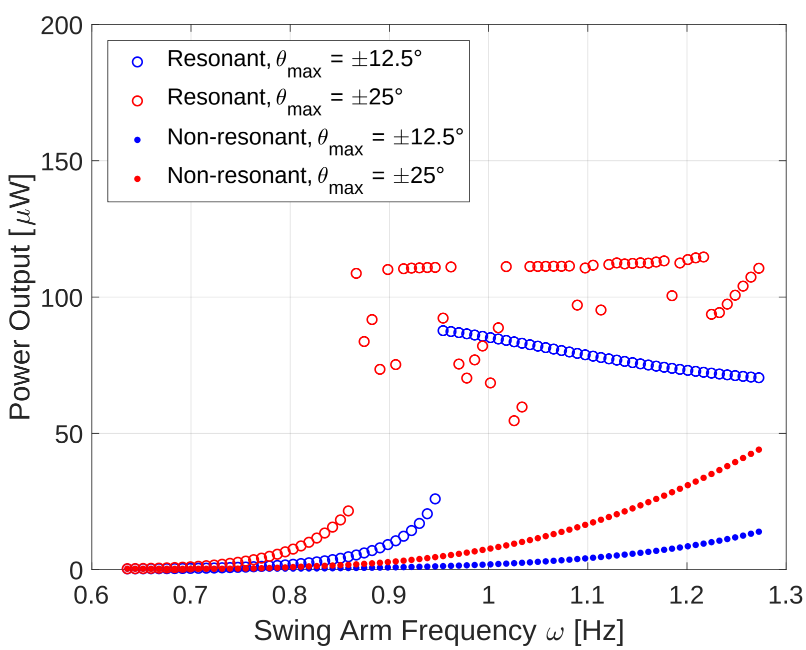

Figure 4-16 – Power vs. swing arm frequency for two example resonant and non-resonant eccentric rotor designs with equal values of electrical damping primary resonance peak is aided by a mild self-tuning phenomenon of the eccentric rotor over the range of excitations considered in Table 4-1. Recall that the natural frequency $\omega_0 = \sqrt{\bar{y}/l_{eff}}$, and that the average y -acceleration $\bar{y} = g(1 - \theta_{max}^2/4) + \theta_{max}^2 l_{arm} \omega^2/2$. This means that $\omega_0 = \omega_0(\omega)$, which increases as the input excitation frequency ω increases; that is, the harvester resonance frequency tends to move with the input frequency. This effect has been observed and exploited in other energy harvesting devices with pendulum dynamics [26], [27].

4.6 Conclusions

The dynamical analysis of an eccentric rotor harvester under swing arm excitation has been presented. A linearized system model predicts the behavior of non-resonant devices well, provided the natural frequency of the device is far from the primary resonance, or nonlinear secondary resonances. It was shown that the eccentric rotor harvester behaves very similar to a Duffing oscillator with softening spring nonlinearity. The relatively small magnitude of the superharmonic resonance and the coexistence of high- and low-amplitude solution branches for the subharmonic resonance makes targeting these resonance peaks in a practical design challenging. However, the behavior of the primary resonance peak makes it ideal for harvesting, since power output appears insensitive to changes in input excitations at this resonance. A novel resonant eccentric harvester was proposed to exploit this behavior, and its performance compared to a non-resonant design via simulation to demonstrate its consistently high power output.

The entire analysis presented in this work assumes a steady state harvesting condition; for excitations derived from human motion, this is likely a rare operating condition. Future work should incorporate transient analysis, as this may have a significant impact on the design approach for an eccentric rotor harvester.

4.7 Acknowledgments

The authors would like to express their gratitude to Alexander Balk and Andrejs Treibergs, for their generosity with their time spent participating in discussions on perturbation methods and nondimensionalization, as well as Analog Devices Inc., for the grant that made this work possible.

4.8 References

[1] P. Pillatsch, E. M. Yeatman, and A. S. Holmes, "A piezoelectric frequency up-converting energy harvester with rotating proof mass for human body applications," *Sensors Actuators, A Phys.*, vol. 206, pp. 178–185, 2014.

[2] L. Xie and R. Du, "Harvest human kinetic energy to power portable electronics," *J. Mech. Sci. Technol.*, vol. 26, no. 7, pp. 2005–2008, 2012.

[3] T. Xue, X. Ma, C. Rahn, and S. J. Roundy, "Analysis of upper bound power output for a wrist-worn rotational energy harvester from real-world measured inputs," in *J. Phys. Conf. Ser.*, vol. 557, 2014.

[4] R. Lockhart, P. Janphuang, D. Briand, and N. F. de Rooij, "A wearable system of micromachined piezoelectric cantilevers coupled to a rotational oscillating mass for on-body energy harvesting," in *2014 IEEE 27th Int. Conf. Micro Electro Mech. Syst.*, pp. 370–373, 2014.

[5] E. Romero, M. R. Neuman, and R. O. Warrington, "Rotational energy harvester for body motion," in *2011 IEEE 24th Int. Conf. Micro Electro Mech. Syst.*, pp. 1325–1328, 2011.

[6] J. Nakano, K. Komori, Y. Hattori, and Y. Suzuki, "MEMS rotational electret energy harvester for human motion," in *J. Phys. Conf. Ser.*, vol. 660, 2015.

[7] M. Adachi, T. Miyoshi, K. Suzuki, Q. Fu, Q. Fang, and Y. Suzuki, "Development of rotational electret energy harvester using print circuit board," in *J. Phys. Conf. Ser.*, vol. 1052, 2018.

[8] M. Hayakawa, “Electronic wristwatch with generator,” US5001685 A, 1991.

[9] Kinetron, “Micro Generator System ‘26.4,’” 2014.

[10] F. J. Romeiras and E. Ott, “Strange nonchaotic attractors of the damped pendulum with quasiperiodic forcing,” *Phys. Rev. Appl.*, vol. 35, no. 10, pp. 4404–4413, 1987.

[11] J. B. Mclaughlin, “Period-doubling bifurcations and chaotic motion for a parametrically forced pendulum,” *J. Stat. Phys.*, vol. 24, no. 2, pp. 375–388, 1981.

[12] B. P. Koch and R. W. Leven, “Subharmonic and homoclinic bifurcations in a parametrically forced pendulum,” *Phys. D Nonlinear Phenom.*, vol. 16, no. 1, 1985.

[13] X. Xu and M. Wiercigroch, “Approximate analytical solutions for oscillatory and rotational motion of a parametric pendulum,” *Nonlinear Dyn.*, vol. 47, pp. 311–320, 2007.

[14] R. Rantz, M. A. Halim, T. Xue, Q. Zhang, L. Gu, and K. Yang, “Architectures for wrist-worn energy harvesting,” *Smart Mater. Struct.*, vol. 27, no. 4, 2018.

[15] A. Cadei, A. Dionisi, E. Sardini, and M. Serpelloni, “Kinetic and thermal energy harvesters for implantable medical devices and biomedical autonomous sensors,” *Meas. Sci. Technol.*, vol. 25, no. 1, p. 012003, 2014.

[16] E. Romero, R. O. Warrington, M. R. Neuman, and S. Member, “Body motion for powering biomedical devices,” in *2009 Annual International Conference of the IEEE Engineering in Medicine and Biology Society*, pp. 2752–2755, 2009.

[17] B. Gutnik, H. MacKie, G. Hudson, and C. Standen, “How close to a pendulum is human upper limb movement during walking?,” *HOMO- J. Comp. Hum. Biol.*, vol. 56, no. 1, pp. 35–49, 2005.

[18] D. Webb, R. H. Tuttle, and M. Baksh, “Pendular activity of human upper limbs during slow and normal walking,” *Am. J. Phys. Anthropol.*, vol. 93, no. 4, pp. 477–489, 1994.

[19] P. D. Mitcheson, T. C. Green, E. M. Yeatman, and A. S. Holmes, “Architectures for vibration-driven micropower generators,” *J. Microelectromechanic Syst.*, vol. 13, no. 3, pp. 429–440, 2004.

[20] C. B. Williams and R. B. Yates, “Analysis of a micro-electric generator for microsystems,” *Sensors Actuators A Phys.*, vol. 52, no. 1–3, pp. 8–11, 1996.

[21] S. J. Roundy, P. K. Wright, and J. Rabaey, “A study of low level vibrations as a power source for wireless sensor nodes,” *Comput. Commun.*, vol. 26, no. 11, pp. 1131–1144, 2003.

[22] S. J. Roundy and P. K. Wright, “A piezoelectric vibration based generator for

wireless electronics,” *Smart Mater. Struct.*, vol. 13, no. 5, pp. 1131–1142, 2004.

[23] D. W. Jordan and P. Smith, *Nonlinear Ordinary Differential Equations : An Introduction for Scientists and Engineers*, 4th ed. Oxford University Press, 2007.

[24] N. Hasan, *Introduction to Perturbation Techniques.* John Wiley & Sons, Inc., 1993.

[25] M. J. D. Powell, *Numerical Methods for Nonlinear Algebraic Equations*. P. Rabinow, 1970.

[26] L. Gu, C. Livermore, and U. States, “Pendulum-driven passive self-tuning energy harvester for rotating applications,” in *Power MEMS Work. Leuven, Belgium*, 2010.

[27] S. J. Roundy and J. Tola, “An energy harvester for rotating environments using offset pendulum dynamics,” *Smart Mater. Struct.*, vol. 23, no. 10, 2014.

CHAPTER 5

CONCLUSIONS

This project begins with a review of the state-of-the-art in energy harvesting from human motion, with a focus on harvesters capable of scavenging energy from the wrist from arm swing during walking. The vibratory excitations observed at the wrist during walking are typically characterized as low-frequency with moderate to large amplitudes; harvesting energy from such excitations using traditional, linear energy harvesting techniques is challenging as such devices generally do not perform well on the body when device dimensions are highly constrained. A number of architectures have been proposed to remedy this issue and improve performance in body-worn applications. An inability to assess the relative merits of each harvester approach warranted a comparative analysis, the result of which lead to the design and development of sprung and unsprung eccentric rotor harvester prototypes. These prototypes were characterized using a benchtop excitation and populations of human subjects walking under controlled conditions. Finally, a dynamical analysis of the eccentric rotor architecture was performed, which yielded a regime of operation that may be beneficial to exploit in practice to achieve higher power output over non-resonant devices. What follows are the primary results of the project.

5.1 Comparative Analysis

In Chapter 2, a comparative analysis was performed in order to determine the harvester architecture best suited for absorbing kinetic energy at the wrist. Six device architectures were proposed and modeled. It was determined that the sprung eccentric rotor architecture was superior for energy harvesting at the wrist in two ways: first, it produced, on average, more power output under human walking excitation than its primary competition, a sprung translational harvester. Secondly, the optimal design parameters of the eccentric rotor exhibited less variation compared to the translational harvester, which means that an eccentric rotor design using averaged optimized design parameters performs better under walking excitation from a population of subjects than a translational harvester designed in the same fashion.

5.2 Experimental Characterization

With the results of the comparative analysis in hand, a series of eccentric rotor prototypes were developed and characterized, as detailed in Chapter 3. Early designs primarily served as a means to corroborate the mathematical models and demonstrate the increase in power that comes with the addition of a torsional spring to the eccentric rotor architecture; average power for the human subject population walking at 2.5 mph increased by a factor of over 15 using the third-generation prototype as a result of the addition of a spring. Results generally conformed to the predictions of the model, although it is difficult to accurately predict power output for an unsprung eccentric rotor for any particular individual. Later prototype iterations served as proofs-of-concept for compact devices with improved power density. Devices occupying 2 cm^3 were developed, which incorporated custom annular section magnets, wound coil arrays, and nested torsional springs.

5.3 Dynamical Analysis

The work of Chapter 4 sought to bring some clarity to the function of eccentric rotor devices through a basic analysis of the dynamics under a benchtop pseudo-walking signal. It was observed that all inertial parameters collapse to a single natural frequency parameter, which affects the dynamics through a dimensionless frequency ratio, Ω. A linearized model helped to explain the large resonance peak observed near $\Omega \approx 1$, and a power output function based on the linearization generally fit the power output of the nonlinear system well. Perturbation solutions provide insight into the behavior where the linearization cannot, showing that the system shares many features in common with a Duffing oscillator with a softening spring nonlinearity, and the analysis additionally gives reason to target the primary resonance as a regime of operation in a real device. This result guided the proposal for a resonant eccentric rotor harvester that appears to exhibit a wideband response in simulations with a low requirement for electrical damping.

5.4 Original Contribution

The primary original contributions of this project are succinctly listed below:

- A comparative analysis between harvester architectures was developed in order to determine which architecture is best suited for harvesting energy at the wrist. It was shown that a sprung eccentric rotor architecture is superior in this application
- A novel architecture – the sprung eccentric rotor – was proposed, and its

performance compared to identical devices without a torsional spring was rigorously characterized. The characterization demonstrated that the addition of a torsional spring can greatly improve the power output of a wrist-worn eccentric rotor harvester under walking excitation.

- A dynamical analysis of the eccentric rotor architecture shed light on the origin of some observed nonlinear behavior, and also revealed an exploitable resonance phenomenon. Many authors had considered resonance to be an ill-suited design goal for body-worn energy harvesting, but a proposed resonant eccentric rotor design exhibited improved power output over a non-resonant design using a range of input frequencies in simulation.

5.5 Future Work

Work on wrist-worn energy harvesters and, in particular, eccentric rotor harvesters is far from complete. Below are some recommendations for future work with a basis in the efforts and results presented in this dissertation:

- Consider transient operation in the design of eccentric rotor harvesters. Only steady-state dynamics have been considered in the analysis, and experiments carried out both on the benchtop and with human subjects considered performance only after transient effects were presumed to have dissipated. In real operation, there may only be short bursts of excitation or the excitation may be inconsistent, such that transient dynamics may dominate the behavior and, consequently, the power output of a design.

- A dynamical analysis of the sprung eccentric rotor architecture would be helpful in explaining why the addition of a spring yields such an improvement in device performance, beyond merely speculating based on the characteristics of a power vs. spring stiffness curve and study of the numerical solutions.
- Refine designs to prepare for commercialization. The addition of a torsional spring to the eccentric rotor architecture complicates the design in two ways: first, the additional component consumes volume and increases parasitic loss. Second, it makes the device orientation-dependent, which may necessitate the design a left- and right-hand version of the device. Alternative methods for imposing a restoring torque should be explored.
- Experimentally validate the performance of the resonant eccentric rotor design proposed in Chapter 4. Although the nonlinear model used to make the performance predictions of the resonant eccentric rotor has been well-validated, its accuracy has not been experimentally confirmed in this particular regime of device operation. Additional validation is necessary.

APPENDIX A

EXTENDED MODEL DERIVATION

What follows in an extended derivation of the planar eccentric rotor model used throughout this work. A schematic used in the derivation of the planar rotor model is shown in Figure A-1, and all variables used in the derivation are defined in Table A-1.

A remark on notation: vectors are denoted by lower-case bold letters with subscripts and superscripts, such as ${}^{i}\boldsymbol{v}_{j}$. The superscript denotes the particular coordinate frame i in which the coordinates of $\boldsymbol{v}_j$ are expressed. Points (such as those that denote an origin) are upper-case letters. Scalars are Roman script. Angles are expressed in Greek letters.

Gravity will be ignored in this derivation without loss of model generality, as gravitational acceleration may be considered acceleration input. The potential energy of the system is

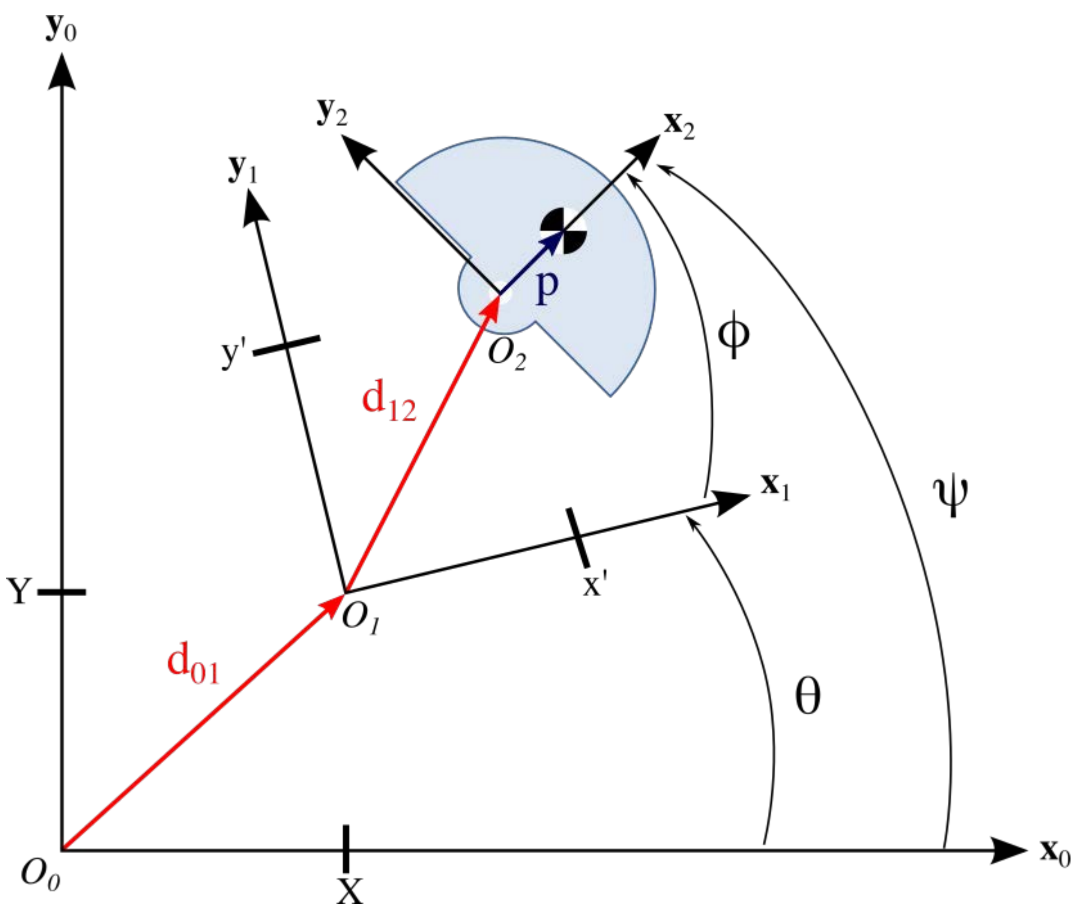

Figure A-1 – Schematic used in the derivation of the rotor model

Table A-1 – List of variables used in the derivation of the eccentric rotor model

Variable	**Definition**
m	Mass of rotor
I_g	Moment of inertia of rotor about center of gravity
L	Eccentric length; distance from rotating center to center of mass measured along rotor centerline (line passing through rotating center and center of mass)
b	Linear viscous damping coefficient for rotational damper
ψ	Angle of centerline of rotor as measured from basis vector $\boldsymbol{x}_0$
θ	Angle of basis vector $\boldsymbol{x}_1$ as measured from basis vector $\boldsymbol{x}_0$ (“housing angle’)
ϕ	Angle of basis vector $\boldsymbol{x}_2$ as measured from basis vector $\boldsymbol{x}_1$ (“relative rotor angle”)
X	Scalar displacement of O_1 in basis vector $\boldsymbol{x}_0$ direction (“absolute housing displacement”)
Y	Scalar displacement of O_1 in basis vector $\boldsymbol{y}_0$ direction (“absolute housing displacement”)
x'	Scalar displacement of O_2 in basis vector $\boldsymbol{x}_1$ direction
y'	Scalar displacement of O_2 in basis vector $\boldsymbol{y}_1$ direction
$\boldsymbol{p}$	Displacement vector from O_2 to center of gravity (Eccentric length, $\lVert\boldsymbol{p}\rVert = L$)
$\boldsymbol{d}_{01}$	Inter-origin vector from O_0 to O_1
$\boldsymbol{d}_{12}$	Inter-origin vector from O_1 to O_2
${}^0R_1$	Rotation matrix from coordinate frame O_1 to O_0
${}^1R_2$	Rotation matrix from coordinate frame O_2 to O_1

$$U = 0$$

since gravity is considered to be an effective acceleration of the point O_1.

Kinetic energy is considered at the center of mass of the rotor, and is composed of translational and rotational components:

$$T = \frac{1}{2}m\lVert\boldsymbol{v}\rVert^2 + \frac{1}{2}I_g\dot{\psi}^2$$

We want to locate the point ${}^{\mathbf{2}}\boldsymbol{p} = \begin{bmatrix} L \\ 0 \end{bmatrix}$ in O_0. Express the displacement vector as

$$
\begin{aligned}
{}^{\mathbf{0}}\boldsymbol{r} &= {}^{0}\boldsymbol{d}_{01} + {}^{0}R_1 {}^{1}\boldsymbol{d}_{12} + {}^{0}R_1 {}^{1}R_2 {}^{2}\boldsymbol{p} \\
&= \begin{bmatrix} X \\ Y \end{bmatrix} + \begin{bmatrix} \cos\theta & -\sin\theta \\ \sin\theta & \cos\theta \end{bmatrix} \begin{bmatrix} x' \\ y' \end{bmatrix} + \begin{bmatrix} \cos\theta & -\sin\theta \\ \sin\theta & \cos\theta \end{bmatrix} \begin{bmatrix} \cos\phi & -\sin\phi \\ \sin\phi & \cos\phi \end{bmatrix} \begin{bmatrix} L \\ 0 \end{bmatrix} \\
&= \begin{bmatrix} X \\ Y \end{bmatrix} + \begin{bmatrix} \cos\theta & -\sin\theta \\ \sin\theta & \cos\theta \end{bmatrix} \begin{bmatrix} x' \\ y' \end{bmatrix} + \begin{bmatrix} \cos\theta & -\sin\theta \\ \sin\theta & \cos\theta \end{bmatrix} \begin{bmatrix} L\cos\phi \\ L\sin\phi \end{bmatrix} \\
&= \begin{bmatrix} X + x'\cos\theta - y'\sin\theta + L(\cos\theta\cos\phi - \sin\theta\sin\phi) \\ Y + x'\sin\theta + y'\cos\theta + L(\sin\theta\cos\phi + \cos\theta\sin\phi) \end{bmatrix} \\
&= \begin{bmatrix} X + x'\cos\theta - y'\sin\theta + L\cos(\theta+\phi) \\ Y + x'\sin\theta + y'\cos\theta + L\sin(\theta+\phi) \end{bmatrix}
\end{aligned}
$$

So far, we have assumed nothing about the nature of x' and y' (the displacements of O_2 as measured from O_1). This was done for generality. Now assume $x' = y' = 0 = constant$, which corresponds to the axis of rotation coinciding with coordinate frame of O_1 for all time. This yields

$$
{}^{\mathbf{0}}\boldsymbol{r} = \begin{bmatrix} X + L\cos(\theta+\phi) \\ Y + L\sin(\theta+\phi) \end{bmatrix} = \begin{bmatrix} X + L\cos(\psi) \\ Y + L\sin(\psi) \end{bmatrix}
$$

Differentiate ${}^{\mathbf{0}}\boldsymbol{r}$:

$$
\frac{d}{dt}{}^{\mathbf{0}}\boldsymbol{r} = \boldsymbol{v} = \begin{bmatrix} \dot{X} - L\dot{\psi}\sin\psi \\ \dot{Y} + L\dot{\psi}\cos\psi \end{bmatrix}
$$

Substitute $\boldsymbol{v}$ into the expression for kinetic energy:

$$
\begin{aligned}
T &= \frac{1}{2}m\|\boldsymbol{v}\|^2 + \frac{1}{2}I_g\dot{\psi}^2 \\
&= \frac{1}{2}m\boldsymbol{v}\cdot\boldsymbol{v} + \frac{1}{2}I_g\dot{\psi}^2
\end{aligned}
$$

$$= \frac{1}{2}m\left(\begin{bmatrix}\dot{X} - L\dot{\psi}\sin\psi \\ \dot{Y} + L\dot{\psi}\cos\psi\end{bmatrix} \cdot \begin{bmatrix}\dot{X} - L\dot{\psi}\sin\psi \\ \dot{Y} + L\dot{\psi}\cos\psi\end{bmatrix}\right) + \frac{1}{2}I_g\dot{\psi}^2$$

$$= \frac{1}{2}m\left[\left(\dot{X} - L\dot{\psi}\sin\psi\right)^2 + \left(\dot{Y} + L\dot{\psi}\cos\psi\right)^2\right] + \frac{1}{2}I_g\dot{\psi}^2$$

Now account for the linear viscous damping. The Rayleigh dissipation function is

$$R = \frac{1}{2}b\left(\dot{\psi} - \dot{\theta}\right)^2$$

Invoke the modified Euler-Lagrange for the equations of motion:

$$\frac{d}{dt}\frac{\partial L}{\partial\dot{\psi}} - \frac{\partial L}{\partial\psi} + \frac{\partial R}{\partial\dot{\psi}} = 0$$

Substitute terms for the equation of motion:

$$mL\left(\ddot{Y}\cos\psi - \ddot{X}\sin\psi\right) + \ddot{\psi}\left(mL^2 + I_g\right) + b\left(\dot{\psi} - \dot{\theta}\right) = 0$$

$$\therefore \ddot{\psi} = -\frac{mL\left(\ddot{Y}\cos\psi - \ddot{X}\sin\psi\right) + b\left(\dot{\psi} - \dot{\theta}\right)}{mL^2 + I_g}$$

Typically, accelerometers report acceleration values expressed in terms of a coordinate system fixed to the accelerometer. Thus, the values of $\ddot{X}$ and $\ddot{Y}$ (the scalar components of the vector representing the acceleration of O_1 expressed in the O_0 coordinate frame) are not useful inputs in practice. Because this acceleration is merely a vector $\boldsymbol{a} \in \mathbb{R}^2$ expressed in O_0 – that is:

$${}^0\boldsymbol{a} = {}^0a_1{}^0\boldsymbol{x}_0 + {}^0a_2{}^0\boldsymbol{y}_0$$

$$= \begin{bmatrix}{}^0\boldsymbol{x}_0 & {}^0\boldsymbol{y}_0\end{bmatrix}\begin{bmatrix}{}^0a_1 \\ {}^0a_2\end{bmatrix}$$

$$= \begin{bmatrix} 1 & 0 \\ 0 & 1 \end{bmatrix} \begin{bmatrix} {}^0a_1 \\ {}^0a_2 \end{bmatrix} = \begin{bmatrix} {}^0a_1 \\ {}^0a_2 \end{bmatrix} \triangleq \begin{bmatrix} \ddot{X} \\ \ddot{Y} \end{bmatrix}$$

– then we may make use of the coordinate frame transformation to re-express this vector in O_1:

$$\begin{aligned} {}^1\boldsymbol{a} &= \begin{bmatrix} {}^1a_1 \\ {}^1a_2 \end{bmatrix} \triangleq \begin{bmatrix} \ddot{x} \\ \ddot{y} \end{bmatrix} \\ &= {}^0a_1 \, {}^1\boldsymbol{x}_0 + {}^0a_2 \, {}^1\boldsymbol{y}_0 \\ &= [{}^1\boldsymbol{x}_0 \quad {}^1\boldsymbol{y}_0] \begin{bmatrix} {}^0a_1 \\ {}^0a_2 \end{bmatrix} = [{}^1\boldsymbol{x}_0 \quad {}^1\boldsymbol{y}_0] \begin{bmatrix} \ddot{X} \\ \ddot{Y} \end{bmatrix} = {}^0R_1{}^{\mathrm{T}} \begin{bmatrix} \ddot{X} \\ \ddot{Y} \end{bmatrix} \\ &= \begin{bmatrix} \cos\theta & \sin\theta \\ -\sin\theta & \cos\theta \end{bmatrix} \begin{bmatrix} \ddot{X} \\ \ddot{Y} \end{bmatrix} \end{aligned}$$

Thus, we may make the substitutions $\ddot{X} = \ddot{x}\cos\theta - \ddot{y}\sin\theta$ and $\ddot{Y} = \ddot{x}\sin\theta + \ddot{y}\cos\theta$:

$$\ddot{\psi} = -\frac{mL[(\ddot{x}\sin\theta + \ddot{y}\cos\theta)\cos\psi - (\ddot{x}\cos\theta - \ddot{y}\sin\theta)\sin\psi] + b(\dot{\psi} - \dot{\theta})}{mL^2 + I_g}$$

$$= -\frac{mL(\ddot{y}\cos(\psi - \theta) - \ddot{x}\sin(\psi - \theta)) + b(\dot{\psi} - \dot{\theta})}{mL^2 + I_g}$$

Because $\dot{\theta}$ (rotation rate) is typically all that is measured by the IMU, this equation would require estimation of another input variable: θ.

Finally, note that we're often not concerned with the angle of the rotor with respect to an inertial frame; the relative angle is typically more important. Substitute $\psi = \theta + \phi$:

$$\ddot{\phi} = -\frac{mL(\ddot{y}\cos\phi - \ddot{x}\sin\phi) + b\dot{\phi}}{mL^2 + I_g} - \ddot{\theta}$$

so that the equation of motion may be solved for $\phi(t)$ directly. Again, because $\dot{\theta}$ (rotation rate) is typically all that is measured by the IMU, this equation again requires an estimation of an input variable, albeit a different one this time: $\ddot{\theta}$.

The addition of a torsional spring simply adds a restoring torque to the rotational mass that is proportional to the relative angle, ϕ. The zero-torque angle is $\phi = {}^{\pi}/_{2}$ by convention. Thus, the sprung rotor architecture is described by

$$\ddot{\phi} = -\frac{mL(\ddot{y}\cos\phi - \ddot{x}\sin\phi) + b\dot{\phi} + k\left(\phi - \frac{\pi}{2}\right)}{mL^2 + I_g} - \ddot{\theta}$$

with $k = 0$ representing the case of the unsprung eccentric rotor.

APPENDIX B

EXTENDED SWING ARM KINEMATICS

Consider a crude model of arm swing during human locomotion using the kinematics of a driven pendulum, with the resultant excitation at the distal end of the pendulum hereafter referred to as *swing arm* excitation (Figure B-1).

The tangential component of acceleration induced by the swing arm motion is given by:

$$a_t = \dot{v} = \frac{d}{dt}\left(l_{arm}\dot{\theta}\right) = l_{arm}\ddot{\theta} \tag{B-1}$$

where l_{arm} is the length of the swing arm, θ is the angular displacement of the swing arm, and overdots represent differentiation with respect to time. Similarly, the normal component of acceleration induced by the swing arm motion is given by:

$$a_n = \frac{v^2}{l_{arm}} = \frac{\left(l_{arm}\dot{\theta}\right)^2}{l_{arm}} = l_{arm}\dot{\theta}^2 \tag{B-2}$$

Rather than consider a downward gravitational force acting on the eccentric mass

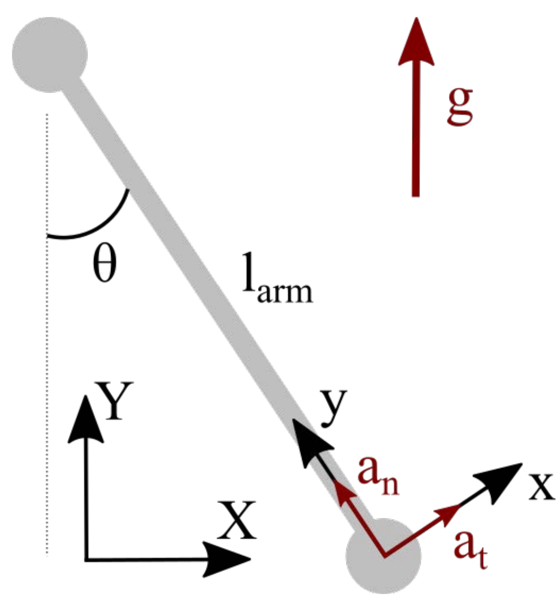

Figure B-1 – Schematic for deriving the kinematics of a driven pendulum directly, instead consider gravity as an effective acceleration of the housing reference frame O_{xy}. For example, at $\theta = \pi/2 = 90°$, the x-component of gravitational acceleration in the housing frame is $g_x = g$ and the y-component is $g_y = 0$. Similarly, when $\theta = 0$, $g_x = 0$ and $g_y = g$. In general:

$$g_x = g \sin\theta \tag{B-3}$$

$$g_y = g \cos\theta \tag{B-4}$$

These gravitational components of acceleration (B-3) and (B-4) sum with (B-1) and (B-2), respectively, to yield the total acceleration of the housing that accounts for gravitational effects. That is:

$$x_{total} = g_x + a_t \tag{B-5}$$

$$y_{total} = g_y + a_n \tag{B-6}$$

A pseudo-walking swing arm signal is derived from the kinematics of a harmonically-driven pendulum. Consider:

$$\theta(t) = \theta_{max} \sin\omega t$$

$$\dot{\theta}(t) = \omega\theta_{max} \cos\omega t \tag{B-7}$$

$$\ddot{\theta}(t) = -\omega^2\theta_{max} \sin\omega t \tag{B-8}$$

where θ_{max} is the amplitude of the swing arm and ω is the driving frequency.

Substitution of (B-1) and (B-3) into (B-5) and subsequent substitution of (B-8) into the result yields:

$$x_{total} = g_x + a_t$$

$$= g \sin\theta + l_{arm}\ddot{\theta}$$

$$= g \sin(\theta_{max} \sin\omega t) + l_{arm}(-\omega^2\theta_{max} \sin\omega t)$$

Similarly, substitution of (B-2) and (B-4) into (B-6) and subsequent substitution of (B-7) into the result yields:

$$y_{total} = g_y + a_n$$

$$= g \cos\theta + l_{arm}\dot{\theta}^2$$

$$= g \cos(\theta_{max} \sin\omega t) + l_{arm}(\omega\theta_{max} \cos\omega t)^2$$

Note that $g, l_{arm}, \theta_{max}, \omega \geq 0$.

B.1 Approximation of Kinematic Functions

Assuming small angles for θ_{max} (noting that $|\sin\omega t| \leq 1$ implies $|\theta_{max} \sin\omega t| \leq \theta_{max}$) allows for dramatic simplification of the expression for total acceleration in the x-direction (Table B-1):

$$x_{total} = g \sin(\theta_{max} \sin\omega t) + l_{arm}(-\omega^2\theta_{max} \sin\omega t)$$

$$\approx g\theta_{max} \sin\omega t - l_{arm}\omega^2\theta_{max} \sin\omega t$$

$$\approx \theta_{max}(g - l_{arm}\omega^2) \sin\omega t \qquad \text{(B-9)}$$

Similarly, the small-angle approximation (Table B-2) can reduce the complexity of

Table B-1 – Error in sine approximation

Angle, $\boldsymbol{\theta_{max}}$	Error in $\mathbf{\sin\theta \approx \theta}$
12.5°	~0.8%
18°	~1.7%
25°	~3.25%

the expression for total acceleration in the y-direction:

$$y_{total} = g\cos(\theta_{max}\sin\omega t) + l_{arm}(\omega\theta_{max}\cos\omega t)^2$$

$$\approx g\left(1 - \frac{\theta_{max}^2\sin^2\omega t}{2}\right) + \theta_{max}^2 l_{arm}\omega^2\cos^2\omega t$$

$$\approx g + \theta_{max}^2 l_{arm}\omega^2 - \theta_{max}^2\left(\frac{g}{2}\sin^2\omega t + l_{arm}\omega^2\sin^2\omega t\right)$$

$$\approx g + \theta_{max}^2 l_{arm}\omega^2 - \theta_{max}^2\left(\frac{g}{2} + l_{arm}\omega^2\right)\sin^2\omega t$$

$$\approx g\left(1 - \frac{\theta_{max}^2}{4}\right) + \frac{\theta_{max}^2 l_{arm}\omega^2}{2} + \frac{\theta_{max}^2}{2}\left(\frac{g}{2} + l_{arm}\omega^2\right)\cos 2\omega t$$

Denoting the average over one swing arm period $2\pi/\omega$ as $\langle\cdot\rangle$, let

$$\bar{y} = g\left(1 - \frac{\theta_{max}^2}{4}\right) + \frac{\theta_{max}^2 l_{arm}\omega^2}{2} \approx \langle y_{total}\rangle$$

Finally, let

$$x = \theta_{max}(l_{arm}\omega^2 - g)$$

$$y = \theta_{max}^2\left(\frac{g}{2} + l_{arm}\omega^2\right)$$

Then the approximate acceleration functions $a_x(t)$ and $a_y(t)$ for swing arm excitation may be expressed compactly as

$$a_x(t) \approx -x\sin\omega t$$

$$a_y(t) \approx \bar{y} + y\cos 2\omega t$$

Table B-2 – Error in cosine approximation

Angle, $\boldsymbol{\theta_{max}}$	Error in $\boldsymbol{\cos\theta \approx 1 - \theta^2/2}$
12.5°	<<0.01%
18°	~0.04%
25°	~0.2%

APPENDIX C

ERROR CONVERGENCE STUDY

A convergence study to determine the independence of a numerical solution from solver settings is advisable to ensure that the solver settings do not result in avoidable solution error. Additionally, a convergence study is useful for determining the largest tolerances that may be used by the solver that still result in acceptable solutions, and is thus useful in reducing solver computational overhead.

Following the poor subject-to-subject simulation results for the unsprung rotor presented in Chapter 3, a particular interest was developed in determining the correct Ordinary Differential Equations (ODE) solver tolerances – specified by a relative tolerance value and an absolute tolerance value – to be used when real human subject walking excitation data were used as input to the unsprung eccentric rotor model.

Two versions of the eccentric rotor model were used in the convergence study: the ψ ODE (2-2) and the ϕ ODE (2-3), which require different approaches to estimate the θ model input from the human subject walking excitation data. The values used for the relative tolerance were varied from 10^{-3} to 10^{-5}, and the values used for the absolute tolerance were varied from 10^{-6} to 10^{-8} in tandem. Thirty input signals recorded from 10 subjects walking on a treadmill at the three test belt speeds of 2.5, 3.5, and 5.5 mph were used as input to the models for the study. Error is computed from the simulated power output by using the measured prototype power output over the length of the test as the standard. The results using the parameters for the second-generation unsprung prototype are presented in Figures C-1 through C-3.

The results indicate that the ψ ODE and the ϕ ODE produce a similar degree of error. Additionally, the results show that the most stringent solver tolerances produce no better results than the least stringent solver tolerances. Consequentially, it is unlikely that

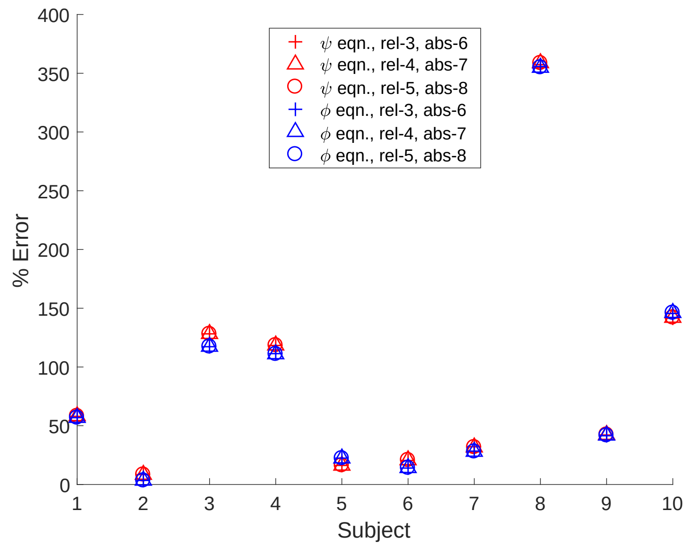

Figure C-1 – Error vs. subject for 2.5 mph treadmill belt speed

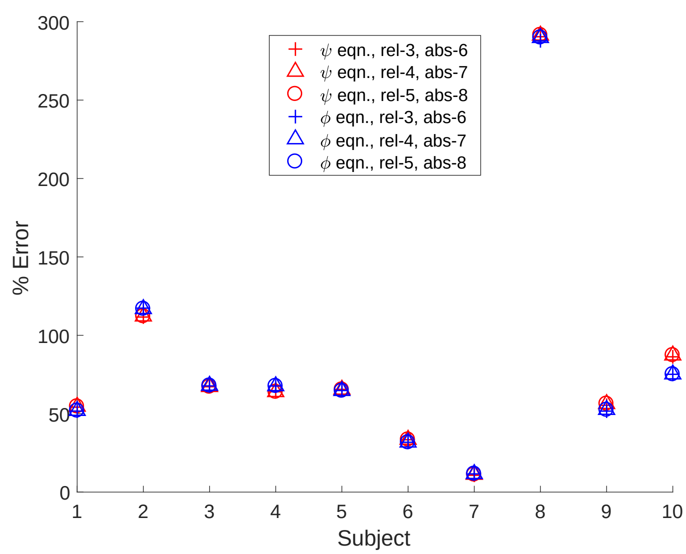

Figure C-2 – Error vs. subject for 3.5 mph treadmill belt speed

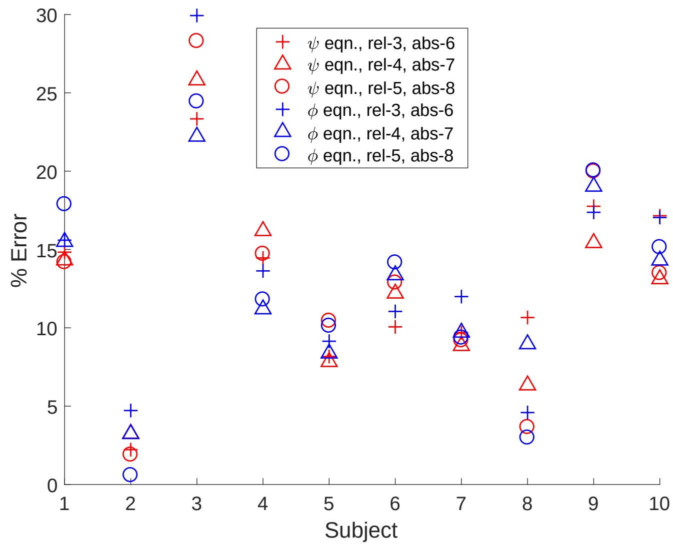

Figure C-3 – Error vs. subject for 5.5 mph treadmill belt speed

the choice of solver tolerances is the cause of the error observed in the unsprung eccentric rotor simulations using real human subject input presented in Chapter 3.

APPENDIX D

METAHEURISTIC OPTIMIZATION OF

UNSPRUNG ECCENTRIC ROTOR

The purpose of the linearization used in Chapter 4 is to produce models that aid in the choice of design parameters for an eccentric rotor harvester; it is thus the local optima of the dimensionless power Π that are of primary concern. However, the linearized system and its contingent dimensionless power result are highly simplified models of the nonlinear system under consideration. It is therefore expected that the maximizers of power output for the linearized and nonlinear systems will differ; exactly how the maximizers differ and possible reasons as to why are the focus of this section. The output from this exploratory work eventually motivated the nonlinear dynamical analysis presented in Chapter 4.

In order to determine the local optima of the dimensionless power output using the nonlinear dynamics, a numerical optimization scheme was formulated. An objective function was formed that takes in the design parameters β_e, Ω, and λ, as well as the mechanical damping β_m, and the excitation A_x, A_y, and θ_{max}. A numerical differential equations solver – MATLAB's *ode45* function with enhanced error tolerances – is called using the aforementioned inputs in order to output a numerical solution, ${\gamma_n}'(\tau)$, which is assumed to be periodic with period $2\pi/\Omega$. It should be noted that making this assumption is unwise, due to the presence of the subharmonic resonance peak. To limit computational demand, 20 cycles of period $2\pi/\Omega$ are simulated numerically and only the last period of the solution is retained; the portion of the solution derivative over this final period is treated as $\gamma'(\tau)$ for substitution into the power equation with $\tau_0 = 2\pi/\Omega$. Numerical integration of the power equation then yields an estimate for the dimensionless power output, Π, for the nonlinear system, which is returned as the output of the objective function. As the output of the objective function is found using numerical integration, it is expected to be nonsmooth, motivating the choice of a metaheuristic direct search – specifically, MATLAB's *patternsearch* function – as the optimization algorithm for finding the local maxima.

The six excitations used in Chapter 4, as well as the three mechanical damping values $\beta_m = 0$ (*no mechanical damping*), $\beta_m = 0.01$ (*typical mechanical damping*), and $\beta_m = 0.1$ (*high mechanical damping*), were used to create 18 different optimization problems seeking the optimal design parameters β_e, Ω, and λ subject to the bounds $\beta_e, \Omega \geq 0$ and $0 \leq \lambda \leq 1$. For each problem, a grid of 1000 evenly spaced initial points within the region $0 < \beta_e \leq 0.5$, $0 < \Omega \leq 2$, and $0 < \lambda \leq 1$ were used to solve each problem for a collection of 1000 maximizers per problem. The optimization was run using parallel processing in MATLAB R2018b on a 3.3GHz six-core processor machine with 32GB of RAM and took approximately 200 hours to complete all 18 sets of damping and excitation parameters.

D.1 Optimization Results

As predicted by the power output of the linearized system, the vast majority of the 1000 initial points approached the infinite power solution as $\beta_e, \Omega \to \infty$. The largest value that could be represented on the machine used for optimization using conventional floating-point values was approximately $1.8 \cdot 10^{308}$; when the objective function exceeded this value, the output is represented in MATLAB by the special value "Inf," at which point the optimization algorithm terminates with a successful exit flag. As local optima are of greater concern in this analysis, these points were separated from the maximizers with finite objective function outputs.

All maximizers attained the upper bound on λ, providing computational support for the conclusion that $\lambda^{\star} = 1$, even in the case of nonlinear rotor dynamics. Thus, only the remaining design parameters β_e and Ω need be considered to identify a particular maximizer; consequently, this makes representing the maximizers as points on an Ω vs. β_e plot convenient for visualizing the optimization results – see Figures D-1 through D-4 for a graphical summary of the maximizers plotted over the contours of the dimensionless power for the linearized system with corresponding mechanical damping and excitation input.

It is worth noting that there were almost no differences between the maximizers for systems with no mechanical damping ($\beta_e = 0$) and typical mechanical damping ($\beta_m = 0.01$). For high mechanical damping ($\beta_m = 0.1$), local maxima with finite objective function value were found only for EX6 – a peak predicted by the linearized power output – and these results are summarized in Figure D-4.

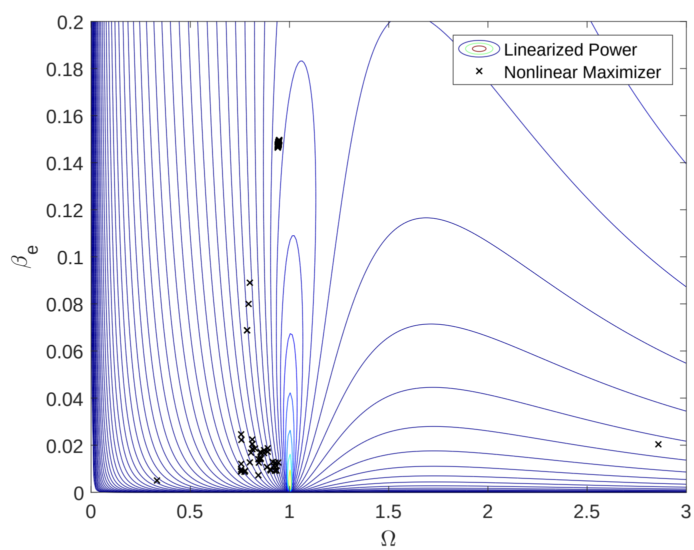

Figure D-1 – Summary of maximizers for EX2 and no mechanical damping ($\beta_m = 0$). This result is nearly identical to that of typical mechanical damping ($\beta_m = 0.01$) as well as EX2 with either no or typical mechanical damping (not shown).

Figure D-1 summarizes the results of optimization for no mechanical damping and excitation EX2. The majority of maximizers are clustered near the *linear* or *primary resonance peak* at $\Omega \approx 1$ and fall along a set that extends to high levels of electrical damping. Maximizers for higher electrical damping are closer to $\Omega = 1$ than their lower electrical damping counterparts. There are additional, albeit very few, maximizers at the *low-frequency peak* near $\Omega \approx 1/3$ and the *high-frequency peak* near $\Omega \approx 2.9$ – peaks, possibly due to resonance, that are not predicted by the linearized system. The results for EX2 with no mechanical damping and typical mechanical damping, as well as EX1 with typical mechanical damping, are very similar to that of the results presented in Figure D-1, and are thus not shown; there are, however, some important differences. The additional maximizers at the low- and high-frequency peaks do not appear in the results for excitations EX1 and EX2 with typical mechanical damping, and only a single maximizer at the low-frequency peak appears with excitation EX1 with no mechanical damping. Furthermore, the maximizers in the typical mechanical damping cases are more tightly clustered near $\Omega \approx 1$, falling along a set that more closely resembles a curve instead of into clusters spread in the Ω-dimension.

The optimization results for excitation EX3 with typical mechanical damping are presented in Figure D-2, and are nearly identical to that of EX3 with no mechanical damping, except that the maximizers are more tightly clustered with greater mechanical damping. The results for excitation EX3 show some important differences between the results for excitations EX1 and EX2, namely, the disappearance of the maximizer at the low-frequency peak, no maximizers with $\beta_e > 0.04$, and more maximizers clustered at the high-frequency peak, this time centered at $\Omega \approx 2.7$.

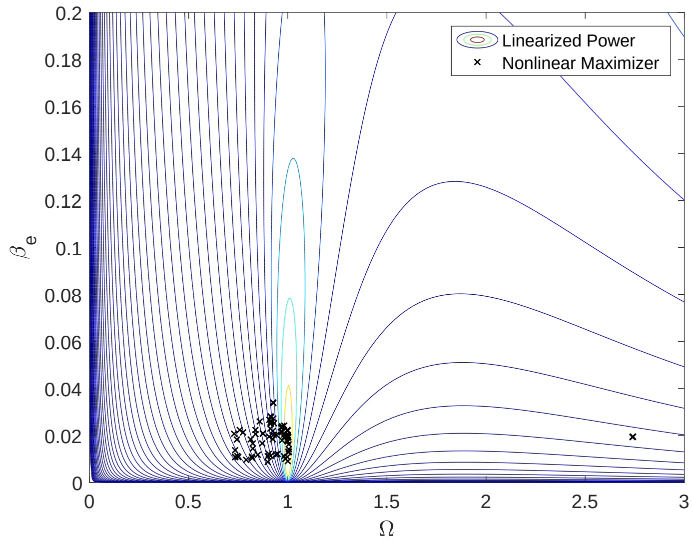

Figure D-2 – Summary of maximizers for EX3 and typical mechanical damping. This result is nearly identical to that of EX3 with no damping (not shown).

The optimization results for excitation EX6 with typical mechanical damping are presented in Figure D-3. The maximizers in the case are heavily concentrated at both the linear resonance and high-frequency peaks, with several maximizers also found at the low-frequency peak. The maximizers for the high-frequency peak now cluster mostly around $\Omega \approx 2.2$, which is lower than with excitations EX1-EX3. Figure D-3 also shows a large spread of the maximizers in both the Ω- and β_e-dimensions. The results of the optimization for excitation EX6 with typical mechanical damping are very similar to the results with no mechanical damping, and these are also similar to the results for excitations EX4 and EX5 (all of which all share the same swing arm amplitude, θ_{max}) with typical and no mechanical damping; there are, however, some important differences. As with the results for excitations EX1-EX3, higher mechanical damping yields more tightly packed clusters of maximizers in the Ω-dimension; lower excitation frequency also produces the same result.

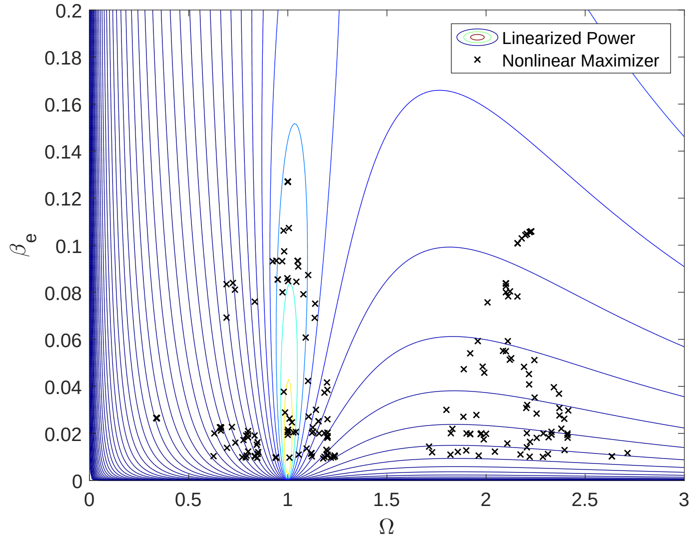

Figure D-3 – Summary of maximizers for EX6 and typical mechanical damping. The results for EX4, EX5, and EX6 for both zero and typical mechanical damping are very similar.

Excitations EX4-EX6 also show a decrease in the number of large β_e maximizers as the excitation frequency becomes smaller, which appears to be the opposite trend observed for excitations EX1-EX3.

Finally, Figure D-4 presents the results for the high mechanical damping case. Only EX6 produced maximizers with finite objective function value; all other excitations only produced maximizers as $\beta_e, \Omega \rightarrow \infty$. The primary resonance peak is predicted by the linearized system, although primary resonance peaks with a local maximum were also predicted for EX2 and EX3. Being that the linearized system overpredicts the dimensionless power output near the primary resonance, this could constitute a difference between the linearized and nonlinear systems. As with other excitations with high swing arm amplitude, maximizers appear at the high-frequency peak in Figure D-4, clustering primarily around $\Omega \approx 2.3$.

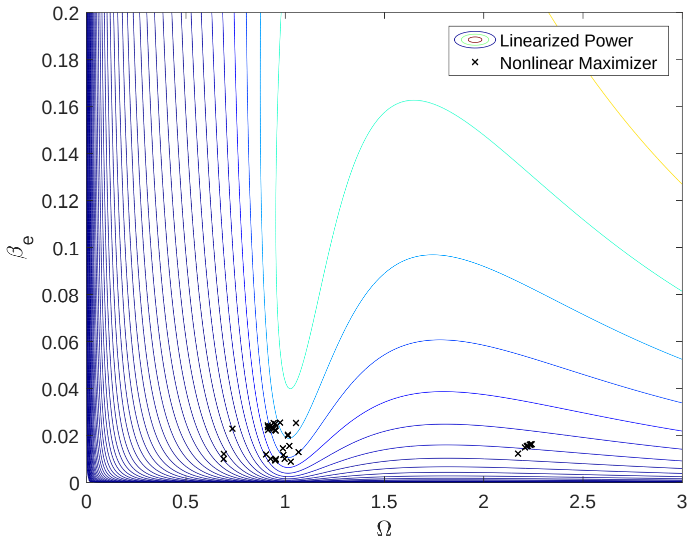

Figure D-4 – Summary of maximizers for EX6 with high ($\beta_e = 0.1$) mechanical damping. No maxima with finite objective function output were found for any other excitation.

The findings of the optimization results across all of the mechanical damping and excitation parameter sets may be summarized as follows:

- For sufficiently low levels of mechanical damping, the maximizers cluster around three high-power peaks: one at $\Omega \approx 1/3$, one near the linear resonance at $\Omega \approx 1$, and one somewhere between $\Omega \approx 2$ and $\Omega \approx 3$.
- Results differ qualitatively more across different swing arm amplitudes than across swing arm frequency.
- For the high-amplitude swing arm input (EX4-EX6), higher frequency excitation produces more maximizers at higher electrical damping. The opposite seems to be true for the low-amplitude swing arm inputs (EX1-EX3).
- The linear resonance peak overpredicts the nonlinear primary resonance peak, and nonlinear resonance occurs to the left of $\Omega \approx 1$.

- Maximizers are more closely clustered in the Ω-dimension for less energetic excitations and when more damping is present, and are more spread when excitations are energetic and less damping is present.

The last point in the above summary suggests that part of the reason for the spreading of the maximizers in the Ω-dimension could be transient effects; study of individual solutions using the design values for various maximizers appears to confirm this hypothesis, as several design points result in solutions that are not periodic at the end of the time period over which the solutions were integrated. Neighboring points sometimes achieve periodic behavior, resulting in many local maxima at the peak values of Ω. Recall that 20 cycles of period $2\pi/\Omega$ was selected as the length of time over which solutions were numerically integrated in order to limit computational demand; this arbitrarily-chosen integration timespan is not sufficient for many of the solutions to become periodic. Assuming chaos (long-term aperiodic behavior) is not the reason for the lack of convergence to periodicity, increasing the number of cycles over which the numerical solutions are integrated should reduce the disparities in Ω values of the maximizers.

For computational support of this hypothesis, consider the maximizers with finite objective function output for excitation EX6 and typical mechanical damping presented in Figure D-5; this represents the optimization problem with some of the least tight clustering of maximizers. The maximizers from this problem were used as initial points in a new problem with identical mechanical damping and excitation, but with a solution time span of 200 cycles of period $2\pi/\Omega$. The results are summarized in Figure D-5, showing much tighter clustering of maximizers, as expected.

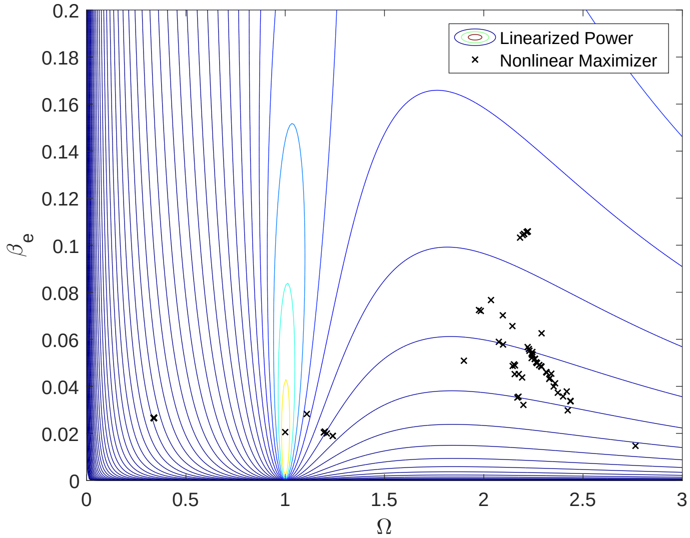

Figure D-5 – Summary of results for EX6 with typical mechanical damping, run using 200 swing arm cycles.

APPENDIX E

ALTERNATIVE NONDIMENSIONALIZATION

Consider the planar model for an unsprung eccentric rotor harvester

$$\ddot{\gamma} + \frac{b_e + b_m}{ml^2 + I_g}\dot{\gamma} + \frac{a_x(t)}{l_{eff}}\cos\gamma + \frac{a_y(t)}{l_{eff}}\sin\gamma + \ddot{\theta}(t) = 0 \tag{E-1}$$

where γ is the displacement of the eccentric rotor relative to the harvester housing coordinate frame as measured from the $-\boldsymbol{y}$ basis vector, b_e and b_m are the electrical and mechanical linear viscous damping coefficients, respectively, m is the mass of the rotor, l is the distance from the rotating center to the rotor's center of gravity, I_g is the inertia of the rotor about its center of gravity, l_{eff} is the effective length, defined as $l_{eff} = \left(ml^2 + I_g\right)/ml$, $a_x(t)$ and $a_y(t)$ are the input linear accelerations of the harvester housing (which typically include gravitational acceleration) in the x and y directions, respectively, $\ddot{\theta}(t)$ is the input angular acceleration of the housing, and overdots represent differentiation with respect to time.

Additionally, consider the approximate excitation imposed on a harvester (E-1) mounted on the distal end of a driven pendulum acting in a gravitational field, with gravity acting as an effective acceleration of the harvester frame of reference:

$$\begin{aligned}\ddot{\gamma} &+ \frac{b_e + b_m}{ml^2 + I_g}\dot{\gamma} + \frac{1}{l_{eff}}\left[\theta_{max}(g - l_{arm}\omega^2)\sin\omega t\right]\cos\gamma \\ &+ \frac{1}{l_{eff}}\left[g\left(1 - \frac{\theta_{max}^2}{4}\right) + \frac{\theta_{max}^2 l_{arm}\omega^2}{2}\right. \\ &\left. + \theta_{max}^2\left(\frac{g}{2} + l_{arm}\omega^2\right)\cos 2\omega t\right]\sin\gamma = \omega^2\theta_{max}\sin\omega t\end{aligned} \tag{E-2}$$

Let $\omega_0 = \sqrt{g/l_{arm}}$ be the natural frequency of the swing arm. Then (E-2) may be nondimensionalized by the introduction of the following normalized variables: time $\tau =$

$\omega_0 t$, electrical damping $\beta_e = b_e/\left(2\omega_0\left(ml^2 + I_g\right)\right)$, mechanical damping $\beta_m = b_m/\left(2\omega_0\left(ml^2 + I_g\right)\right)$, excitation frequency $\Omega = \omega/\omega_0$, effective length $\lambda_1 = l_{eff}/l_{arm}$. Equation (E-2) may now be written as

$$\gamma'' + 2(\beta_e + \beta_m)\gamma' + \frac{\theta_{max}}{\lambda_1}(1 - \Omega^2)\sin\Omega\tau\cos\gamma$$
$$+ \frac{\theta_{max}^2}{\lambda_1}\left[\frac{1}{2}\left(\Omega^2 - \frac{1}{2}\right) + \left(\Omega^2 + \frac{1}{2}\right)\cos 2\omega t\right]\sin\gamma + \frac{1}{\lambda_1}\sin\gamma \tag{E-3}$$
$$= \omega^2\theta_{max}\sin\omega t$$

Thus, what started as an equation with independent variable t, five harvester parameters m, l, I_g, b_e, b_m, and four excitation parameters θ_{max}, ω, g, and l_{arm} has been reduced to the equivalent, dimensionless equation with independent variable τ, three harvester parameters λ_1, β_e, and β_m, and two excitation parameters θ_{max} and Ω. One may be concerned, then, that the choice of nondimensionalization in Chapter 4 is suboptimal; that choice also yields three harvester parameters Ω, β_e, and β_m, but *three* excitation parameters, θ_{max}, A_x, and A_y. This is a valid concern; however, the choice to use the latter nondimensionalization was motivated by the following observations:

- Choosing to scale (E-1) by the natural frequency of the driven pendulum is unusual, and will likely result in solution derivatives γ' and γ'' achieving values that are not close to unity.
- The excitation parameter l_{arm} is selected as the scaling factor in the definition of the dimensionless effective length λ_1 because it is the only available parameter (in the sense that it is not a design parameter to be

determined) with dimension of length. As l_{arm} is an arbitrary length, the optimal values of λ_1 will likely not be especially meaningful.

- Evaluating the values of the linear acceleration amplitudes A_x and A_y is useful in determining to what extent each acceleration direction contributes input to the harvester system.
- Reducing the number of excitation parameters doesn't yield many benefits computationally. The excitation is fixed before numerical solutions are computed, and evaluating the value of an additional excitation parameter results in a negligible amount of computational overhead.

However, it should be noted that treatment of (E-3) has been perfunctory, and it is quite possible that the scale used to derive (E-3) better provides insights into rotor behavior than the scale used for the work presented in Chapter 4.

APPENDIX F

SURVEY OF VIBRATION SIGNALS

DE GRUYTER Energy Harvesting and Systems 2017; 4(2): 67–76

Robert Rantz* and Shad Roundy

Characterization of Real-world Vibration Sources and Application to Nonlinear Vibration Energy Harvesters

DOI 10.1515/ehs-2016-0021

Abstract: A tremendous amount of research has been performed on the design and analysis of vibration energy harvester architectures with the goal of optimizing power output. Often, little attention is given to the actual characteristics of common vibrations from which energy is harvested. In order to shed light on the characteristics of common ambient vibration, data representing 333 vibration signals were downloaded from the NiPS Laboratory "Real Vibration" database, processed, and categorized according to the source of the signal (e. g. vehicle, machine, etc.), the number of dominant frequencies, the nature of the dominant frequencies (e. g. stationary, band-limited noise, etc.), and other metrics. By categorizing signals in this way, the set of idealized vibration inputs (i. e. single stationary frequency, Gaussian white noise, etc.) commonly assumed for harvester input can be corroborated and refined. Furthermore, some heretofore overlooked vibration input types are given motivation for investigation. The classification determined that, of the set of signals used in the study, 64 % of the animal source signals are best described with nonstationary dominant frequencies, 58 % of machine source signals are best described with stationary frequencies, and vehicle source signals are poorly described by any one signal type used in the classification. Nonlinear harvesters with a cubic stiffness term have received extensive attention in the scholarly literature; a numerical simulation and optimization procedure were performed using several representative signals as vibration inputs to determine the prevalence with which such a nonlinear harvester architecture might provide improvement to power output. The analysis indicated that a nonlinear harvester architecture may prove beneficial in increasing power output over a linear counterpart if the signal contains a single, dominant frequency that is not stationary in time, as evidenced by a 14 % increase in harvester power output when employing an architecture with a nonlinear cubic stiffness function. Other studies have indicated that nonlinear architectures may be beneficial for signals with nonstationary frequencies or filtered noise. 53 % of the all characterized signals fall into categories that could potentially benefit from a nonlinear oscillator architecture.

Keywords: energy harvesting, nonlinear harvesters, optimal architectures, vibration classification, vibration database

***Corresponding author: Robert Rantz,** Department of Mechanical Engineering, University of Utah, 1495 E 100 S, Salt Lake City, UT 84112, USA, E-mail: robert.rantz@utah.edu
Shad Roundy, Department of Mechanical Engineering, University of Utah, 1495 E 100 S, Salt Lake City, UT 84112, USA

Introduction

In order to extract sufficient power for a given application, vibration energy harvesters (VEHs) are typically high Q (10-100) resonant oscillators. Thus, their operating bandwidth can be quite narrow. This has motivated an extraordinary amount of research work on methods to increase the operating bandwidth of VEHs (Daqaq et al. 2014; Neiss et al. 2014; Roundy et al. 2005; Wu et al. 2013; Zine-El-Abidine and Yang 2009). Such methods include multi-mode dynamic structures, active frequency tuning by both mechanical and electrical means, and nonlinear dynamic structures. Of course, if the vibration source is dominated by a single stationary frequency, a linear oscillator-based energy harvester is the optimal energy harvesting structure (Halvorsen et al. 2013; Heit and Roundy 2015; Mitcheson et al. 2008; Williams, Woods, and Yates 1996).

In the search for methods to improve the operating bandwidth of VEHs, careful examination and quantification of the types of vibrations that appear frequently in environments conducive to energy harvesting often become a secondary priority; to our knowledge, there has not been a systematic study of the prevalence of vibration sources geared towards determining which VEH structure would be most appropriate for a given source.

The current study seeks to provide additional insight into the prevalence and characteristics of vibrations commonly encountered in the environment. A broad range of vibrations from the existing NiPS Laboratory "Real Vibration" database is classified using metrics that capture vibration properties that are relevant to VEH design. A comparative analysis of two types of energy harvesting architectures – linear, and nonlinear with a cubic stiffness function – is performed on several representative signals in order to quantify the degree to which a nonlinear architecture could improve power output over a linear architecture, if at all.

Methodology for Classifying Vibrations

The NiPS Laboratory "Real Vibration" database is a library of downloadable vibration signals collected from several types of acquisition kits (Neri et al. 2012). Each signal in the database consists of 3 axes of vibrational data; linear acceleration of X, Y and Z, measured in units of g. Each of the 3 axes is treated as an independent signal for processing purposes. DC bias was removed from each signal axis by subtracting the mean value from the data.

A classification system has been developed for the study that has been previously published (Rantz and Roundy 2016) and is only briefly summarized here.

Signal Sources

The "source" classification of a signal is a broad categorization of what kind of system produced the vibration, as determined by the signal metadata. Source classifications include *Animal, Machine, Vehicle, Structure*, or in the case that the source of the vibration cannot be surmised with confidence, *Unknown*.

Spectrogram Parameters

The entire NiPS database of vibration signals was downloaded and processed into spectrograms for each of the 3 axes, using several sets of processing parameters, generating several spectrograms per vibration signal.

In order to make dominant signals more apparent, a filtering technique was employed based in linear VEH theory. According to the Velocity Damped Resonant Generator (VDRG) model (Mitcheson et al. 2004), the upper bound on average power output of a linear VEH subject to harmonic excitation at resonance is:

$$P_{avg} = \frac{A^2 m \zeta_e}{4\omega(\zeta_m + \zeta_e)^2} \quad (1)$$

where A is the input acceleration amplitude, m is the seismic mass, ζ_m is the mechanical damping ratio, and ζ_e is the electrical damping ratio. (Mitcheson et al. 2004).

Notice that the leading terms A^2 and ω in (1) are properties of the input alone. Determining dominant frequencies is a major component of the classification system presented in this study; thus, in order to make classification more straightforward, spectrograms filtered by only plotting frequency content that is greater than ½ the maximum value of A^2/ω in each FFT frame were plotted alongside unfiltered spectrograms. This filtering process made "dominant" frequencies more distinct, resulting in easier classification of the signal. See Figure 1 for an example spectrogram. Refer to (Rantz and Roundy 2016) for more information on the spectrogram generation procedure and subsequent signal classification.

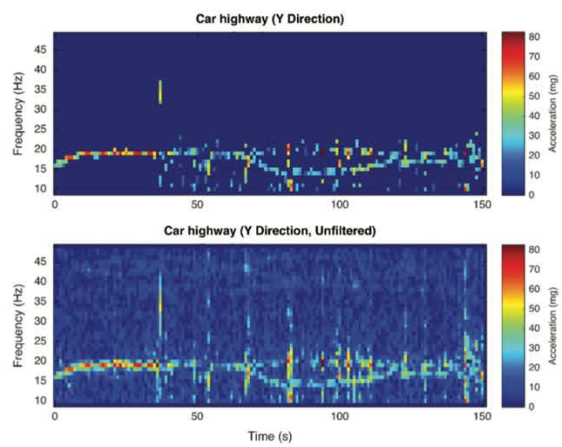

Figure 1: Filtered (top) and unfiltered (bottom) spectrogram used for classification.

Signals with Distinct Dominant Frequencies

Knowledge of the frequencies at which the input power is concentrated has major implications in the design of a VEH architecture, and is therefore of critical importance in any classification scheme intended to shed light on the kinds of vibrations that could be encountered by VEHs.

A *dominant frequency* in the context of this study is a distinct frequency in the signal spectrogram at which the value of A^2/ω is large relative to other frequencies that persists for a substantial duration of the signal.

Vibration signals may have zero, one, or more dominant frequencies. Note that the term *dominant frequency* is derived from the degree to which a particular frequency dominates (in terms of A^2/ω value) a single FFT window, and is thus somewhat of a misnomer; a dominant frequency need not remain at a single frequency throughout the length of the spectrogram.

The time-varying behavior of the dominant frequencies throughout the duration of the signal is also used for classifying the signal. A dominant frequency is considered *stationary* if the frequency at which it occurs does not change much during the length of an input signal. It is possible for some, all, or none of the dominant frequencies of a signal to be stationary.

Signals without Distinct Dominant Frequencies

Many vibration signals do not have distinct, dominant frequencies. Many of these signals can be best described as white noise and filtered noise. For simplicity of classification, two classifiers were employed in this study to describe signals without distinct, dominant frequencies: *White Noise* and *Filtered Noise*.

Amplitude and Noise Tags

Vibrations with inconsistent acceleration amplitudes present unique challenges to nonlinear VEH designs, where both the amplitude and frequency of an input vibration have the capacity to dramatically affect the power output. In order to catalog vibrations with significant swings in amplitude without creating another classification dimension, an *amplitude tag* is applied to all vibrations that change at least (an arbitrarily selected) 50 % over the length of the signal.

Classification Methodology

The entire NiPS database of signals was first downloaded, along with the signal metadata, by virtue of an automated script; at the time of execution, the script downloaded a total of 329 different signals, each with X, Y and Z channels. Spectrograms were then generated for each axis of the signal. The signals, with their associated metadata and spectrograms, were then manually inspected. Signals that did not meet minimum quality criteria were discarded. This process removed 218 signals, leaving 111 left for the study. The classification of each spectrogram was performed manually, by visual inspection of both the spectrogram image file, as well as the (interactive) MATLAB-FIG file.

Vibration Classification Results

Breakdown of Signals by Source

A total of 333 spectrograms were analyzed for the study. A breakdown of all signals by source classification is presented in Figure 2.

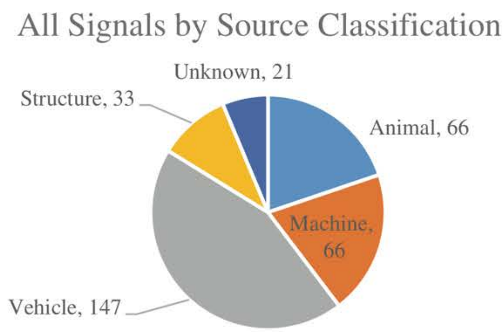

Figure 2: All 333 signals from the study, sorted by source classification.

Breakdown of Signals by Spectrogram Classification

A breakdown of all signals by spectrogram classification is presented in Figure 3.

Most of the signals analyzed in the study can be classified as having a single, dominant frequency. Over a quarter of the total signals can be characterized as lacking a dominant frequency, and are better described by either the White Noise or Filtered Noise categories. A relatively small number of the signals could be classified as having more than one distinct, dominant frequency.

Breakdown of Individual Source Classifications

Perhaps the most important results concern how the signals were characterized for each source. Figure 4 shows the breakdown of characterizations for the Animal sources analyzed in the study.

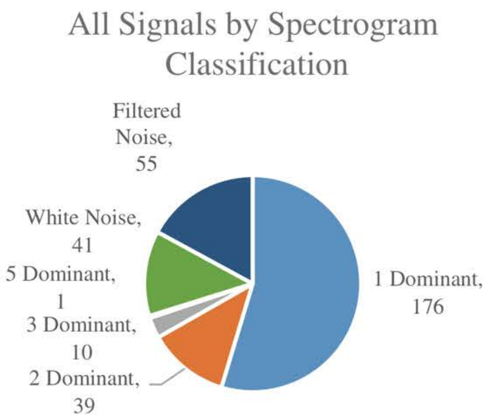

Figure 3: All 333 signals from the study, sorted by spectrogram classification.

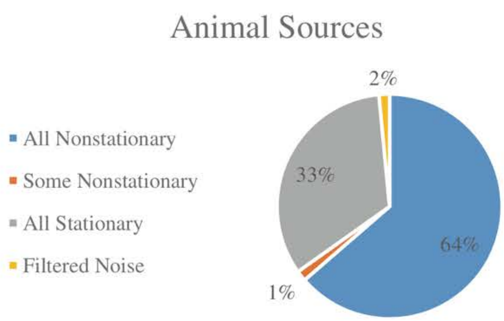

Figure 4: Breakdown of animal sources.

The majority of Animal signals can be described as having dominant frequencies that are nonstationary.

Figure 5 shows the breakdown of characterizations for Machine sources. In this case, the vast majority of signals exhibit either stationary frequencies or are best characterized as noise.

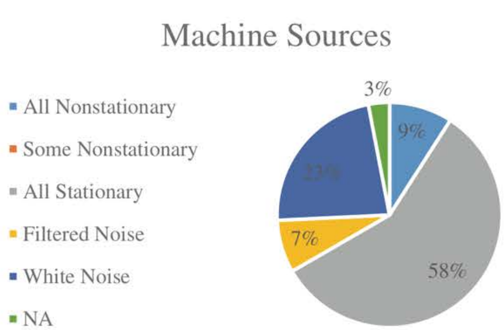

Figure 5: Breakdown of Machine sources.

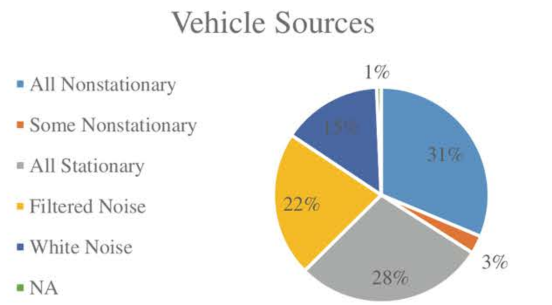

Figure 6: Breakdown of vehicle sources.

Figure 6 shows the breakdown of characterizations for Vehicle sources. Vehicle sources have the most variability in their characterizations; no single category dominates over the others. Dominant frequencies constitute the largest combined category, making up 62 % of the classifications. The largest single category is "All Nonstationary," consuming 31 % of the total characterizations. This is, perhaps, no surprise; as a vehicle accelerates and decelerates, it is reasonable to assume that the vibrational characteristics will vary with time. "All Stationary" is the second largest category. This may be explained by steady-state vehicle motion; a car moving at constant speed on a highway, for example, may not have any vibrational characteristics that change over the length of the signal.

Figure 7 shows the breakdown of characterizations for Structure sources. For this analysis, a "structure" relates to infrastructure items such as bridges, highways, and buildings. The majority (64 %) of the signals derived from Structure sources can best be described as "noisy."

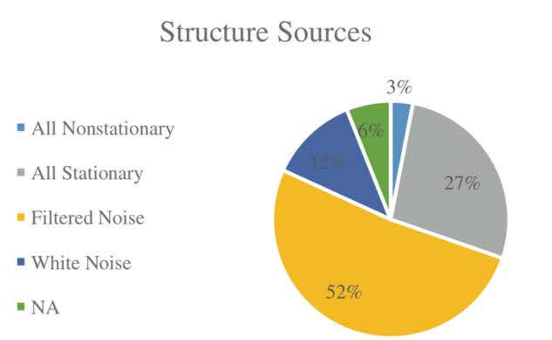

Figure 7: Breakdown of structure sources.

Amplitude Tag

Recall that another important piece of information relevant to VEH design is the time dependence of the vibration amplitude, and that this information is conveyed in this study by virtue of an *amplitude tag*. The amplitude tag can be applied to all classifiable signals; that is, signals not classified as "NA."

Figure 8 displays the frequency with which the amplitude tag was applied to signals, sorted by source classification. It is very clear that time-dependence of vibration amplitude is common in real-world vibration signals, regardless of source.

Method for Comparing Linear and Nonlinear Harvester Architectures

Two vibration energy harvester architectures – one linear, and one with a nonlinear cubic stiffness function – were compared using six representative input signals in order to determine the degree to which the introduction of nonlinearity improves power output, if at all.

The power extracted from the harvester via the electromechanical transducer is assumed to act as an ideal linear damper, as in the VDRG model (Mitcheson et al. 2004). The harvester architectures under consideration may all be described by:

$$m\ddot{z} + (b_m + b_e)\dot{z} + f_s(z) = -\ddot{y} \tag{2}$$

where z is the relative displacement between the base of the harvester and the harvester seismic mass, m is the seismic mass, b_m is the mechanical vicious damping coefficient representing mechanical losses, b_e is the electrical damping coefficient representing the damping imposed by the power transduction mechanism, $f_s(z)$ is the restorative force, and y is the displacement of the base; consequentially, the term y represents the input vibration described by an acceleration signal. A schematic of the system model described by eq. (2) can be found in Figure 9

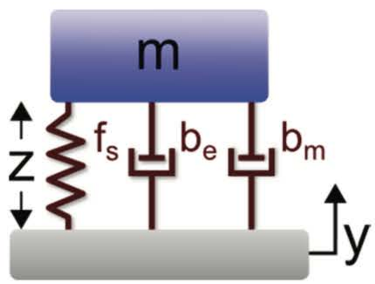

Figure 9: A schematic of the system model described by (2).

In the case of a linear harvester, the restorative force is proportional to displacement:

$$f_s(z) = kz \tag{3}$$

where k is the linear spring constant. Equation (3) in conjunction with eq. (2) represent the VDRG model (Mitcheson et al. 2004). A cubic stiffness function is employed for the nonlinear harvester architecture:

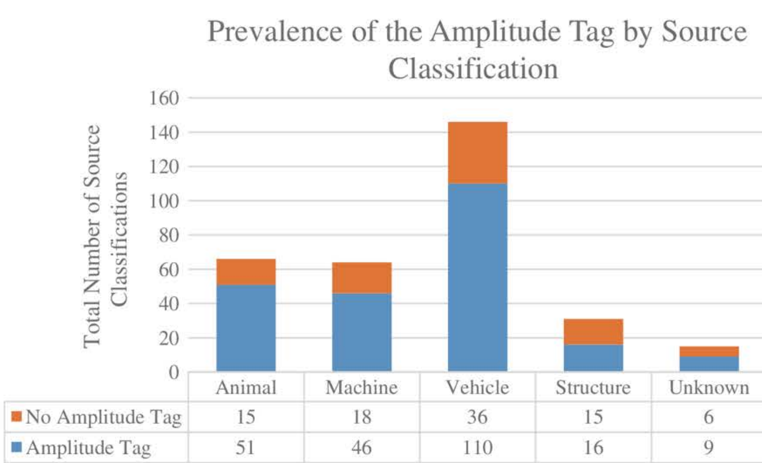

	Animal	Machine	Vehicle	Structure	Unknown
No Amplitude Tag	15	18	36	15	6
Amplitude Tag	51	46	110	16	9

Figure 8: Prevalence of the amplitude tag, broken down by source classification.

$$f_s(z) = \beta z + \alpha z^3 \quad (4)$$

where β is the linear stiffness coefficient, and α is the cubic stiffness coefficient. When the stiffness function described in eq. (4) is substituted into eq. (2), this becomes the familiar Duffing oscillator excited by the input vibration $-\ddot{y}$. When posed in this form, equation eq. (4) conveniently encapsulates a range of qualitatively different nonlinear architectures (Daqaq et al. 2014). If $\beta > 0, \alpha = 0$, then eq. (4) reduces to eq. (3); that is, the restorative force is linear. If $\beta \geq 0, \alpha > 0$ $(\alpha < 0)$, the restorative force can be viewed as a hardening (softening) spring. Finally, if $\beta < 0, \alpha > 0$, the resultant system is bistable in nature, characterized by two potential energy wells corresponding to two stable equilibria separated by a potential barrier.

In order to approximate a ceiling on the power that a harvester architecture could achieve, optimization must be performed on the system parameters with the goal of maximizing power dissipation through the electrical damper for a given input signal. The seismic mass, m, and the mechanical damping, b_m. from eq. (2) were considered to be fixed parameters for both linear and nonlinear architectures with values of 1 and 0.02, respectively. The electrical damping, b_e, was an optimization parameter for both architectures.

For the linear architecture exhibiting a stiffness function described by eq. (3), the only additional parameter over which optimization was performed was k, the linear stiffness coefficient. Thus, candidate solutions for the optimization of the linear harvester architecture were two-dimensional, consisting of an electrical damping value, b_e, and a stiffness value, k.

For the nonlinear architecture exhibiting a stiffness function described by eq. (4), two additional optimization parameters were introduced: β, the linear stiffness coefficient, and α the cubic stiffness coefficient. Thus, candidate solutions for the optimization of the nonlinear harvester architecture were three-dimensional, consisting of an electrical damping value, b_e, a linear stiffness coefficient, β, and a cubic stiffness coefficient, α.

An objective function was formed relating the relevant harvester optimization parameters to the power output of the harvester subject to a particular input signal. The relevant design parameters were the input to the objective function; these parameters were used to populate the values in the differential equation that describes the system in eq. (2) and a numerical solver was used to compute the relative motion of the seismic mass in response to the signal input. Having solved for the relative velocity of the mass over the length of the signal T, the power dissipated in the electrical damper was computed via numerical estimation of $P_{avg} = b_e \int_0^T \dot{z}^2 dt$, which was then returned as the output of the solver. The goal of the optimization was to find the design parameters that maximize the harvester output power.

A Pattern Search (PS) algorithm was used in MATLAB (Mathworks 2016) to determine the optimal design parameters for the linear and nonlinear architectures under consideration. Because the objective function requires the numerical solution of eq. (2) subject to fairly long input signals, it was deemed too costly to employ a search method (which may require many function evaluations) in order to inform an initial point for the optimization algorithm. Therefore, in an effort to improve the likelihood that the optimization algorithm converged on or near the global maximum, the algorithm was run multiple times for each signal and each architecture using various initial points, including: a best guess based on the appearance of the spectrogram and, in the case of a linear (nonlinear) architecture, the points near the optimal output for the nonlinear (linear) architecture.

Finally, in order to compare the architectures, the percent change in power from the optimal linear harvester to the optimal nonlinear harvester (found using the PS algorithm) was computed for each representative signal used for the comparison.

Linear and Nonlinear Architecture Comparison Results

Optimal harvester designs were determined using the methodology described in Section 4 and the percent improvement over linear architectures was computed. Approximate values for the percent improvement, as well as values for the optimal β and α, are presented in Table 1.

A linear harvester architecture generally performed as well as the nonlinear harvester architecture in all but one case – Car in highway/X/171 – where the introduction of a nonlinearity in the restorative force resulted in a 14 % improvement of power output over the linear counterpart. As can be seen in Table 1, this single case is also the only significantly nonlinear architecture determined to be optimal by the PS algorithm; in the other cases, the α value (which determines the degree of nonlinearity) is several orders of magnitude lower than the β value,

Table 1: Comparison of optimal linear and nonlinear harvester architectures.

Signal Title/Direction/Number	# Dominant frequencies	Nature	Improvement	Nonlinearity	β [Nm^-1]	α [Nm^-3]
Air Pump/Z/47	2	All Stationary	1 %	Hardening	$77.6 \cdot 10^3$	1.3
Airplane, light turbulence/X/161	>2	0 Stationary	<1 %			
Car in highway/X/171	1	0 Stationary	14 %	Softening	$14.1 \cdot 10^3$	$-99.6 \cdot 10^3$
Chicago metro/Z/165	1	Stochastic	1%	Hardening	$67.7 \cdot 10^3$	1.0
Electric hand shaver/Z/191	1	Stochastic	<1%			
Car highway/Y/229	2	0 Stationary	<1%			

suggesting that the optimal harvester architecture is very nearly linear in these cases.

Discussion

Classifications and Relationship to VEH Design

The study classified a broad range of vibrations from an existing database in order to inform the VEH researcher of the prevalence and characteristics of vibrations seen in real world environments.

The study of 333 signals from the NiPS Real Vibrations database resulted is several interesting conclusions about the available dataset:

The majority of signals do not maintain constant amplitude excitations. This appears to be the case regardless of the source classification.

No single vibration classification appears to describe a single source classification universally. With the exception of the Unknown source classification (not discussed), the greatest portion that any single signal classification consumes within a single source is 64 % (All Nonstationary, Animal). This suggests that proper modelling of a signal from a known source requires more information than simply the source classification of the signal.

Most Animal sources are best described as having distinct dominant frequencies that move with time. 65 % of the signals with the Animal source classification have a dominant component that moved in time. Additionally, nearly half of the Animal signals were embedded in significant levels of noise, as indicated by the number of signals given the noise tag.

Most Machine sources are best described as having distinct dominant frequencies that are stationary, and a substantial portion can best be described using noise. 58 % of the Machine sources analyzed contained dominant frequencies that remained stationary with time, and 9 % contained dominant frequencies that moved with time. 30 % of the Machine sources generated spectrograms that could best be described as "noisy;" that is, 23 % received the "White Noise" classification, and 7 % received the "Filtered Noise" classification.

No single classification dominates the description of Vehicle vibrations. Signals with the Vehicle source classification expressed the most variety in their signal classifications.

Most Structure sources can be described by some type of noise. The White Noise and Filtered Noise signal classifications constitute a combined 64 % of signals that also have the Structure source classification. Nearly all of the remaining signals were classified as having stationary dominant frequencies. Of the signals classified using dominant frequencies, half received the noise tag.

In the case of the single dominant, stationary frequency, it seems unlikely that a novel structure could provide any substantial increase to the maximum power output over a harvester based on a linear oscillator (i. e. characterized by the VDRG model). In fact, it has been shown that for the case of a simple harmonic input, a properly designed linear harvester represents the limiting case of harvester power output (Halvorsen et al. 2013; Heit and Roundy 2015). Of all the signals in the study, approximately 23 % are characterized by a single dominant, stationary frequency.

If the signal can be classified as having multiple dominant, stationary frequencies, then it may be possible to harvest more power from such a signal than could be harvested by a well-designed linear harvester. For example, a multi-mode or wideband harvester might outperform the standard linear oscillator in certain cases. Of all signals in the study, approximately 6 % are characterized by multiple stationary frequencies.

For signals with dominant frequencies that move in time, a tunable harvester would appear to be an appropriate architecture choice, depending on the amount that the frequencies move with time, the characteristic speed with which the frequencies move, and the tuning power costs of the harvester. Wideband harvester architectures could also provide benefit for this class of signal; harvesters with multiple vibratory modes, for example, or harvesters that employ nonlinear dynamical structures have the potential to provide an increase in power over a linear counterpart with a single resonant peak.

Comparison of Linear and Nonlinear Architectures

Much research has been focused on wideband harvesters exhibiting a nonlinear stiffness function, usually characterized by a cubic stiffness function. Thus, it is worthwhile to investigate how often – in the sample set characterized here – this architecture might provide a significant benefit over a standard linear harvester design. As previously mentioned, such nonlinear harvesters may provide a potential improvement in cases with multiple dominant frequencies or a single moving frequency. Hoffmann (Hoffmann, Folkmer, and Manoli 2012) showed an improvement of 479 % for a test case in which the frequency was linearly swept between a low value and a high value using a monostable nonlinear harvester when compared a linear architecture reference design. The amplitude was held constant for this test case. In the same study, a bi-stable harvester showed very little improvement for multiple stationary frequencies. However, nonlinear harvester architectures represented a significant improvement for an input consisting of band-limited noise. Daqaq (Daqaq 2011) has shown that the shape of the potential function does not affect the power that can be harvested from white noise. Therefore, it is reasonable to conclude that the categories where a significant improvement could be made from a nonlinear harvester are single dominant nonstationary frequency, filtered noise, and multiple dominant stationary frequencies. Taken together, these comprise approximately 53 % of the total signals. It should be noted, however, that such nonlinear structures have a strong amplitude dependence and the majority of signals analyzed have shifting amplitudes. Thus, the real percentage of signals for which a nonlinear design would represent an improvement over a linear design will be somewhat lower.

The comparison of linear and nonlinear harvester architectures described in Section 4 resulted in Table 1 in Section 5. Table 1 suggests that a nonlinear harvester architecture with a cubic stiffness function (softening type, a nonlinear monostable configuration) can improve power output when the input signal can be best described as having a single dominant frequency that moves in time; this conclusion is consistent with results from Hoffmann (Hoffmann, Folkmer, and Manoli 2012). For the particular signal under consideration, however, the power was only 14 % greater than the linear counterpart.

For the other signals described in Table 1, the nonlinear architecture did not appear to significantly improve power output over a linear counterpart; a linear harvester came within 1% of the power output of a nonlinear harvester in all but a single case. This suggests that, in at least these cases, a linear harvester architecture could provide optimal power output.

Limitations of the Study

There are numerous limitations to the study:

Uncertainty in measured data. As previously described, nearly 2/3 of available signals were discarded due to poor quality. Of the signal data that appeared to be useful to the study, the majority were measured using an iPhone as the data acquisition system. This raises several concerns as to the validity of the data; namely, it is unknown if the uploader is qualified to be making careful measurements of the vibration signals, the iPhone sampling rate is limited to 100Hz in the database, there are no specifications regarding the recording conditions (mounting and placement of the iPhone, events that occurred during recording, etc.), the iPhone model used for recording is unknown, and at least one source (Allan 2011) states that the maximum resolution of a particular iPhone accelerometer model is 18 mg. Thus, many of the signals that passed the crude quality check may not be valid representations of the phenomena that was intended for recording.

Subjectivity of analysis. One inescapable consequence of having a human visually examine spectrograms for the purpose of signal classification is the subjectivity of the resulting classifications; although efforts were put in place to prevent obvious misclassification (such as fixing the definition of a particular signal classification before classification began), in many cases, two observers may disagree on the classification of a particular signal. For example, a signal that appears to be characterized by a single dominant frequency embedded in noise to one observer may appear to be better characterized as filtered noise to another observer.

The comparison of linear to nonlinear harvester architectures described in Section 4 also suffers from several limitations that make generalization of the results difficult. Firstly, the output of the PS optimization algorithm is highly dependent on an initial point as a first iterate (Mathworks 2016). Because of the computational cost of objective function evaluations (which involves numerically solving (2) over lengthy input signals) a search method that could inform the initial point for the PS algorithm (which would likely require many objective function evaluations) was abandoned in exchange for a "best guess" based on the appearance of the signals' spectrograms. Consequentially, it is possible that entire basins of attraction were overlooked by the PS algorithm, and the optimal points at which the algorithm arrived represent locally optimal designs. Furthermore, limits on the accuracy of the numerical solver output, limits on the mesh resolution of the PS algorithm, as well as chaotic motion that could be exhibited by a nonlinear harvester architecture subject to the representative signals used for the comparison, will result in an objective function that is nonsmooth over the solution space; therefore, even if one could guarantee that the initial point for the PS algorithm is placed in the basin of attraction that contains the global optimum, it could not be guaranteed that the PS algorithm could find the global optimum. As a result of these shortcomings, it cannot be stated with certainty that the cases in which a nonlinear harvester architecture *did not* appear to improve power output over a linear counterpart represent cases in which a nonlinear harvester architecture *could not* improve power output over a linear counterpart.

Future work would include a more refined approach in comparing linear and nonlinear VEH architectures. One potential improvement to the proposed method would involve applying a search method to the optimization procedure in order to inform the initial point of the PS algorithm. Such search methods can help to ensure that multiple basins of attraction are considered in the solution space, improving the likelihood that the final output of the PS algorithm is the global optimum.

Conclusions

333 vibration signals from the NiPS Laboratory "Real Vibration" have been characterized and classified by key vibration characteristics. A primary goal of this classification is to provide insight into the design of vibration energy harvesters (VEHs). Determining the prevalence of vibration signals for which standard VEH architectures are optimal is of particular interest. The vibrations were classified by source (i. e. machine, animal, vehicle, structure, unknown). The signals were further characterized by the number of dominant frequencies, whether these frequencies are stationary or move with time, or whether the signal was best characterized by noise, either broadband or filtered. A comparative analysis of linear and nonlinear harvester architectures was performed using six representative signals as inputs. The results of the comparison suggest that a nonlinear harvester architecture exhibiting a cubic stiffness function may offer improvement over a linear counterpart if the input signal can best be described as having a single dominant frequency that moves in time; for the particular signal under consideration, the degree of power improvement was 14 %. However, a linear architecture performed approximately the same for the remaining five representative signals used in the comparative analysis. A qualitative analysis of the set of signals used in the study indicates that a standard linear oscillator harvester is likely the best design for at least 23 % of the signals and that harvesters with the common cubic nonlinear stiffness function could offer an improvement at most 53 % of the time; this is an initial conclusion based on signal classifications and more study is required to refine this result.

Funding: Funding for this research was provided by the National Science Foundation under Award Number ECCS 1342070.

References

Allan, A. 2011. *Basic Sensors in IOS: Programming the Accelerometer, Gyroscope, and More* (illustrate). O'Reilly Media, Inc.

Daqaq, M. F. 2011. "Transduction of a Bistable Inductive Generator Driven by White and Exponentially Correlated Gaussian Noise." *Journal of Sound and Vibration* 330 (11):2554–2564. doi:10.1016/j.jsv.2010.12.005.

Daqaq, M. F., R. Masana, A. Erturk, and D. Dane Quinn. 2014. "On the Role of Nonlinearities in Vibratory Energy Harvesting: A Critical Review and Discussion." *Applied Mechanics Reviews* 66 (4):40801. doi:10.1115/1.4026278.

Halvorsen, E., C. P. Le, P. D. Mitcheson, and E. M. Yeatman. 2013. "Architecture-Independent Power Bound for Vibration Energy Harvesters." *Journal of Physics: Conference Series* 476:117–121. doi:10.1088/1742-6596/476/1/012026.

Heit, J., and S. Roundy. 2015. "A Framework to Find the Upper Bound on Power Output as A Function of Input Vibration Parameters." *Energy Harvesting and Systems* 1–9. doi:10.1115/SMASIS20147444.

Hoffmann, D., B. Folkmer, and Y. Manoli (2012). Comparative Study of Concepts for Increasing the Bandwidth of Vibration Based Energy Harvesters. In *Proceedings of PowerMEMS 2012*, 219–222. http://cap.ee.ic.ac.uk/~pdm97/powermems/2012/oral/O7A-4.pdf

Mathworks. 2016. Global Optimization Toolbox: User's Guide (R2016b). Retrieved September 15, 2016 from http://www.mathworks.com/help/pdf_doc/gads/gads_tb.pdf

Mitcheson, P., T. C. Green, E. M. Yeatman, and A. S. Holmes. 2004. "Architectures For Vibration Driven Micropower Generators." *Journal of Microelectromechanic System* 13 (3):429–440.

Mitcheson, P. D., E. M. Yeatman, G. K. Rao, A. S. Holmes, and T. C. Green. 2008. "Energy Harvesting from Human and Machine Motion for Wireless Electronic Devices." *Proceedings of the IEEE* 96 (9):1457–1486. doi:10.1109/JPROC.2008.927494.

Neiss, S., F. Goldschmidtboeing, M. Kroener, and P. Woias. 2014. Tunable Nonlinear Piezoelectric Vibration Harvester. *Journal of Physics: Conference Series 557*:12113. 10.1088/1742-6596/557/1/012113

Neri, I., F. Travasso, R. Mincigrucci, H. Vocca, F. Orfei, and L. Gammaitoni. 2012. "A Real Vibration Database for Kinetic Energy Harvesting Application." *Journal of Intelligent Material Systems and Structures* 23 (18):2095–2101. doi:10.1177/1045389X12444488.

Rantz, R., and S. Roundy. 2016. "Characterization of Real-World Vibration Sources with a View toward Optimal Energy Harvesting Architectures." *Proceedings SPIE 9801, Industrial and Commercial Applications of Smart Structures Technologies* 9801:98010P. doi:10.1117/12.2219416.

Roundy, S., E. S. Leland, J. Baker, E. Carleton, E. Reilly, E. Lai, B. Otis, J. M. Rabaey, P. K. Wright. V. Sundararajan. 2005. "Improving Power Output for Vibration-Based Energy Scavengers." *IEEE Pervasive Computing* (Jan-March 2005): 28–36. doi:10.1109/MPRV.2005.14.

Williams, C. B., R. C. Woods, and R. B. Yates. 1996. Feasibility Study of a Vibration Powered Micro-Electric Generator. In *Proceedings of IEE Colloquium Conference on Power Sources (Digest No. 96/107)*, 2–4.

Wu, H., L. Tang, Y. Yang, and C. K. Soh. 2013. "A Novel Two-Degrees-Of-Freedom Piezoelectric Energy Harvester." *Journal of Intelligent Material Systems and Structures* 24 (3):357–368. doi:10.1177/1045389X12457254.

Zine-El-Abidine, I., and P. Yang. 2009. "A Tunable Mechanical Resonator." *Journal of Micromechanics and Microengineering* 19 (12):125004. doi:10.1088/0960-1317/19/12/125004.